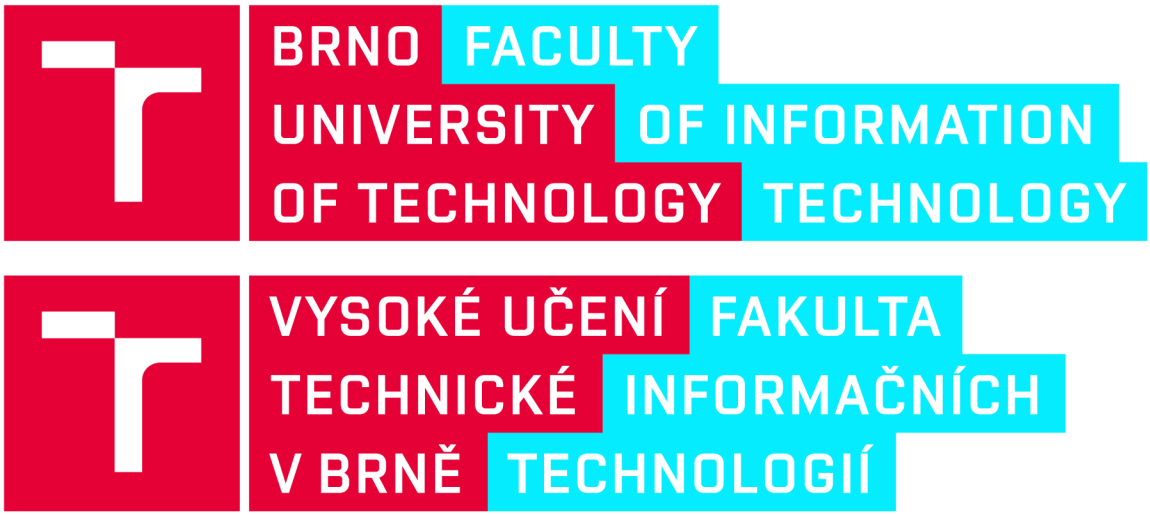

DEPARTMENT OF COMPUTER GRAPHICS AND MULTIMEDIA
ÚSTAV POČÍTAČOVÉ GRAFIKY A MULTIMÉDIÍ

MODEL-BASED 2D-3D REGISTRATION METHODS FOR ANALYSIS OF CONVENTIONAL RADIOGRAPHS

METODY 2D-3D REGISTRACE MODELŮ
PRO ANALÝZU KONVENČNÍCH RENTGENOVÝCH SNÍMKŮ

PH.D. THESIS
DISERTAČNÍ PRÁCE

AUTHOR
AUTOR PRÁCE
ING. ONDŘEJ KLÍMA

SUPERVISOR
VEDOUCÍ PRÁCE
PROF. DR. ING. PAVEL ZEMČÍK

CONSULTANT
KONZULTANT
ING. MICHAL ŠPANĚL, PH.D.

BRNO 2021

Ing. Ondřej Klíma: *Model-based 2D-3D registration methods for analysis of conventional radiographs* , doctoral thesis Brno, Brno University of Technology, Faculty of Information Technology, 2021.

I’d like to dedicate this thesis to my family and friends
for their support in my life.

ABSTRACT

Conventional radiography plays a key role within bone fracture diagnoses, preoperative planning, and postoperative evaluations of orthopedic interventions. The thesis is focused on methods enabling 3D analysis of conventional radiographs, based on the registration of digital models into pairs of calibrated X-ray images.

The thesis presents a method for reconstruction of complete intact models of long bones suffering displaced diaphyseal fractures from conventional radiographs of individual fragments. The reconstruction is achieved using a 2D-3D registration of a statistical shape model into the fragments with simultaneously performed fracture reduction. The reduction is enabled by accurate estimation of the bone length, which is achieved by an automatic division of the statistical shape model into individual fragments. The proposed approach is involved in a software application intended for preoperative planning of diaphyseal fractures reduction with a focus on the identification of the best fitting intramedullary nail or bone plate.

The reconstruction adopts a proposed intensity-based revision of non-overlapping area registration procedure, intended for involvement in model-based radiostereometry. In contrast with the original contour-based formulation, the revised method is able to handle occlusions or unreliable parts of involved digital models. Moreover, performed evaluations reveal an order of magnitude higher accuracy in comparison with the contour-based approach, reaching similar results as the state-of-the-art feature-based approaches, while allowing the involvement of highly detailed 3D models and straightforward acceleration.

In addition to the non-overlapping area approach, also a density-based registration pipeline using statistical shape and intensity models was created for reconstruction of patient-specific bone models. Although reaching slightly lower surface reconstruction accuracy, the density-based registration is able to estimate the internal bone structures such as spongy and compact tissues, potentially providing more information for the planning. For practical aspects, different optimisation methods and possibilities of statistical shape and intensity models lossy compression were investigated.

KEYWORDS

Model-based 2D-3D registration; radiostereometric analysis; preoperative osteosynthesis planning.

ABSTRAKT

Konvenční radiografie hraje klíčovou roli v oblastech dignostiky zlomenin kostí, předoperačního plánování a pooperačního hodnocení ortopedických zákroků. Tato dizertační práce je zaměřena na metody umožňující 3D analýzu konvenčních rentgenových snímků, založené na registraci digitálních modelů.

Práce prezentuje metodu pro rekonstrukci celistvých modelů kostí, které utrpěly dislokované zlomeniny diafýzy, na základě konvenčních rentgenových snímků jejich fragmentů. Rekonstrukce je dosaženo použitím 2D-3D registrace statistického tvarového modelu do jednotlivých fragmentů a jejich současně prováděné repozice. Repozice je umožněna díky přesnému odhadu délky kosti, kterého je dosaženo automatickým dělením statistického tvarového modelu do jednotlivých fragmentů. Vytvořená metoda byla vestavěna do softwarové aplikace určené pro předoperační plánování osteosyntézy diafýzy se zaměřením na výběr vhodného intramedulárního hřebu nebo rekonstruční dlahy.

Rekonstrukce částečně využívá navrženou intenzitní revizi registrační procedury minimalizující nepřekrývající se oblasti, určenou pro radiostereometrii založenou na modelech. Oproti původnímu přístupu využívající kontury modelů je revidovaná metoda schopna pracovat s jejich překrytými nebo nespolehlivými částmi. Provedené evaluace také vykazují řádově vyšší přesnost ve srovnání s přístupem založeným na konturách a dosahují srovnatelných hodnot se současnými hranovými metodami, zatímco je umožněno použití modelů s vysokým počtem polygonů, přímá akcelerace a snadná interpretovatelnost.

Pro rekonstrukci modelů kostí byla kromě přístupu založeném na nepřekrývajících se oblastech vytvořena také registrace založená na hustotách a využívající stastistické tvarové a intenzitní modely. Ačkoliv metoda dosahuje mírně nižší přesnosti rekonstrukce povrchu, registrace založená na hustotách umožňuje odhadnout vnitřní struktury kosti tvořené kompaktní a houbovitou tkání a poskytnout tak více informací pro plánování. Pro praktické využití bylo také zkoumáno nasazení různých optimalizačních metod a možnosti ztrátové komprese statistických tvarových a intenzitních modelů.

KLÍČOVÁ SLOVA

2D-3D registrace modelu; radiostereometrická analýza; předoperační plánování osteosyntézy.

BIBLIOGRAPHIC CITATION

Ing. Ondřej Klíma: *Model-based 2D-3D registration methods for analysis of conventional radiographs* , doctoral thesis Brno, Brno University of Technology, Faculty of Information Technology, 2021.

DECLARATION

I declare that this dissertation thesis is my original work and that I have written it under the guidance of prof. Dr. Ing. Pavel Zemčík and Ing. Michal Španěl, Ph.D. All sources and literature that I have used during my work on the thesis are correctly cited with complete reference to the respective sources.

Brno, 2021

Ing. Ondřej Klíma, August 31, 2021

ACKNOWLEDGMENTS

Many thanks belong to my consultant Michal Španěl and supervisor Pavel Zemčík for their support, patience, and guidance during the study, for my involvement in research projects allowing me to formulate the presented ideas, and particularly for my introduction into the field of preoperative planning. My gratitude also belongs to colleagues Petr Klepárník and David Bařina for efforts spent on OpenGL acceleration of the registration framework and cooperation regarding lossy compression topics.

I am grateful to Roman Madeja, Petr Novobilský, Petr Krupa, and Leopold Pleva from University Hospital Ostrava for arranging the radiographic acquisitions, providing computed tomography images and arthroplasty prostheses, evaluation of the presented methods, and for interesting insights into the medical field. Many thanks also belong to colleagues from TESCAN 3DIM for preprocessing the computed tomography volumes and for the development of experimental preoperative planning application partially based on the proposed approaches. I would also like to thank Miroslav Králík and Martin Čuta from the Department of Anthropology at Masaryk University for providing archeological material for the anatomy reconstruction evaluations and fruitful discussions. An optical 3D scanning of arthroplasty prostheses was generously performed by Pavel Stoklásek and Aleš Mizera from Tomas Bata Univerzity in Zlín. I am also grateful to Adéla Hýlová for providing the CAD drawings of the biplanar calibration box and Plexiglas® phantom and Koplast s.r.o. for their construction. I would like to thank Adam Chromý for his cooperation on junior research grants related to model-based registration in the medical field. My final thanks belong to Lukáš Polok for kindly providing the LaTeX template based on `classicthesis`.

The research was financially supported by Czech Technology Agency grants Modern Image Processing Techniques and Computer-based Planning in Trauma Treatment (TA04011606) and V3C - Visual Computing Competence Center (TE01020415). The support was also provided by Brno University of Technology junior research grants Intermodal Registration of Medical 3D Data (FEKT/FIT-J-17-4745) and Application of 3D Modeling in Medical Imaging (FEKT/FIT-J-16-3485) and by the Ministry of Education, Youth and Sports from the National Programme of Sustainability (NPU II) project IT4Innovations excellence in science (no. LQ1602).

CONTENTS

1

INTRODUCTION

Conventional radiography is a key imaging technique for skeletal examinations, such as fracture diagnose, preoperative planning, or postoperative assessment, and evaluation of orthopedic interventions, providing 2D intensity images of a patient's internal tissues. The thesis is focused on methods enabling 3D analysis of conventional radiographs, based on the registration of virtual models into calibrated biplanar radiographs. Presented methods are designed for involvement in fields of preoperative planning of osteosynthesis, used for the digital 3D templating to identify the best fitting fixation material for fracture treatment, and model-based roentgen stereophotogrammetric analysis focused on assessment of joint replacement micromotion.

Current systems for 3D preoperative planning based on plain radiographs are mostly focused on joint arthroplasties. The systems exploit deformable 2D-3D registration of 3D bone atlases into the radiographs to recover the patient-specific bone models. The thesis deals with problems related to construction of a similar solution for preoperative planning of diaphyseal fractures reduction and fixation. In contrast with the current systems, the main challenge of the proposed solution is a reconstruction of a complete bone model from radiographs of its individual fragments, which is in the case of diaphyseal fractures closely related to the correct estimation of the bone length. The thesis addresses the challenge by proposing a novel multi-fragment registration method with an automatic splitting of the bone atlas into the individual fragments.

The multi-fragment registration method extends a revision of the non-overlapping area approach, proposed within the scope of the thesis, adopted from the field of model-based radiostereometric analysis. The intensity-based revision addresses a problem of differences between virtual 3D models and the radiographic images, caused by occlusions, missing parts of the models, or bone degradations, negatively affecting the 2D-3D registration accuracy.

The thesis also focuses on aspects allowing practical application of the preoperative planning system, including reconstruction accuracy and time and space consumption, providing a comparison of intensity-based and density-based registration approaches, evaluation of different optimization formulations and methods, and investigating possibilities of the bone atlases compression.

The thesis is written as a compilation of the author's previous publications, ordered ascending by the complexity of the presented registration approach. Selected

papers were further extended with appendix sections presenting additional details. Part i provides a brief introduction into fields of pre-operative planning and radiostereometric analysis with an overview of selected existing solutions. Parts ii presents published contributions focused on the 2D-3D registration methods. Part iii provides additional discussions and notes on the results and concludes the thesis. Part iv consists of conference abstracts, describing preliminary results of the proposed methods. Supplementary materials, including technical drawings of calibration phantoms, markers, and an overview of constructed shape and intensity models are attached in the final part v.

Part I

COMPUTER-ASSISTED METHODS IN RADIOGRAPHS ANALYSIS

This part presents a brief introduction to the fields of preoperative planning and roentgen photogrammetric analysis with a focus on the application of digital 3D models.

2

ROENTGEN STEREOPHOTOGRAMMETRIC ANALYSIS

Roentgen stereophotogrammetric analysis [105, 103, 104] is a proven method for high-precision assessment of motion between anatomical structures, bone implants, or joint replacements. The analysis allows observation of spatial movement between objects captured on conventional radiographs. Since its introduction, the method has become the basis of considerable many clinical studies with various focuses. The analysis is mainly used for an assesment of joint replacements mechanical stability, evaluating implant fixation within the surrounding bone, mostly in relation with a hip [83, 25, 128, 31, 75] or knee arthroplasty [137, 88, 38, 43, 45, 5]. In addition to the lower extremity joints, the analysis is feasible also for an evaluation of upper limb arthroplasty [20], particularly in cases of shoulder [116, 77, 115, 93, 85] and elbow joints [126, 123]. Beyond the implant fixation, the radiostereometry is applied for joint stability [8, 33] and kinematics [19, 58, 121] observation, or a fracture treatment and stability evaluation [66, 94, 92].

2.1 CONVENTIONAL RADIOSTEREOMETRY

For motion evaluation, the conventional radiostereometry uses sets of tantalum beads marking the observed objects. The three-dimensional poses of the beads are computed from stereo radiographs.

2.1.1 *Stereo Radiographs Acquisition*

The stereo radiographs are usually captured using a bi-planar X-ray imaging facility. Acquisition of stereo radiographs is enabled by the involvement of calibration cages into the imaging procedure, as shown in Figure 2.1. As the relative patient's pose to the calibration box must be the same in both radiographs, the images are usually taken at the same time using a synchronized imaging machine.

The calibration cages are equipped with tantalum bead markers in several different planes. Due to the known spatial placement of the beads within the cage and their consequent projections in captured radiographs, it is possible to reconstruct a 3D scene capturing the examination set up. As a result of the calibration, 3D poses of the radiation sources, box, and radiographs are known. In contrast with the original method, using fiducial and control planes (FCP) [103], the calibration approach

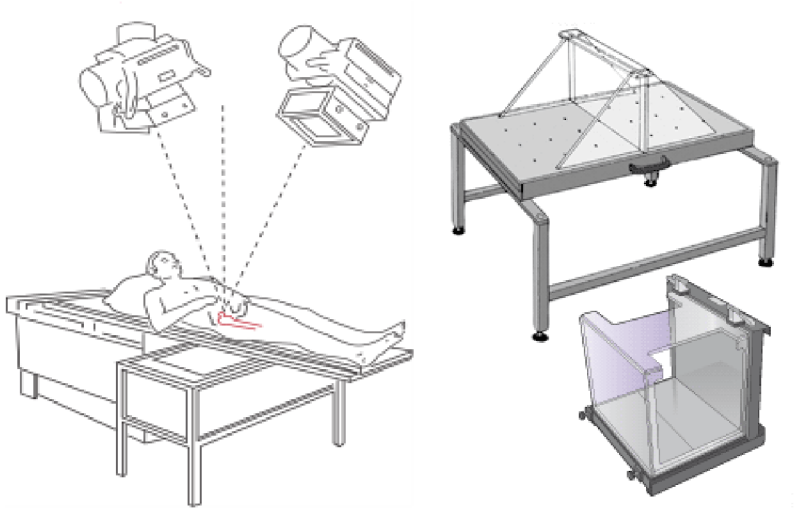

Figure 2.1: Roentgen stereophotogrammetric analysis set up *(left)* with a uniplanar calibration box placed under the patient[1]. Schematic pictures of uniplanar and biplanar calibration cages provided by RSA Biomedical AB[2] *(right)*. The top calibration box is intended for examination of hip joints, the bottom cage is designed for knee, ankles, and elbows. The biplanar design was also adopted for the custom-made calibration box in the chapters 5 and 9.

involved within the scope of this thesis is based on camera pinhole model [44]. Formally, the calibration aims to recover the intrinsic and extrinsic parameters of the camera model, for both radiographs and respective X-ray sources. The extrinsic parameters are given by a rigid transformation matrix $(R|t)$, describing rotation and translation of the camera within the space of the calibration box. Intrinsic parameters, written in matrix C, contain image scaling, given by a source to image distance and pixel spacing of the detector, and coordinates of the principal point, where the optical axis intersects the detector. A relation between a pose X of a tantalum bead within the 3D space and its image x in a radiograph, expressed in homogenous coordinates, is consequently given as $x = C(R|t)X$. Having pairs of bead poses and their respective projections, it is possible to obtain a matrix $P = C(R|t)$ using a direct linear transformation (DLT) [22]. Using an approach based on QR factorization, the P matrix is finally decomposed to the individual rotation and translation matrices. Although the direct linear transform is feasible with at least 6 pairs of the beads poses and projections, the higher number increases the accuracy of the calibration. The calibration box involved in the following studies includes 18 bead markers for each view.

[1] http://www.rsacore.nl/model-based-rsa/about-rsa/

[2] https://rsabiomedical.com/

Figure 2.2: Tantalum beads provided by Halifax Biomedical Inc.[3] in comparison with the size of One Dime *(left)*. Commonly used beads are of size 0.8 and 1.0 mm in diameter. Beads injector provided by the same company *(middle)*. The injector uses cartridges pre-loaded with 16 tantalum markers of 1.0 mm diameter *(right)*.

2.1.2 *High-precission Motion Assessment*

The most common application of the radiostereometric analysis is an observation of joint replacement mechanical stability, when the micro-motion between the prosthesis and the surrounding bone is assessed during long-term follow-up examinations [83, 25, 137]. A determination of the relative pose is possible due to sets of tantalum beads, where the first set of beads is attached to the implant, usually by the manufacturer, and the second set is injected directly to the bone by a surgeon. A sample of the commercially available injector and beads is shown in Figure 2.2.

Using the extrinsic and intrinsic parameters of the camera model, it is possible to reconstruct 3D poses of individual beads attached to the implant or injected into the bone, captured in radiographs. A pose of an individual bead is obtained as an intersection of two rays, coming from the radiation sources and falling on the detectors. The intersection is usually approximated by a middle point of the shortest distance segment connecting the two rays, as the real data are usually noisy.

The major drawback of the conventional radiostereometry is its dependence on the bead markers, that must be attached to the implant, which limits the applicability of the method only to special prostheses.

2.2 MODEL-BASED RADIOSTEREOMTERIC ANALYSIS

To overcome the dependence of the analysis on special implants equipped with beads, a model-based radiostereometry was proposed by Valstar [124], relying on virtual models of the implants, obtained in form of CAD models of the prosthesis design, reverse engineering [56] or primitive geometry models [55, 51]. Instead of

[3] https://halifaxbiomedical.com/imaging/what-is-rsa/

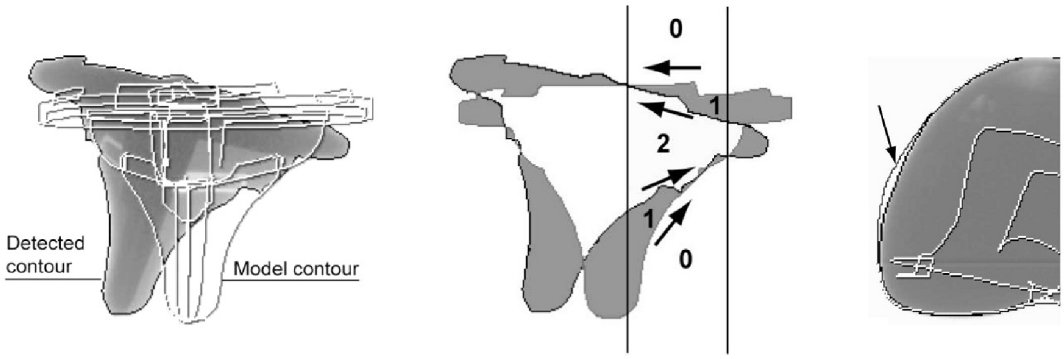

Figure 2.3: An implant segmented from a radiograph overlayed by silhouettes rendered using the digital model *(left)*. Direction codes-based non overlapping area measure *(middle)*. Differences between CAD model and real implant caused by dimensional tolerances *(right)*. Adopted from [124].

markers, the pose of the implant is recovered using registration of the digital model into the calibrated stereo radiographs. The registration is usually formulated as an iterative optimization problem, which minimizes reprojection error between the input radiographs and projections of the digital model.

2.2.1 *Contour-Based Non-Overlapping Area*

The first published model-based method was based on minimization of the uncommon area between the captured implant and the digital model projection [124], as shown in Figure 2.3 *(left)*.

For the evaluation of the non-overlapping area measure, the contours of the implant and the model projection are divided into common intervals along the horizontal axis, while the number of intervals is given as a number of model silhouette nodes minus one. In each interval, individual segments are given an area code based on the silhouette direction values. The direction value is determined with respect to the horizontal orientation of the silhouette part. When the silhouette part has a positive x-direction, it is assigned a direction value equal to 1, otherwise, the direction value is set to -1. Then, each direction value is assigned to the area above the corresponding silhouette. In the next step, area codes are obtaibned by summing up the direction values, as shown in Figure 2.3 *(middle)*. When the resulting area code is equal to +1 or -1, the part belongs to the non-overlapping area. The final value of the measure is given by summing the size of all uncommon parts together. During the registration process, the measure is minimized as a scalar-valued objective function using Feasible Sequential Quadratic Programming (FSQP) [113] optimization method.

The contour-based non-overlapping area requires a complete contour of the implant, which is a major drawback with respect to unreliable parts of a prosthesis or its possible occlusions, as shown in Figure 2.3 *(left)*. The unavailable part of the contour must be manually estimated by a user, which affects the registration accuracy.

2.2.2 *Feature-Based Methods*

In contrast with non-overlapping area approach, feature-based methods minimize distances between corresponding points of actual and virtual contours. The most commonly used approaches are Iterative Inverse Perspective Matching (IIPM) [54] and Contour Difference (DIF) [34] algorithm. Both algorithms estimate the correspondences by finding the closest points on the virtual contour for each vertex of the actual silhouette, as shown in Figure 2.4. The contour difference algorithm then minimizes the mean distance of all actual vertices by using DHSAnn or DoNLP2 optimizers [90].

On the other hand, the perspective matching algorithm back projects the virtual points back on the digital model and estimates poses of the actual vertices within the model space. The model is then aligned to the estimated actual vertices. The process based on Iterative Closest Point (ICP) [14] is repeated until the model is finally aligned.

In practice, combinations of different metrics and optimizers are used successively to reach the optimal alignment, usually in IIPM, DIFDoNLP, and DIFDHsAnn order [114, 91, 39, 84]. The feature-based methods reach higher accuracy in comparison with the contour-based non-overlapping area, as they allow to drop out the uncertain or occluded parts of involved models.

2.2.3 *Intensity-based Non-Overlapping Area*

The thesis proposes an intensity-based revision of the non-overlapping area registration [KNM+18], which enables drop-outs and thus reaches a similar accuracy as the state-of-the-art feature-based methods while allowing the involvement of high-poly models and straightforward acceleration. The revision is subsequently extended for reconstruction of patient-specific bone models [KKŠZ16a, KMŠ+18].

2.3 DYNAMIC RADIOSTEREOMETRY

Dynamic radiostereometric analysis is used for assessment of joint kinematics, allowing observation of 3D motion reconstructed from fluoroscopic sequences. To

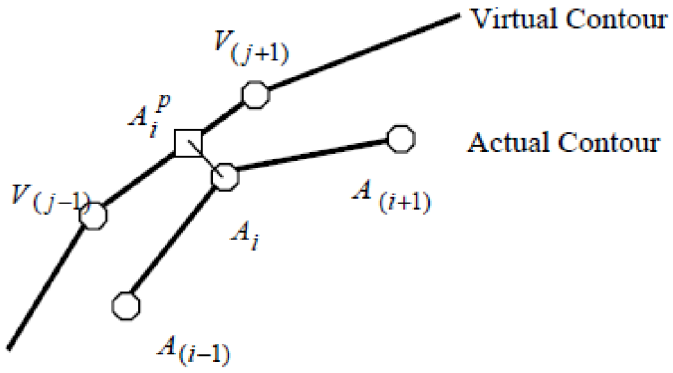

Figure 2.4: Estimation of correspondences between the virtual and actual contour. For each vertex A_i of the actual contour, a closest point A_i^p on the virtual silhouette is found. Adopted from [54].

prevent surgical marking of the bones using tantalum beads, the method exploits registration of bone models obtained by computed tomography [40, 39, 23]. The digital model is produced by the volume segmentation followed by marching cubes algorithm [71] and mesh postprocessing, usually consisting of decimation and smoothing. Then, poses of bones within each frame of the sequence are estimated by the registration of their digital models, using the methods described in Section 2.2.2.

2.3.1 *Statistical Shape Models*

To avoid the need for computed tomography image acquisition, it is possible to exploit a statistical shape model of the bones [12, 13, 122], to simplify the process and increase its applicability. The statistical shape model serves as an elastic atlas, capturing shape variations of the bone within the population. The atlas is constructed using a training set of rigid models obtained from computer tomography images, which are brought into correspondence, mutually aligned using Generalized Procrustes Analyzes (GPA) [28] and processed using Principal Component Analysis (PCA) [3], as shown in 2.5. Consequently, the statistical shape model is deformable with respect to given PCA modes in a such constrained way that it generates biologically plausible shapes.

During the registration, the shape of the model is optimized together with its pose. As a result, in addition to the observed motion, also patient-specific models of the joint bones are recovered without the computed tomography image acquisition.

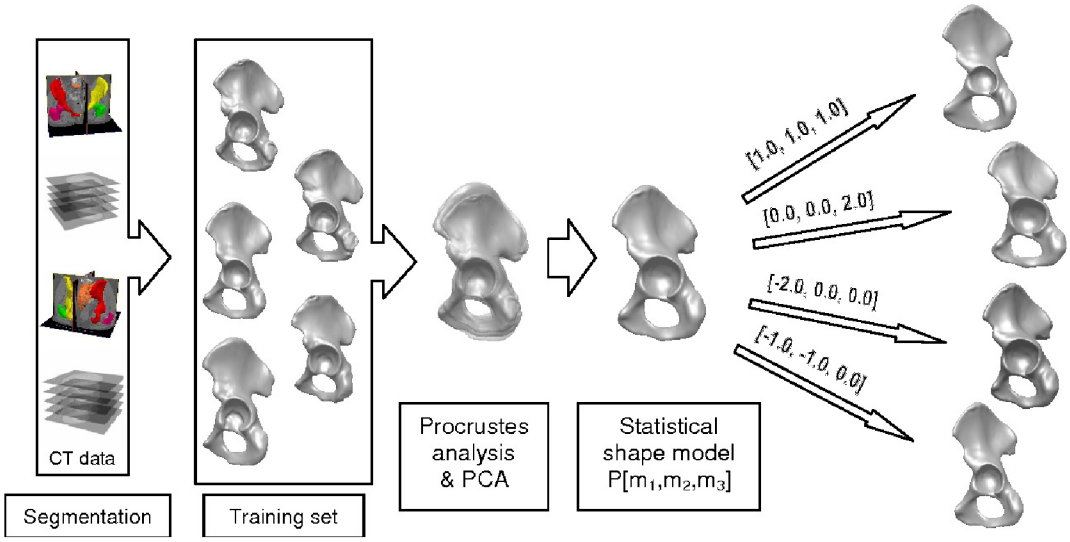

Figure 2.5: Pipeline describing the construction of a pelvic statistical shape model, retrieved from [110]. First, polygonal models are segmented from the training set of volumetric images. Then, the models are brought into correspondence, aligned using Generalized Procrustes Analyzes (GPA) [28] and processed using Principal Component Analysis (PCA) [3]. Model instances corresponding to different values of the shape modes are shown on the right.

3

SYSTEMS FOR DIGITAL PREOPERATIVE PLANNING

Preoperative planning based on digital templating takes an essential part in total joint arthroplasty [47, 9] and is of significant benefit in case of fracture reduction and treatment [7]. The aim of the templating is a selection of ideally fitting joint replacement or fixation material for a specific patient.

Conventional planning depends on X-ray film, manually overlayed with acetate sheet with a printed template of the evaluated implant [67]. However, the conventional templating is usually prone to mismatches between template and radiograph magnification, depending on factors as source-to-image distance, patient's positioning or physique, difficulting identification of ideal implant dimensions.

Since the advent of digital radiography, the planning is performed using a clinical software application instead of the acetate sheets. Consequently, it is possible to address the magnification using a calibration marker of known dimensions by scaling the digital image to the correct size [18, 17]. An example of commercialy available magnification marker provided by Innomed, Inc. manufacturer is shown in Figure 3.1.

More precise planning is enabled by 3D templating, exploiting bone models obtained from computed tomography images [87]. However, the requirement of computed tomography examination complicates the process, exposes the patient to higher radiation doses [112] and brings additional costs. Therefore, systems for 3D preoperative planning based on the 2D-3D reconstruction of bone models have

Figure 3.1: Lombardi self-holding X-ray magnification marker. Retrieved from Innomed, Inc.[1].

[1] https://www.innomed.net/

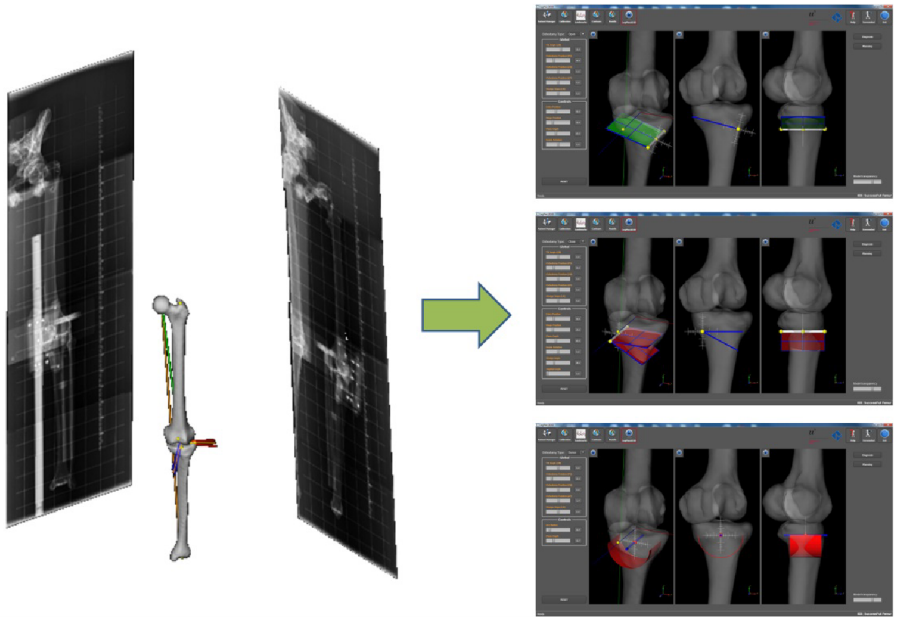

Figure 3.2: Reconstructed bone models within the calibrated space of original radiographs *(left)* with a screenshot of the preoperative planning software based on the models *(right)*. Retrieved from [2].

been proposed [2, 1, 136, 46]. Similar to the case of dynamic radiostereometry described in Section 2.3.1, the reconstruction is performed by performing registration of a statistical shape model into conventional radiographs. As a result, a three-dimensional model suitable for the digital templating is obtained.

3.1 TOTAL KNEE ARTHROPLASTY

For the preoperative planning of the total knee arthroplasty, systems 3XPlan [46], 3X-Knee [136] and iLeg [2] have been proposed, involving a reconstruction method based on [135]. Beyond the identification of the best fitting knee prosthesis, the reconstructed bone models are also used for planning the osteotomy planes, or the postoperative assessment of the intervention. An illustration of the iLeg system is shown in Figure 3.2.

3.1.1 *Radiographs Acquisition*

Opposed to radiostereometry, clinical radiographs for preoperative planning are usually taken sequentially. During the sequential capturing, the pose between the calibration marker and the examined bones must remain unaltered. Therefore, it is necessary to immobilize the joint and ensure rigidity of a marker attachment. Figure 3.3 shows a solution proposed in [135], where a calibration phantom *(left)*

is attached to an immobilization apparatus *(right)*. The phantom design and calibration framework are detailed in [100].

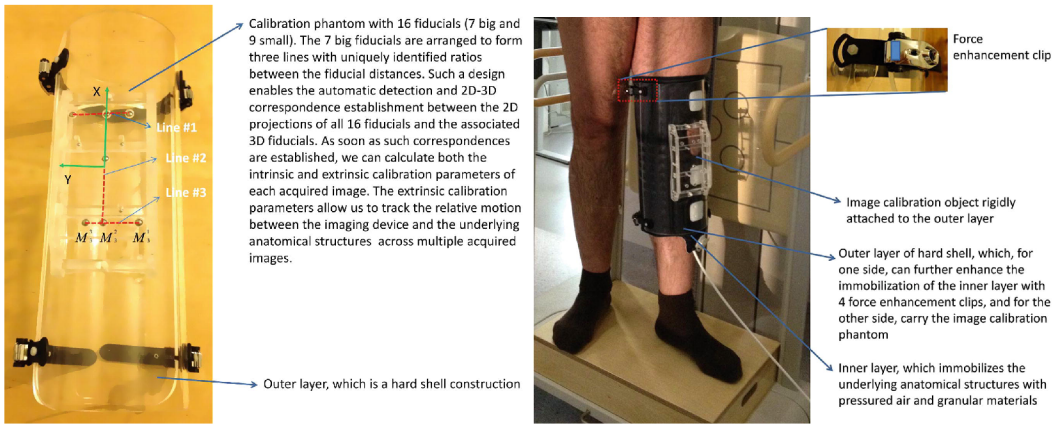

Figure 3.3: Phantom used for sequential acquisition of knee joint radiographs *(left)*, attached to the knee immobilization apparatus *(right)*. Adopted from [135].

Within the scope of this thesis, sequential radiographs are used for the reconstruction of fractured bones. In this case, the immobilization of individual fragments is performed using a limb vacuum splint, the calibration marker is temporarily fixed to the splint in an adhesive manner. The involved markers and radiographic examination of dummy with splint are described in Supplement F, Figures F.1 and F.3.

3.2 TOTAL HIP ARTHROPLASTY

An iJoint [1, 99] system based on similar principles was proposed for preoperative planning of total hip arthroplasty. The system provided an automatic detection of the calibration marker within the radiographs, using a CLAHE algorithm [89], circular Hough transformation (CHT) [29] and a simulation-based verification of fiducials candidates. The digital models were reconstructed using a hierarchical registration of femoral and pelvic statistical shape models [98]. A schematic illustration of the system is shown in Figure 3.4.

3.3 DIAPHYSEAL FRACTURE REDUCTION

Beyond the joint arthroplasty, also possibilities of statistical shape models involvement in preoperative planning of osteosynthesis surgery have been studied [101, 35]. Schumann et at. [101] proposed an approach aiming at diaphyseal fractures of long bones, estimating rotational alignment of proximal and distal fragments. The method was based on the registration of a single shape prior into the individual fragments [134], initialized by commonly used landmarks [127, 117, 130].

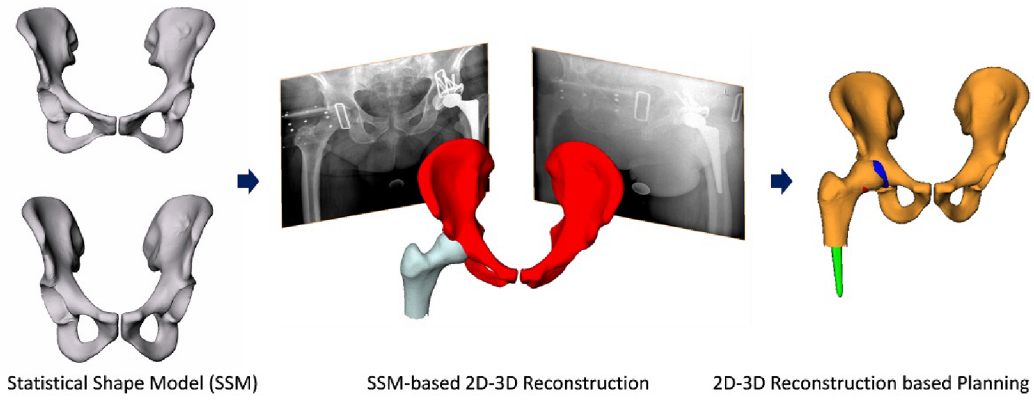

Figure 3.4: A schematic description of the iJoint system. Retrieved from [1].

However, before the registration, the shape model had to be split into the fragments manually, based on an external measurement of the bone. Therefore, due to the unability to recover the accurate bone length the method was not able to reconstruct complete models of intact bones, but only models of individual fragments and their rotational alignment. The method was evaluated using data sets of virtual radiographs and a mock-up with sawed plastic bone models, as shown in Figures 3.5 and 3.6.

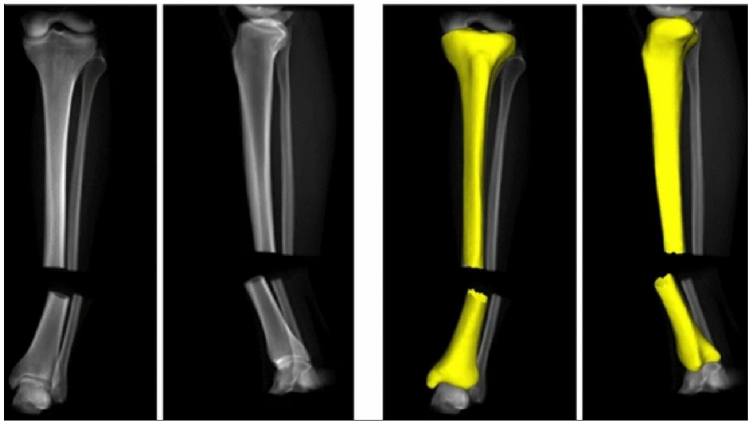

Figure 3.5: Virtual radiographs of fractured tibial bone with reconstructed models of individual fragments. Adopted from [101].

In contrast with [101], the method presented within this thesis [KMŠ+18] is able to split the statistical shape model automatically and therefore to produce models of complete intact bones of accurate length. Consequently, the method [KMŠ+18] has been included in the preoperative planning software called TraumaTech[2], allowing estimation of intramedullary nail ideal length or selection of best fitting bone plate. Table 3.1 provides a brief summary on systems focused on 3D preoperative planning based on planning radiographs.

[2] https://www.tescan3dim.com/solutions/medical-software/digital-orthopaedics

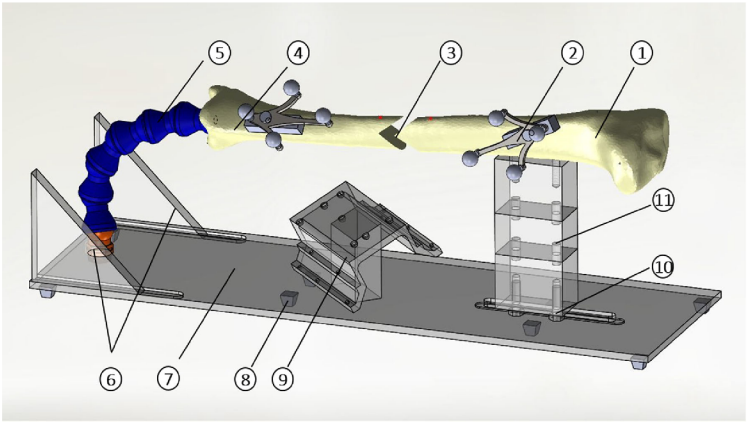

Figure 3.6: A mock-up with calibration phantom and plastic model of the tibial bone. Adopted from [101].

Table 3.1: Overview of solutions for 3D preoperative planning using plain radiographs.

Solution	Intervention	Form	Objects in the input radiographs	Outcoming reconstructed model(s)
iLeg [2]	TKA	System	Uninjured bones	Intact bones
3XPlan [46]	TKA	System	Uninjured bones	Intact bones
3X-Knee [136]	TKA	System	Uninjured bones	Intact bones
iJoint [1, 99]	THA	System	Uninjured bones	Intact bones
Schumann [101]	Osteosynthesis	Study	Fractured bone	Individual fragments
Proposed solution [KMŠ+18]	Osteosynthesis	System	**Fractured bone**	**Intact bone**

Part II

PUBLISHED CONTRIBUTIONS

4

RESEARCH OUTLINE

The thesis is mainly focused on registration methods allowing the reconstruction of patient-specific three-dimensional models of long bones from conventional radiographs. The state-of-the-art methods focus on a reconstruction of uninjured long bones, or the reconstruction of individual fragments in cases of their diaphyseal fractures. The main research question of the thesis is if it is possible, in case of displaced diaphyseal fracture of a long bone, to reconstruct a model representing a complete intact bone only from radiographs of its individual fragments. The main scientific contribution of the thesis is therefore verification of the statement: *It is possible to design a method performing reconstruction producing models with accurate shape and length that overcomes the capabilities of the state-of-the-art reconstruction methods.* The verification is performed by proposing a reconstruction method dealing with fractured long bones and its experimental evaluation.

The following papers describe individual steps leading to the final design of the reconstruction pipeline, its evaluation and also consider practical aspects allowing application of the methods in preoperative planning software.

Paper [KNM+18] focuses on the revision of rigid registration method based on non-overlapping area approach, intended for involvement in model-based roentgen stereo photographic analysis. The paper presents an intensity-based revision of the original contour-based approach, involving an effective Levenberg-Marquardt optimizer with a coarse-to-fine strategy of central-differences approximation of Jacobian matrix and allowing to drop the uncertain or occluded parts of the models out of the registration. The paper experimentally evaluates to what extent the revised formulation outperforms the original approach and if its accuracy is comparable with the state-of-the-art methods currently used in the field of model-based radiostereometry. The proposed method, originally designed for rigid 2D-3D registration of bone implants, is in subsequent papers extended and used for reconstruction of patient-specific bone models.

Paper [KKŠZ16a] is focused on a reconstruction of uninjured patient-specific bone models using 2D-3D registration of statistical shape and intensity models into captured radiographs. The paper proposes a density-based reconstruction, based on statistical shape and intensity models, normalized mutual information similarity measure, and Levenberg-Marquardt optimisation, and compares it with an extended approach based on the revised non-overlapping area registration, referred to as *Black&White Pixel Differences* method. The paper investigates if a Levenberg-

Marquardt solver is an efficient optimizer for performing deformable 2D-3D registration in terms of speed and accuracy and how the reconstruction accuracy is affected by the presence of the density information.

As the reconstruction speed is crucial for real involvement of the methods in preoperative planning software, the paper [KCZ+16] investigates if a Levenberg-Marquardt optimisation, involving a computationally demanding numerical central-differences approximation of a Jacobian matrix, is within the terms of the 2D-3D registration more effective than the commonly used evolution strategies.

The density information present in statistical shape and intensity models also usually requires not negligible storage space. Therefore, the paper [KBK+16] investigates if it is possible to use lossy compression on the statistical shape and intensity models to reduce their space requirements and to what extent the compression artifacts affects the 2D-3D reconstruction accuracy.

The main contribution of the thesis is finally presented in paper [KMŠ+18], which describes the design and evaluation of the 2D-3D reconstruction pipeline for long bones suffering diaphyseal injuries. The design involves the intensity-based revision of non-overlapping area approach, extended to the form of multi-fragment registration with an automatic splitting of the statistical shape model into the individual bone fragments, to ensure an accurate estimation of the bone length. The paper presents evaluations of the design using synthetic and cadaveric data sets, revealing if the reconstruction of an intact bone model from the radiographs of individual fragments is feasible and if the reconstruction accuracy is sufficient for the involvement of the method in preoperative planning software.

5

INTENSITY-BASED NON OVERLAPPING AREA REGISTRATION SUPPORTING "DROP-OUTS" IN TERMS OF MODEL-BASED RADIOSTEREOMETRIC ANALYSIS

CITATION

[KNM+18] Ondřej Klíma, Petr Novobilský, Roman Madeja, David Bařina, Adam Chromý, Michal Španel, and Pavel Zemčík. Intensity-based nonoverlapping area registration supporting "drop-outs" in terms of model-based radiostereometric analysis. *Journal of Healthcare Engineering*, 2018:8538125, May 2018. **(Impact factor: 1.295)**

ABSTRACT

A model-based radiostereometric analysis (MBRSA) is a method for precise measurement of prosthesis migration, which does not require marking the implant with tantalum beads. Instead, the prosthesis pose is typically recovered using a feature-based 2D-3D registration of its virtual model into a stereo pair of radiographs. In this study, we evaluate a novel intensity-based formulation of previously published non-overlapping area (NOA) approach. The registration is capable to perform with both binary radiographic segmentations or non segmented X-ray images. In contrast with the feature-based version, it is capable to deal with unreliable parts of prosthesis. As the straightforward formulation allows efficient acceleration using modern graphics adapters, it is possible to involve precise high-poly virtual models. Moreover, in case of binary segmentations, the non-overlapping area is simply interpretable, useful for indicating the accuracy of the registration outcome. *In silico* and phantom evaluations were performed using a cementless Zweymüller femoral stem and its reverse engineered (RE) model. For initial pose estimates with difference from the ground-truth limited to ± 4 mm and ± 4 °respectively, the mean absolute translational error was not higher than 0.042 ± 0.035 mm. The error in rotation around the proximodistal axis was 0.181 ± 0.265 °, error for remaining axes was not higher than 0.035 ± 0.037 °.

KEYWORDS

Radiostereometric analysis, implant migration, pose estimation, intesity-based registration, OpenGL acceleration

5.1 INTRODUCTION

Roentgen stereophotogrammetric analysis (RSA), introduced by Selvik [103, 104], is an established method for an accurate measurement of prosthesis mechanical stability, indicated in particular in cases of total joint arthroplasty. The analysis is used for measuring micromotion between the prosthesis and the surrounding bone. Due to its high precision, it allows to reveal a potential failure of the implant fixation at early stages, when the prosthesis migration is not recognizable in plain radiographs nor clinical symptoms occur [82]. The conventional radiostereometric analysis depends on two sets of tantalum beads. The first set of markers is attached to the prosthesis, while the second set of beads is injected directly into a bone surrounding the implant. A position of each marker in three dimensional space is obtained using a triangulation from a stereo pair of radiographs. Commonly, a patient undergoes several following-up radiographic examinations during a certain time period after the arthroplasty [125]. A potential failure of the prosthesis fixation is observed when the relative pose between the two sets of markers differs between the individual examinations.

However, the attachment of tantalum beads to the implant raises several potential issues. In radiographs, the prosthesis may occlude the attached beads, marked implants are more expensive and the strength of the prosthesis may be negatively affected. To overcome these difficulties, model-based radiostereometric analysis (MBRSA) has been proposed by Valstar [124]. Instead of attaching the beads, the implant pose is recovered by 2D-3D registration of its virtual model into a stereo pair of radiographs. Several studies have revealed the model-based radiostereometry reaches lower, but acceptable accuracy in comparison with the conventional approach [57, 81, 106].

Registration methods used in radiostereometry are typically feature-based, exploiting edges detected in radiographs and a prosthesis outline obtained from the virtual model. Valstar [124] proposed an approach based on non overlapping area (NOA) minimization, which required a complete outline of the prosthesis to be obtained from the radiographs. The major drawback of the method was an inability to handle unreliable parts of the detected outline, as there were significantly large dimensional differences between the actual prosthesis and its computer-aided design (CAD) model involved in the phantom evaluation. A following-up study, pro-

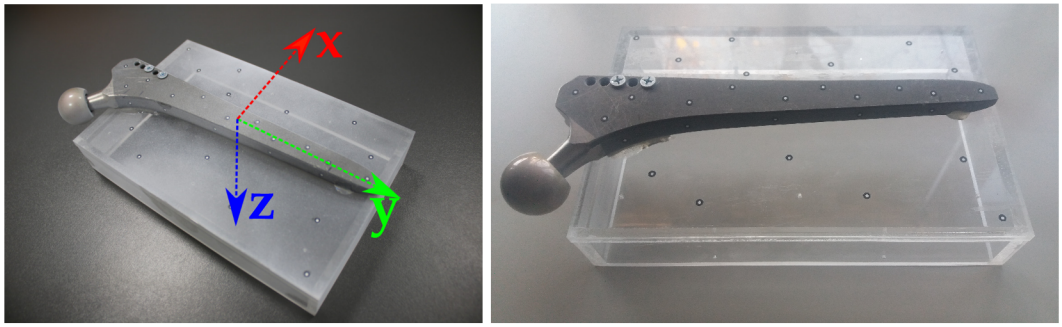

Figure 5.1: The Zweymüller femoral stem attached to the Plexiglas® phantom. The green arrow shows a proximodistal axis of the implant.

posed by Kaptein [56], enhanced the accuracy by using reversed engineering (RE) models of prosthesis instead of CAD models provided by a manufacturer and by improving the registration method to handle the unreliable parts of detected contours, referred to as “drop-outs", which may be caused by metallic objects that are not included in the virtual model, such as bone screws, etc. The registration was based on minimization of contour difference, which can be in contrast with original non overlapping area evaluated locally and the unreliable parts of the contour, selected by the user, may be simply omitted from the registration. The minimization of contour difference was in broader principle adopted by many subsequent studies [57, 65, 118, 81].

In this study, we propose an intensity-based radiostereometric method, reviving the idea of non overlapping area. In contrast with [124], the proposed registration allows to evaluate the non overlapping area locally. Consequently, the contribution of this revisited method is the ability to handle the drop-outs and unreliable parts of the prosthesis captured in radiographs. As the contour detection and a feature matching are not required by the intensity-based registration, the computation is much more simple in comparison with the previously published approaches. Therefore, the method is straightforward for efficient acceleration using graphics adapters. The study presents *in silico* and phantom evaluations of the proposed approach.

5.2 MATERIAL

The study was performed involving SLR-PLUS Cementless Revision Stem, Zweymüller system produced by Smith&Nephew, Inc. The femoral stem was attached to a phantom containing 10 tantalum beads of 1 mm diameter provided by X-medics Scandinavia. The phantom was a box with dimensions $200 \times 130 \times 30$ mm, created from extruded Plexiglas® of 6 mm thickness by Koplast s.r.o. manufacturer. A complete assembly is shown in Figure 5.1. A polygonal model of the

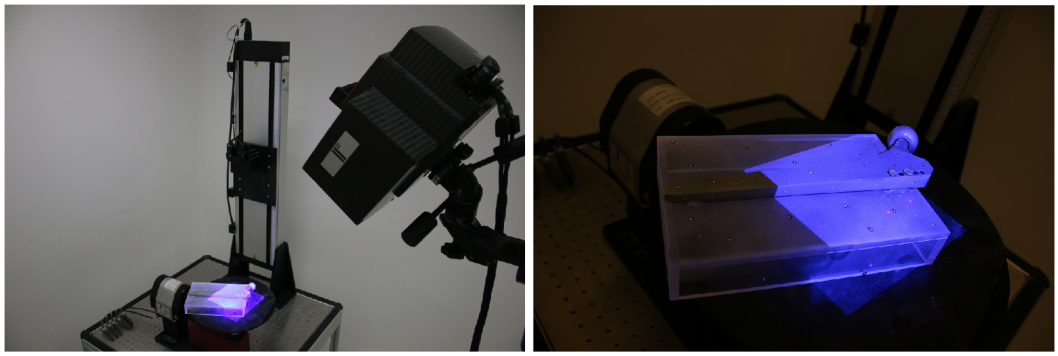

Figure 5.2: Scanning of the phantom assembly.

implant was generated using ATOS TripleScan II system and ATOS Professional v8 SR1 software. The final model used for both *in silico* and phantom evaluations was formed by 236,053 vertices and 470,337 polygons. A mutual pose of the implant and the phantom box was determined by additional scanning the assembly, as shown in Figure 5.2. Final positions of the tantalum markers with respect to the prosthesis were calculated, as their locations inside the phantom were defined by the CAD model, used for manufacturing the box.

The Carestream Directview DR 9500 System was exploited for sequential capturing of digital radiographs (DR). The phantom assembly was inserted into a biplanar calibration cage filled with 36 tantalum beads. We used direct linear transform (DLT)[4] for the radiographs calibration, as proposed by Choo [22], instead of the traditional fiducial-control planes (FCP) approach [104]. The assembly was rotated approximately 45 °around the prosthesis proximodistal axis to prevent occlusions of the phantom markers by the implant. The complete experimental set up is shown in Figure 9.6.

For the phantom study, 8 radiographs were captured from each anterior-posterior and lateral views. Pose of the calibration box within the imaging system was varied among the individual acquirements. The radiographs were enhanced using an intensity curve adjustment and histogram equalization. Upon the radiographs, a set of 64 stereo pairs was constructed, an example stereo pair of radiographs is shown in Figure 5.4. Randomly chosen 32 pairs were exploited for a precise refinement of the mutual pose between the phantom and the implant, the remaining half was used for the evaluation.

5.3 METHOD

The proposed registration is suitable for usage with both binary segmentations or enhanced non segmented radiographs.

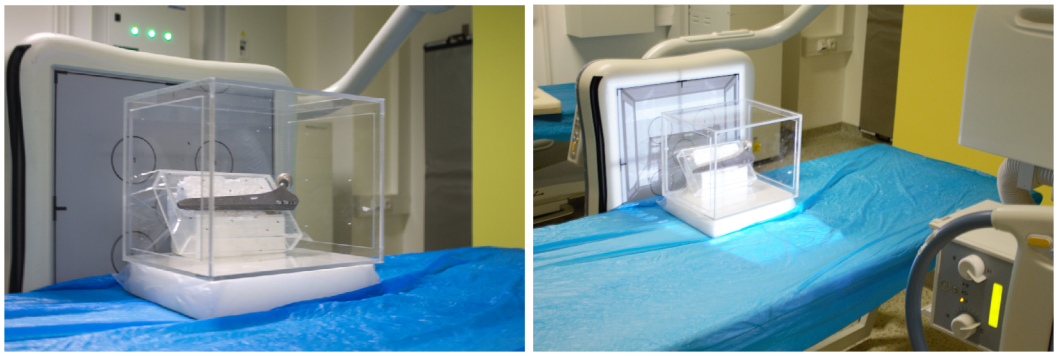

Figure 5.3: The phantom with attached prosthesis inside the calibration box, placed into the uniplanar imaging system. The phantom was firmly fixed to the calibration box.

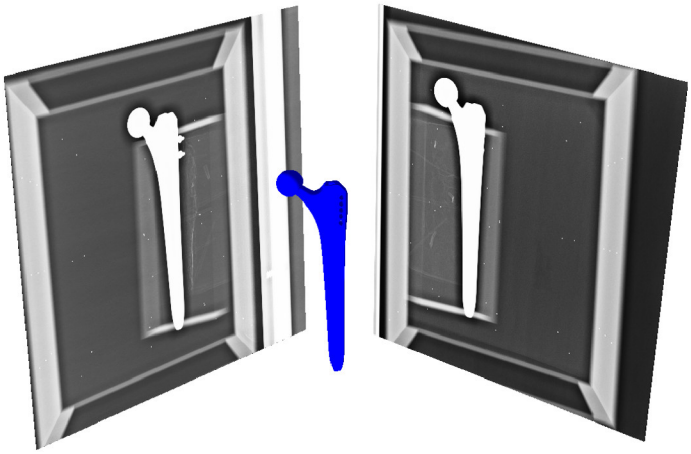

Figure 5.4: A stereo pair of enhanced radiographs with the RE model of the replacement. The model is in the ground-truth pose, determined using tantalum beads inside the phantom.

5.3.1 *Binary Images*

As the metallic implants are highly radiopaque, the segmentation is performed by thresholding the enhanced radiographs; pixels representing the prosthesis are set to 1. A coarse initial estimate of the prosthesis pose must be provided by the user. During the registration, binary digitally reconstructed radiographs (DRR) are rendered from the prosthesis model. Following [124], the non overlapping area is defined as the area that the segmentations of real and calculated radiographs do not have in common. The size of the area is equal to the count of different pixels between the real and virtual segmentations. Since the segmentations contain only

Figure 5.5: Non overlapping area between the actual and reprojected prosthesis segmentation. The error is set to $R_{err} = (4.59, -3.68, -2.38)°$ and $T_{err} = (-1.31, 1.07, -1.03)$ mm. The size of non overlapping area is 27.5%.

binary values, the count is computed by summing squares of the pixel differences (PD):

$$PD(\mathcal{P}, x, y) = DR(x, y) - DRR(\mathcal{P}, x, y) \tag{5.1}$$

$$NOA(\mathcal{P}) = \sum_{x,y} \|PD(\mathcal{P}, x, y)\|^2 \tag{5.2}$$

where $\mathcal{P} = (R, T)$ is a vector formed by a rotation and translation of the prosthesis model in the space of stereo radiographs. To eliminate different radiograph resolutions or perspective scaling, it is convenient to express the non overlapping area size in a relative form as $\frac{NOA(\mathcal{P})}{NOA(\mathcal{P})+C(\mathcal{P})}$, where $C(\mathcal{P})$ is a count of overlapping pixels. The metric is schematically depicted in Figure 9.3. The minimization of non overlapping area for anterior-posterior (AP) and lateral (LAT) views is formulated as non-linear least squares (NLS) problem:

$$(\mathcal{P}^*) = \underset{\mathcal{P}}{\operatorname{argmin}} \left[NOA_{AP,LAT}(\mathcal{P}) \right] \tag{5.3}$$

5.3.2 *Non Segmented Radiographs*

Due to the significant radiopacity, it is assumed the metallic prostheses are objects with the highest contrast in radiographs, exceeding the brightness of the surrounding bone, soft tissues or eventual cement layer, which makes the segmentation rather a straightforward task. On the other hand, a precise segmentation may demand some additional user interaction and consequently, to decrease the amount of required user efforts, it is convenient to perform the registration using directly the non segmented radiographs. In case of the proposed intensity-based registration, radiographs are preprocessed using the histogram equalization. After the preprocessing, pixels representing the prosthesis reach approximately the maximum value of the image intensity range. The digitally reconstructed radiographs contain only two intensity levels. Following the radiopacity assumption, the virtual model is rendered with the highest contrast, while the background pixels are set

Figure 5.6: A femoral stem with attached ball head (left), ball head occluded by the acetabular prosthesis (middle), blue colored drop-out area roughly selected by a user (right).

to the lowest intensity. As the intensity-based non overlapping area registration is formulated as a least squares problem, it is clearly suitable for usage with gray-scale images. With respect to the high prosthesis radiopacity and the least squares formulation of the registration, the equalized radiographs may be considered as a probabilistic approximation of the prosthesis segmentation. However, in this case the sum of squared differences does not correspond to the exact size of the non overlapping area, in contrast with the registration involving only the binary segmentations.

5.3.3 *Handling Drop-outs*

Drop-outs are especially related with metallic objects, that are not a part of the prosthesis virtual model, but which are present in radiographs and occlude certain parts of the implant. In case of hip prosthesis, the ball head attached to the femoral stem may be occluded by a metallic acetabular implant. In this case, a user must roughly select the area, where a boundary of the prosthesis, corresponding to the virtual model, is unclear. The situation is schematically illustrated in Figure 5.6. Consequently, the drop-out areas are discarded from both input X-ray images and digitally reconstructed radiographs, hence they do not affect the registration accuracy. The drop-outs are supported by both segmentation-based and intensity-based registrations. However, they were not supported by the original contour-based approach [124], as it required a complete and precise outline of the prosthesis to be extracted from the input radiographs.

5.3.4 *Optimization Scheme*

During the registration, 6 degrees-of-freedom (DOF) of the model pose are optimized using Levenberg-Marquardt numerical solver [KKŠZ16a]. As the Levenberg-Marquardt optimization is gradient-based, an evaluation of Jacobian matrix J_F is

required during each iteration [59]. The matrix contains partial derivatives of pixel differences with respect to the pose parameters:

$$J_F = \left.\begin{pmatrix} \frac{\partial PD(\mathcal{P},1,1)}{\partial[r_x,r_y,r_z]} & \frac{\partial PD(\mathcal{P},1,1)}{\partial[t_x,t_y,t_z]} \\ \vdots & \vdots \\ \frac{\partial PD(\mathcal{P},x,y)}{\partial[r_x,r_y,r_z]} & \frac{\partial PD(\mathcal{P},x,y)}{\partial[t_x,t_y,t_z]} \end{pmatrix}\right\} w_{AP}h_{AP} + w_{LAT}h_{LAT} \tag{5.4}$$

The number of rows in J_F matrix is given by the total count of pixels in both anterior-posterior and lateral images, the number of columns is equal to the count of degrees-of-freedom. As it is not possible to evaluate the Jacobian matrix using a closed-form solution, we use a central differences approximation:

$$\frac{\partial}{\partial p}PD(p,x,y) \approx \frac{1}{2\epsilon}DRR(p+\epsilon,x,y) - \frac{1}{2\epsilon}DRR(p-\epsilon,x,y) \tag{5.5}$$

where $p \in \mathcal{P}$ is a certain pose parameter and ϵ is a difference spacing. To increase both capture range and accuracy at the same time, the registration is divided into five subsequent optimizations where the coarse-to-fine strategy is applied on the difference spacing ϵ. Stages with ϵ equal to $1e^1, 1e^0, 1e^{-1}, 1e^{-2}, 1e^{-3}$ millimeters or degrees respectively were used in the study. To speed up the registration and lower the memory requirements, only regions of interest were cropped from radiographs to form the pixel differences vector, based on bounding boxes of the implant segmentations. To prevent an undesirable cropping of the non overlapping areas, the bounding boxes were enlarged by certain margins. Due to pixel-wise formulation of the registration, places containing drop-outs, selected by the user, were simply discarded from the registration.

5.4 RESULTS

5.4.1 *In silico Evaluation*

As eventual segmentation errors may negatively affect the 2D-3D registration [74], the aim of the *in silico* evaluation was to investigate the intensity-based approach accuracy itself, without external influences. Three data sets containing one hundred virtual stereo radiographs of the implant, differing in resolution, were created with pixel spacings set to 0.5, 0.35 and 0.143 mm. The initial poses were generated randomly with uniform distribution, the maximal translational and rotational errors were limited to ± 5 mm and ± 5 °respectively. Table 9.2 shows mean values and standard deviations of absolute pose errors together with corresponding non overlapping area size, number of iterations and processing time. A relation between accuracy and pixel spacing is shown using box plots in Figure 5.7. The accuracy obviously increases with the radiographs resolution, as the registration is able to

perform more iterations. However, the rising count of iterations together with increasing length of the pixel differences (PD) vector yields into a trade-off between the registration accuracy and the processing time.

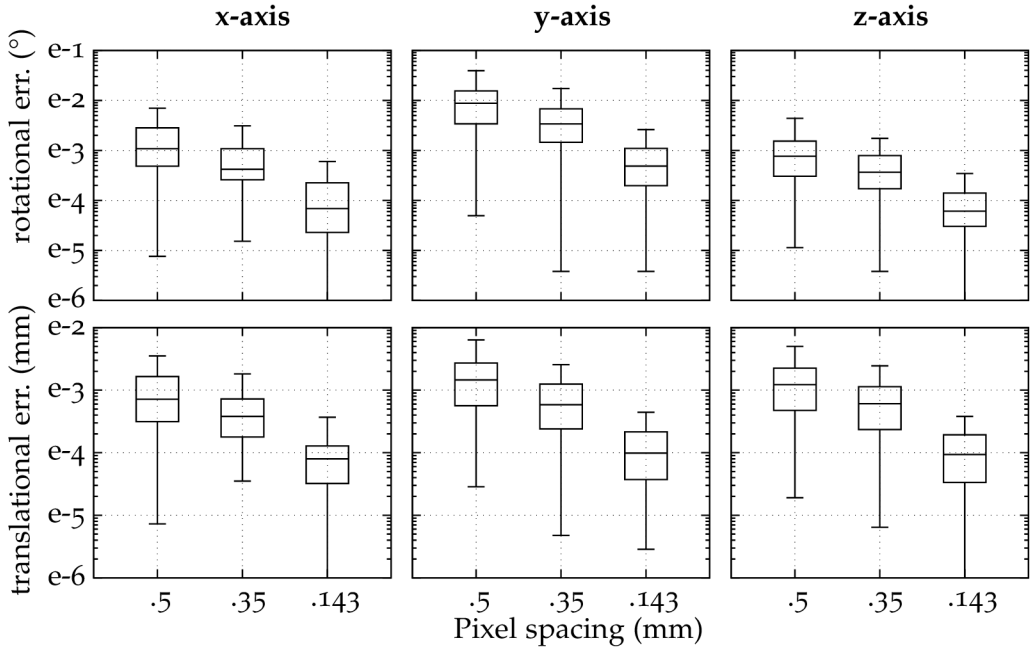

Figure 5.7: Distributions of absolute rotational and translational errors in dependence on the radiographs pixel spacing. The error distributions are shown in logarithmic scale.

5.4.2 *Phantom Evaluation*

The model-based radiostereometric analysis monitors possible changes in relative pose between the bone and the joint replacement among certain time periods. The prosthesis pose is recovered by the registration of its virtual model into a stereo pair of radiographs, while the pose of the bone is obtained using a tantalum beads placed inside the bone. The tantalum beads are inserted using commercially available injectors, provided for instance by Tilly Medical Products AB or RSA Biomedical suppliers. A three dimensional pose of the bone markers is easily obtained from the stereo radiographs by triangulation. In consequence, the prosthesis migration is measured with respect to the set of markers injected into the bone. During the phantom study, for the accuracy evaluation purposes, the ground-truth pose of the implant within the space of stereo radiographs was determined using ten tantalum markers inside the phantom Plexiglas box, as the relative pose between the phantom and the attached prosthesis was known.

The registration was evaluated for both binary and non segmented radiographic images, with and without user selected drop-outs. A sample stereo pair containing

drop-outs, chosen from the evaluation data set, is shown in Figure 5.8. The results of accuracy evaluations with and without drop-outs are shown in Tables 5.2 and 9.2 respectively, their comparison is visualized in Figure 5.9. To investigate a relation between the capture range and the registration accuracy, the evaluations were performed for different limitations of maximal errors in initial poses, revealing a gentle decrease of accuracy and higher number of iterations with rising initial pose error.

The results show the estimation of proximodistal rotation reaches the lowest accuracy in comparison with other pose parameters. The accuracy of the rotation around the y axis would be increased by involving a third radiographic image taken in proximodistal projection, allowing the registration to minimize a non overlapping area even in the xz plane. However, in a real clinical environment, it is not possible to capture a radiographic image from such projection.

Generally, the recovery of the prosthesis pose using its virtual model is possible due to sufficient asymmetry of the implant, leading to unique projections of the model [124, 56]. Therefore, dropping the ball head out from the radiographs, a significantly asymmetric part of the prosthesis, which may be on the other hand in real situation occluded by a metallic acetabular implant, has rather slight, but still recognizable influence on the registration accuracy. As the ball head is the most proximal and the most medial part of the model, a slight decrease of the accuracy can be seen mainly in the translation along the proximodistal and z axis. The method also performs for binary segmentations with slightly higher accuracy than for enhanced radiographs.

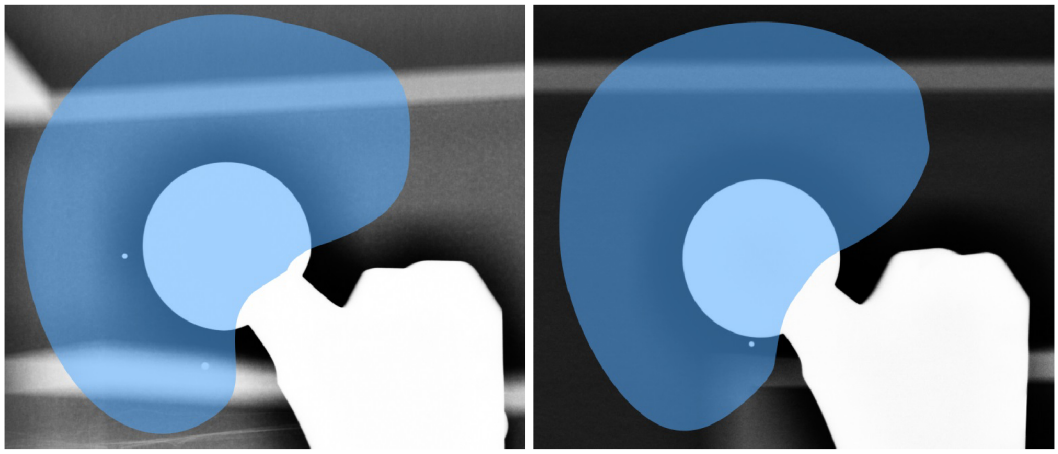

Figure 5.8: A sample stereo pair of radiographic images with roughly selected drop-out areas, chosen from the drop-outs evaluation data set. The selected areas, highlighted by blue overlay, are present in the places, where the femoral prosthesis with the attached ball head may be occluded by a metallic acetabular implant, as schematically shown in Figure 5.6.

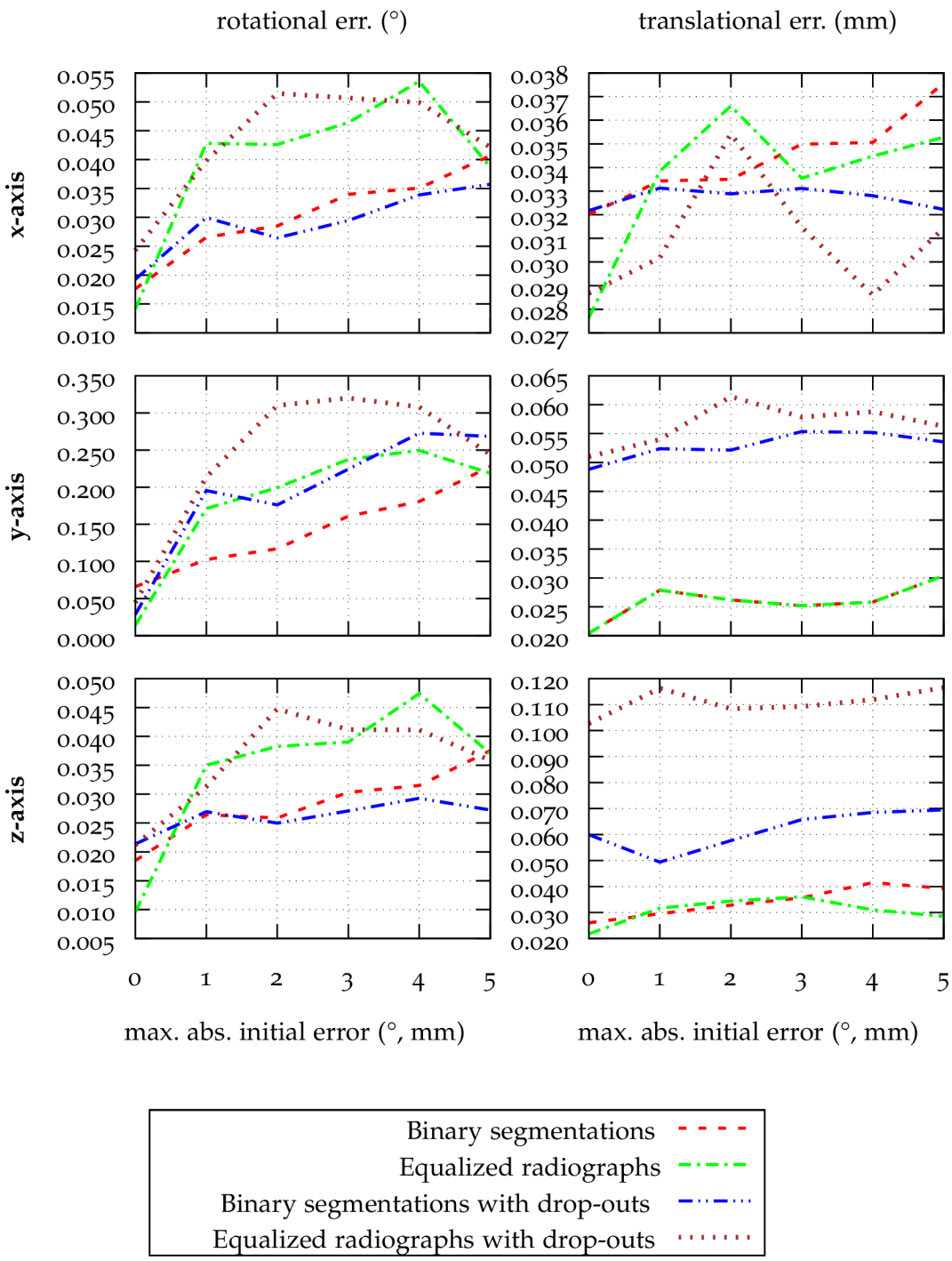

Figure 5.9: Dependence of the registration accuracy on the initial pose estimation error.

The registration pipeline was implemented using Qt Toolkit 5.8.0 and compiled with MSVC 2013 64-bit. To speed up the registration, the rendering part of the pipeline was accelerated using OpenGL 4.3. The evaluations were performed using a Microsoft Windows 8.1 64-bit desktop machine equipped with Intel Core i5-6500 CPU processor, NVidia 980 GTX Ti 6GB graphics adapter and 24GB of DDR4 SDRAM memory.

Table 5.1: Results of the accuracy and performance evaluations.

Max. initial err. (mm,°)	Spacing (mm)	Rotational error *(mean±stdev)* x (°)	y (°)	z (°)	Translational error *(mean±stdev)* x (mm)	y (mm)	z (mm)	Iters.	Time (s)	NOA (%)
In silico evaluation										
±5	0.5	0.006 ± 0.041	0.040 ± 0.170	0.006 ± 0.041	0.011 ± 0.010	0.022 ± 0.210	0.010 ± 0.081	24.6	5.2	0.197
±5	0.35	0.001 ± 0.002	0.005 ± 0.006	0.001 ± 0.008	0.001 ± 0.007	0.001 ± 0.001	0.001 ± 0.001	26.7	9.2	0.004
±5	0.143	0.000 ± 0.000	0.001 ± 0.001	0.000 ± 0.000	0.000 ± 0.000	0.000 ± 0.000	0.000 ± 0.000	31.8	44.4	0.000
Phantom evaluation using binary segmentations										
0	0.143	0.018 ± 0.015	0.066 ± 0.056	0.019 ± 0.013	0.032 ± 0.019	0.020 ± 0.010	0.026 ± 0.020	25.3	-	1.079
±1	0.143	0.027 ± 0.021	0.103 ± 0.070	0.026 ± 0.016	0.033 ± 0.019	0.028 ± 0.011	0.030 ± 0.023	54.5	-	1.080
±2	0.143	0.029 ± 0.022	0.117 ± 0.079	0.026 ± 0.018	0.034 ± 0.019	0.026 ± 0.011	0.033 ± 0.021	62.7	-	1.081
±3	0.143	0.034 ± 0.034	0.161 ± 0.230	0.030 ± 0.028	0.035 ± 0.025	0.025 ± 0.011	0.036 ± 0.028	71.3	-	1.088
±4	0.143	0.035 ± 0.037	0.181 ± 0.265	0.032 ± 0.030	0.035 ± 0.026	0.026 ± 0.011	0.042 ± 0.035	85.5	-	1.093
±5	0.143	0.041 ± 0.051	0.228 ± 0.424	0.038 ± 0.047	0.038 ± 0.030	0.030 ± 0.026	0.039 ± 0.025	98.5	108.7	1.121
Phantom evaluation using enhanced radiographs										
0	0.143	0.014 ± 0.016	0.014 ± 0.011	0.010 ± 0.010	0.028 ± 0.020	0.013 ± 0.009	0.022 ± 0.017	16.8	-	-
±1	0.143	0.043 ± 0.048	0.171 ± 0.192	0.035 ± 0.037	0.034 ± 0.024	0.028 ± 0.010	0.032 ± 0.023	43.6	-	-
±2	0.143	0.043 ± 0.062	0.199 ± 0.284	0.038 ± 0.056	0.037 ± 0.033	0.028 ± 0.012	0.034 ± 0.022	84.3	-	-
±3	0.143	0.046 ± 0.067	0.237 ± 0.376	0.039 ± 0.063	0.034 ± 0.032	0.031 ± 0.018	0.036 ± 0.026	101.4	-	-
±4	0.143	0.054 ± 0.078	0.250 ± 0.436	0.047 ± 0.076	0.035 ± 0.035	0.033 ± 0.024	0.031 ± 0.026	113.5	-	-
±5	0.143	0.039 ± 0.069	0.219 ± 0.403	0.037 ± 0.068	0.035 ± 0.036	0.031 ± 0.023	0.029 ± 0.020	120.8	188.0	-

Table 5.2: Accuracy and performance evaluation on phantom data containing drop-outs.

Max. initial err. (mm,°)	Spacing (mm)	Rotational error *(mean±stdev)* x (°)	y (°)	z (°)	Translational error *(mean±stdev)* x (mm)	y (mm)	z (mm)	Iters.	Time (s)	NOA (%)
Evaluation using binary segmentations										
0	0.143	0.019 ± 0.015	0.029 ± 0.031	0.021 ± 0.014	0.032 ± 0.018	0.049 ± 0.015	0.060 ± 0.033	22.7	-	1.090
±1	0.143	0.030 ± 0.021	0.195 ± 0.155	0.027 ± 0.016	0.033 ± 0.017	0.052 ± 0.018	0.049 ± 0.034	47.0	-	1.108
±2	0.143	0.026 ± 0.024	0.176 ± 0.154	0.025 ± 0.018	0.033 ± 0.018	0.052 ± 0.014	0.058 ± 0.039	60.1	-	1.104
±3	0.143	0.029 ± 0.024	0.224 ± 0.174	0.027 ± 0.017	0.033 ± 0.019	0.055 ± 0.020	0.066 ± 0.058	68.2	-	1.120
±4	0.143	0.034 ± 0.029	0.273 ± 0.322	0.029 ± 0.022	0.033 ± 0.021	0.055 ± 0.021	0.069 ± 0.058	79.5	-	1.150
±5	0.143	0.036 ± 0.027	0.268 ± 0.260	0.027 ± 0.018	0.032 ± 0.018	0.054 ± 0.024	0.070 ± 0.049	93.9	113.0	1.174
Evaluation using enhanced radiographs										
0	0.143	0.024 ± 0.022	0.045 ± 0.035	0.021 ± 0.021	0.029 ± 0.018	0.051 ± 0.017	0.103 ± 0.052	17.4	-	-
±1	0.143	0.040 ± 0.030	0.214 ± 0.201	0.031 ± 0.024	0.030 ± 0.019	0.054 ± 0.022	0.116 ± 0.064	41.5	-	-
±2	0.143	0.051 ± 0.047	0.310 ± 0.402	0.045 ± 0.046	0.035 ± 0.025	0.061 ± 0.019	0.108 ± 0.059	73.7	-	-
±3	0.143	0.051 ± 0.047	0.320 ± 0.389	0.041 ± 0.038	0.031 ± 0.024	0.058 ± 0.029	0.109 ± 0.053	90.0	-	-
±4	0.143	0.050 ± 0.049	0.308 ± 0.404	0.041 ± 0.036	0.029 ± 0.021	0.059 ± 0.028	0.112 ± 0.054	108.0	-	-
±5	0.143	0.042 ± 0.041	0.244 ± 0.327	0.036 ± 0.031	0.031 ± 0.021	0.056 ± 0.025	0.117 ± 0.051	115.0	188.8	-

5.5 DISCUSSION AND CONCLUSION

In contrast with 2D-3D registration methods exploiting contour difference minimization, non overlapping area does not require feature matching between detected and virtual contours, which is a computationally demanding and error prone task. Considering theoretical aspects, determining matches between the contours is in principle an ill-posed problem. Strictly speaking, there are no actual correspondences between the detected and calculated contours until the ground-truth pose of the model is recovered. In other poses, the virtual contour captures different places of the prosthesis than the edges detected in radiographs. We therefore suggest the non overlapping area has a stronger theoretical basis than the contour difference registration.

A computation of the intensity-based non overlapping area is more straightforward in comparison with the original feature-based formulation. In the feature-based case, the area was evaluated using non-trivial procedure based on horizontal directions of both detected and virtual contours [124]. On contrary, the intensity-based variant exploits plain pixel differences between radiographs and virtual segmentations obtained from the prosthesis model.

As the OpenGL acceleration was focused only on the part of the pipeline, data transfers between a graphical and operational memory were a cause of a performance bottleneck. There is an opportunity for further significant acceleration by implementing the rest of the registration pipeline using the OpenGL compute shader programs, eliminating the memory transfers and exploiting parallelization of the Levenberg-Marquardt algorithm. We believe the shift from the feature to intensity-based variant is possible due to rapid progress of hardware performance, as the intensity-based registration feasibility depends on usage of modern hardware resources.

Due to efficient graphics hardware and intensity-based formulation, it is possible to involve complete high-poly RE models without decimating the mesh, in contrast with studies presented by [56, 102]. The registration accuracy is comparable with previously published feature-based approaches, according to the summary presented by [118]. However, the comparison is rather tentative, as the accuracy depends on the shape of involved implants [57] and on the type of imaging system. An important contribution of the intensity-based revision is the ability to handle the drop-outs, which are useful for dealing with components that are not a fixed part of the prosthesis model. We also suggest the relative size of non overlapping area is a simply interpretable metric, useful for indicating the resulting accuracy of the registration.

CONFLICT OF INTEREST STATEMENT

The authors declare no conflict of interest.

ACKNOWLEDGEMENTS

We would like to thank Pavel Stoklasek and Ales Mizera for capturing the RE model of the prosthesis and Adela Chroboczkova for designing CAD drawings of the phantom. This work has been supported by the Internal Science Fund of Brno University of Technology grant no. FEKT/FIT-J-17-4745 Intermodal Registration of 3D Data in Health-care and by the Technology Agency of the Czech Republic grant no. TE01020415 V3C - Visual Computing Competence Center.

5.6 APPENDIX

Note on Least Squares Formulation of Non-Overlapping Area Registration

The intensity-based revision of non-overlapping area metric uses binary masks instead of implant or model contours. The measure is evaluated as a sum of squared differences, as shown in the following equations using a matrix notation. The DR is a binary mask obtained from the input digital radiograph, DRR is a digitally reconstructed radiograph capturing the model rendered with respect to the pose parameters $\mathcal{P}$ and PD is a vector of pixel differences. As the following example shows, the sum of squared differences between the binary masks is equal to the count of different pixels.

$$\mathrm{PD}(\mathcal{P}) = \mathrm{DR} - \mathrm{DRR}(\mathcal{P}) \tag{5.6}$$

$$\mathrm{PD}(\mathcal{P}) = \begin{bmatrix} 0 & 0 & 0 & 0 & 0 \\ 0 & 1 & 1 & 0 & 0 \\ 1 & 1 & 1 & 1 & 0 \\ 1 & 1 & 1 & 1 & 0 \\ 0 & 1 & 1 & 0 & 0 \\ 0 & 0 & 0 & 0 & 0 \end{bmatrix} - \begin{bmatrix} 0 & 0 & 0 & 0 & 0 \\ 0 & 0 & 1 & 1 & 0 \\ 0 & 1 & 1 & 1 & 1 \\ 0 & 1 & 1 & 1 & 1 \\ 0 & 0 & 1 & 1 & 0 \\ 0 & 0 & 0 & 0 & 0 \end{bmatrix} = \begin{bmatrix} 0 & 0 & 0 & 0 & 0 \\ 0 & 1 & 0 & -1 & 0 \\ 1 & 0 & 0 & 0 & -1 \\ 1 & 0 & 0 & 0 & -1 \\ 0 & 1 & 0 & -1 & 0 \\ 0 & 0 & 0 & 0 & 0 \end{bmatrix} \tag{5.7}$$

$$\mathrm{NOA}(\mathcal{P}) = \|\mathrm{PD}(\mathcal{P})\|^2 = \mathrm{trace}(\mathrm{PD}^{\mathrm{T}}\mathrm{PD}) \tag{5.8}$$

$$\mathrm{NOA}(\mathcal{P}) = \mathrm{trace}\left(\begin{bmatrix} 0 & 0 & 1 & 1 & 0 & 0 \\ 0 & 1 & 0 & 0 & 1 & 0 \\ 0 & 0 & 0 & 0 & 0 & 0 \\ 0 & -1 & 0 & 0 & -1 & 0 \\ 0 & 0 & -1 & -1 & 0 & 0 \end{bmatrix} . \begin{bmatrix} 0 & 0 & 0 & 0 & 0 \\ 0 & 1 & 0 & -1 & 0 \\ 1 & 0 & 0 & 0 & -1 \\ 1 & 0 & 0 & 0 & -1 \\ 0 & 1 & 0 & -1 & 0 \\ 0 & 0 & 0 & 0 & 0 \end{bmatrix} \mathrm{phantoma} \right) \tag{5.9}$$

$$\mathrm{NOA}(\mathcal{P}) = \mathrm{trace}\left(\begin{bmatrix} 2 & 0 & 0 & 0 & -2 \\ 0 & 2 & 0 & -2 & 0 \\ 0 & 0 & 0 & 0 & 0 \\ 0 & -2 & 0 & 2 & 0 \\ -2 & 0 & 0 & 0 & 2 \end{bmatrix} \right) = 8 \tag{5.10}$$

Consequently, it is possible to formulate the registration as a non-linear least squares problem and involve the Levenberg-Marquardt optimizer. In contrast with the contour-based approach, the optimizer works directly with the residual vector instead of a scalar-valued objective function, and the non-overlapping area size is evaluated implicitly by the solver.

5.6.1 *Radiographs Acquisition*

In addition to the uniplanar DIRECTVIEW DR 9500 Carestream radiographic facility, a biplanar fluoroscope manufactured by the Innova vendor was tested for the radiographs acquisition. However, despite the benefit of synchronized radiographs capturing, the fluoroscopic images were not used due to lower resolution and contrast, when compared to the radiographic images taken using the uniplanar DIRECTVIEW machine. Capturing the fluoroscopic images is shown in Figure 5.10.

5.6.2 *Shoulder Prosthesis*

Beyond the femoral stem and radial plate, also a shoulder implant shown in Figures 5.11 and 5.12 was involved in initial experiments. However, due to a difficult attachment to a Plexiglass phantom, the implant was not used for further evaluations.

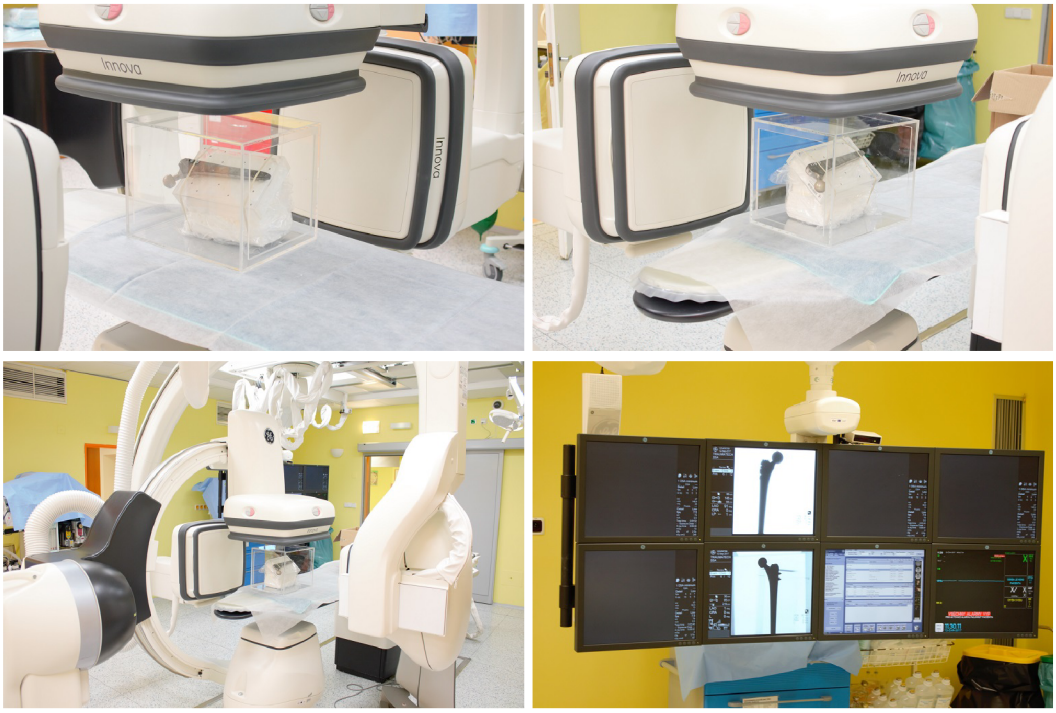

Figure 5.10: Capturing radiographs of femoral stem using Innova fluoroscope.

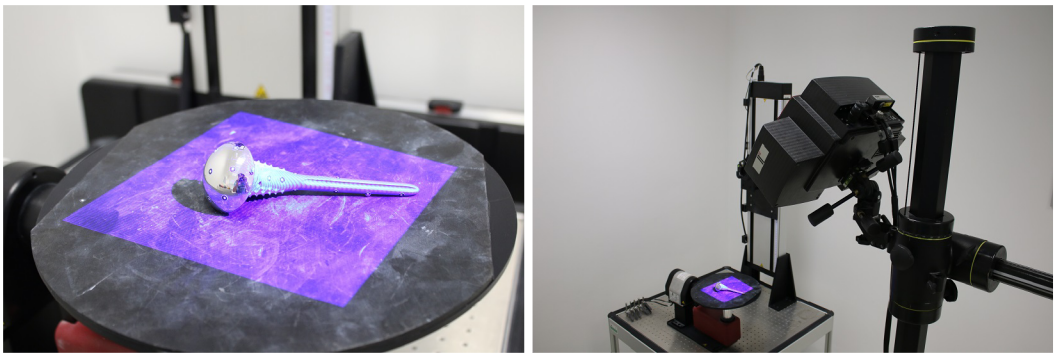

Figure 5.11: Scanning of the shoulder implant.

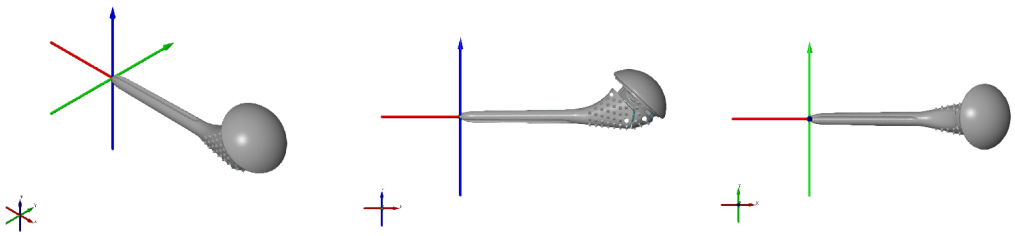

Figure 5.12: Virtual model of the shoulder implant.

6

INTENSITY-BASED FEMORAL ATLAS 2D/3D REGISTRATION USING LEVENBERG-MARQUARDT OPTIMISATION

CITATION

[KKŠZ16a] Ondřej Klíma, Petr Klepárník, Michal Španel, and Pavel Zemčík. Intensity-based femoral atlas 2D/3D registration using Levenberg-Marquardt optimisation. In *Medical Imaging 2016: Biomedical Applications in Molecular, Structural, and Functional Imaging*, volume 9788, pages 113 – 124. International Society for Optics and Photonics, SPIE, 2016. doi: 10.1117/12.2216529

ABSTRACT

The reconstruction of a patient-specific 3D anatomy is the crucial step in the computer-aided preoperative planning based on plain X-ray images. In this paper, we propose a robust and fast reconstruction methods based on fitting the statistical shape and intensity model of a femoral bone onto a pair of calibrated X-ray images. We formulate the registration as a non-linear least squares (NLS) problem, allowing for the involvement of Levenberg-Marquardt optimisation. The proposed methods have been tested on a set of 96 virtual X-ray images. The reconstruction accuracy was evaluated using the symmetric Hausdorff distance between reconstructed and ground-truth bones. The accuracy of the intensity-based method reached 1.23 ± 1.65 mm on average.

KEYWORDS

Preoperative planning, image registration, 2D/3D reconstruction, statistical shape and intensity model, Levenberg-Marquardt optimisation, GPU acceleration

6.1 INTRODUCTION

In the field of the orthopaedic traumatology, surgical intervention is often preceded by a preoperative planning. The common aim of the preoperative planning is to get acquainted with the bone fracture and to at least roughly plan repositioning of the bone fragments. If the reposition is done virtually using 3D planning software, precise identification of the best shaped patient-specific bone plate is possible as well. Typically, the treatment of a traumatized bone requires Radiography (X-ray) and, in the difficult cases, the computed tomography (CT) examination is needed as well. The virtual planning is typically based on 3D models of bones or their fragments usually extracted from CT data sets captured with high level of detail. However, in comparison to the plain X-ray imaging, in case of CT, the patient is exposed to higher radiation doses during the CT examination [129]. In addition, the CT imaging is more time consuming and more expensive. Therefore, preoperative planning based on plain X-ray images has been brought into focus in recent years. For the purposes of the planning, it is important to reconstruct the 3D patient-specific anatomy. The reconstruction is usually achieved by a deformable 2D/3D registration of the shape prior into the set of co-registered X-ray images.

To satisfy requirements of the involvement in clinical planning software, the 2D/3D reconstruction method must be reliably robust and fast. As the registration is an iterative process, its performance depends mainly on the rate of convergence of the involved optimisation method. Another important performance factor is the level of parallelization of the time demanding parts of the registration pipeline. We propose three considerable fast methods. The first proposed intensity-based method is capable of recovering the surface and even internal structures of the reconstructed bone, bringing more benefits to the pre-operative planning. The next two proposed *Black&White (BW)* methods focus only on the surface reconstruction, but outperform the intensity-based method in speed or accuracy, depending on the global or local formulation of the registration. It is assumed that the bone background is segmented out from the original X-ray images by the user in a semiautomatic manner.

The main contribution of the paper is the formulation of the registration in such a manner that it can be solved using the Levenberg-Marquardt optimisation algorithm [59], which is a well established numerical method with a high rate of convergence and its involvement leads to a significant speed-up of the registration. For orientative comparison, Ehlke's intensity-based method [32] takes 1:41 minutes on average for one pelvic bone reconstruction, while our intensity-based method requires only 8.8 seconds on average to reconstruct a femoral bone. The second contribution is the formulation of the local similarity evaluation, leading to highly

accurate deformable registration. The last contribution is the acceleration of certain parts of the registration pipeline using the graphics hardware.

The rest of the paper is organized as follows. There is a brief summary of the related literature with a particular focus on the intensity-based reconstruction methods in Section 2. The novel Levenberg-Marquardt based methods are proposed in Section 3 and their evaluation is reported in Section 4. Section 5 concludes the paper.

6.2 RELATED WORK

Two major categories of previously published 2D/3D reconstruction approaches can be distinguished. The first category comprises of methods based on features, usually edges or bone silhouettes extracted from the original X-ray images, and from the statistical shape model (SSM). The second category is formed by intensity-based methods, which work directly with pixels contained in the original X-ray images, and pixels rendered from the statistical appearance model. The categories differ in the anatomy features they are able to reconstruct, involved shape prior and their performance. The feature-based methods usually use a polygonal mesh SSM which makes them eligible only for the reconstruction of the bone shape, while the intensity-based methods involve a statistical appearance model and therefore, beyond the bone shape, they are commonly capable of reconstructing the bone densities and consequently the anatomy features such as compact and spongy bone. On the other hand, it requires considerably less effort to construct a plain shape model in comparison with training an appearance model. In addition, there are more stringent requirements for the training data of the appearance model, as CT data sets must be captured with the same X-ray energy. Also, the extraction of shape model features is more straightforward and efficient than the extraction of the bone densities from the appearance model. Methods from both categories require close manual initialization.

Yao proposed an intensity-based method for the reconstruction of pelvic and femoral bones. The major contribution of his work was the proposal of novel shape and appearance prior named statistical shape and intensity model (SSIM)[132]. The SSIM model is based on a volumetric mesh and describes bone densities using analytical functions which allow efficient manipulation with the bone geometry in comparison with the voxel-based appearance models. Yao's work was continued by Sadowsky [95], who focused on effective rendering of virtual X-ray images, also referred to as density reconstructed radiographs (DRR). Sadowsky derived his rendering approach from the projected tetrahedra (PT)[108] algorithm, replaced the numerical evaluation of integrals of the rays intersecting the SSIM by the closed

formula solution and involved the graphics processing unit (GPU) acceleration of the proposed method. He further extended his approach[96] and exploited it for the reconstruction of the pelvic bone from X-ray images with limited field of view [97]. The rendering approach was partially adopted by Ehlke [32], who focused on the full OpenGL acceleration of the DRR generation from the Yao's SSIM. Ehlke reused the closed formula solution for the ray integrals computation, but proposed novel approach for the tetrahedron thickness calculation instead of PT based method. He used the method for the single view registration of the pelvic bone. Gong involved the SSIM based deformable registration for the simultaneous fractured distal radius reduction and 2D/3D reconstruction [35]. Intensity-based reconstruction approaches using special appearance models were also investigated. Lamecker investigated the usability of the thickness images instead of DRRs for the intensity-based reconstruction of a pelvis [68]. Hurvitz constructed a statistical appearance model capturing whole CT data sets instead of modeling only the bone of interest [48]. The registration took advantage from authentically looking DRRs containing the anatomy of interest including the surrounding soft tissues and bone joints. Tang proposed a method based on a special shape model comprising of not intersecting spheres [119].

Beyond the methods listed above, feature-based approaches focused on a femoral bone reconstruction were proposed by Zheng [133] and Baka [11]. Zheng presented a reconstruction of the proximal femur using a method based on 3D similarity metric and establishment of correspondences between the 2D bone silhouettes and the 3D shape model. He assumed that the bone silhouettes are extracted from the original X-ray images by the user in a semiautomatic manner. Baka proposed a method combining the 3D similarity metric with the automatic extraction and selection of the relevant bone silhouettes from the X-ray images.

Yao also investigated factors affecting the deformable registration accuracy [131]. He found out that the best accuracy with respect to the running time is achieved when using two X-ray images. The experiments we performed revealed that the reconstruction error is minimal when the X-ray images are orthogonal. On the contrary, the view angles between the X-ray planes and the captured bone have no significant effect on the reconstruction accuracy. As expected, the reconstruction error is highly correlated with the X-ray images noise level, distortion and co-registration error.

The 2D/3D registration methods generally involve numerical optimisation. Most methods exploit various modifications of the gradient-descent algorithm [30, 32]. Downhill Simplex optimiser was used by Sadowsky. Gong employed the covariance matrix evolution strategy (CMA-ES) [41].

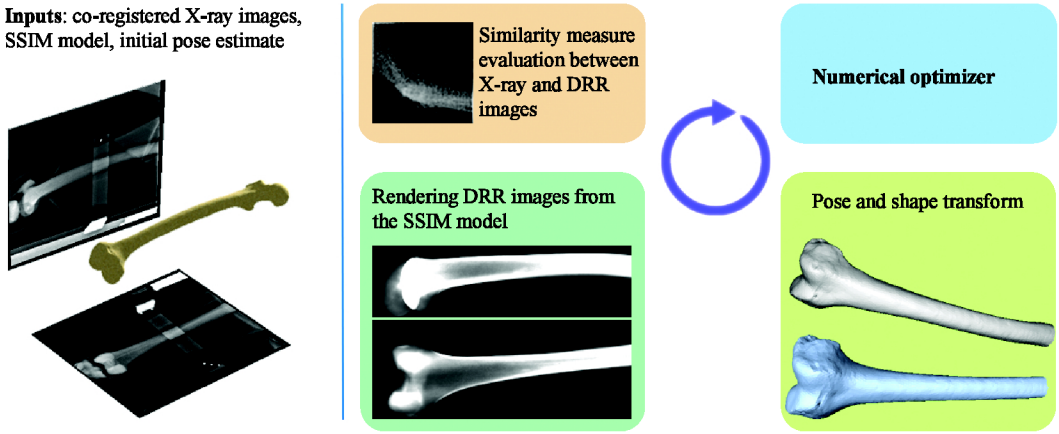

Figure 6.1: General scheme of the deformable 2D-3D registration process.

For the proposed intensity-based method, we have adopted Yao's SSIM appearance model [132] and partially Ehlke's accelerated reconstruction approach [32]. We replaced the gradient-descent based optimisation by the Levenberg-Marquardt method. The improved method significantly outperforms the Ehlke's original approach in the registration speed. To the best of our knowledge, no Levenberg-Marquardt algorithm based registration method has been proposed so far.

6.3 METHOD

The pipeline for the 2D/3D registration of the SSIM into the set of calibrated X-ray images is built as numerical optimisation. In each iteration, DRRs are rendered from the shape and intensity model. Differences between the original X-ray images and the corresponding DRRs are evaluated using an image similarity measure. The initial pose and shape parameters of the shape model are then adjusted to minimize the dissimilarities between original and rendered images. The patient-spefic bone model is reconstructed when the similarity between the DRR and X-ray images is maximal. The registration scheme is depicted in Figure 6.1. Accordingly to Yao's investigation of the accuracy factors, we reconstruct the 3D bone model from two orthogonal radiographs, usually taken from the anterior-posterior (AP) and lateral (LAT) view.

6.3.1 *Statistical Shape and Intensity Model (SSIM)*

We have largely adopted the Yao's SSIM appearance model which describes the shape variability of femur using a point distribution model (PDM) [24] and a reference tetrahedral mesh of the femoral bone. PDM is trained from tetrahedral meshes extracted from 22 CT data sets obtained from virtual skeleton database (VSD)[63].

The meshes have been brought into correspondence using the `Elastix` software [64] and aligned using the Generalized Procrustes Analysis (GPA) with the omitted re-scaling step. The linear model of the following form has been obtained by applying the Probabilistic Principal Component Analysis (PPCA)[16]:

$$S = \phi_s \mathbf{b} + \overline{S} + \epsilon_s \tag{6.1}$$

where S is the volumetric bone model generated according to the given shape parameters $\mathbf{b}$, $\overline{S}$ is the mean bone shape, ϕ_s is the matrix of principal components and ϵ_s is a zero-mean Gaussian-distributed noise. The count n_b of the shape parameters, strictly lesser than the number of bones in the training set, can be chosen arbitrarily. In contrast to Yao, we have created the femoral volumetric mesh following the Si's Delaunay-based tetrahedralization [109]. The constructed tetrahedral model, illustrated in Figure 6.2 left, contains 104 thousand of tetrahedra and 26 thousand of vertices. According to Yao, the bone density is described in each tetrahedron independently using Bernstein polynomials:

$$D(\mu) = \sum_{\forall i,j,k,l \in \mathbb{Z} \wedge i+j+k+l=n} C_{i,j,k,l} B^n_{i,j,k,l}(\mu) \tag{6.2}$$

where $D(\mu)$ is a bone density in a certain point inside the tetrahedron, μ is a barycentric coordinate of that point, n is a degree of the Bernstein polynomial, $C_{i,j,k,l}$ are the polynomial coefficients and $B^n_{i,j,k,l}$ is the Bernstein basis function:

$$B^n_{i,j,k,l}(\mu) = \frac{n!}{i!j!k!l!} \mu_x^i \mu_y^j \mu_z^k \mu_w^l \tag{6.3}$$

We have involved polynomials of the 2^{nd} degree resulting in requirement of 10 coefficients per tetrahedron. The coefficients have been obtained by solving an over-constrained system of linear equations as shown in Ref. 132. The generative model describing bone densities has been created using PPCA:

$$C = \phi_d e + \overline{C} + \epsilon_d \tag{6.4}$$

where C is a vector containing $C_{i,j,k,l}$ coefficients for each tetrahedron in the bone model, generated w.r. to the density parameters e, $\overline{C}$ is a vector of mean coefficients, ϕ_d is a matrix of principal components and ϵ_d is noise.

6.3.2 *Digitally Reconstructed Radiographs*

The rendering of virtual X-ray images is performed by a projection of the SSIM appearance model following the Ehlke's GPU accelerated approach. The X-ray beam passing through a bone is exponentially attenuated according to the Beer-Lambert law:

$$I_{out} = I_{in} e^{-\int_{w_{in}}^{w_{out}} \alpha(w)\,dw} \tag{6.5}$$

Figure 6.2: A cross-section of a tetrahedral model of the proximal femur (left). Digitally reconstructed radiographs rendered from instances of the shape and intensity model. The value of the first principal components of the left and right bone corresponds to 2σ and -2σ respectively (middle). Binary masks rendered from the same instances of the PDM (right).

where I_{in} is the intensity of the beam entering the bone at the Cartesian coordinates w_{in}, I_{out} is the output intensity of the attenuated beam at the point w_{out} and $\alpha(w)$ is linear attenuation coeffiecient of a tissue. The overall attenuation encountered by the beam passing the single tetrahedron is determined by the closed-form expression:

$$\int_{w_{in}}^{w_{out}} D(\mu)d\mu = \|w_{out} - w_{in}\| \sum_{\forall i,j,k,l \in \mathbb{Z} \wedge i+j+k+l=n}^{n} C_{i,j,k,l} \int_{\mu_{in}}^{\mu_{out}} B^{n}_{i,j,k,l}(\mu)d\mu \tag{6.6}$$

where μ_{in} and μ_{out} are the barycentric coordinates of the ray entrance and exit respectively. Because the limits of the definite integrals of the Bernstein basis functions are in barycentric coordinates, the overall sum has to be multiplied by the actual distance between the w_{in} and w_{out} points. The definite integral of the Bernstein basis function has the following closed-form solution according to Sadowsky[95]:

$$\int_{\mu_{in}}^{\mu_{out}} B^{n}_{i,j,k,l}(\mu)d\mu = \frac{1}{n+1} \sum_{i' \le i, j' \le j, k' \le k, l' \le l} B^{i'+j'+k'+l'}_{i',j',k',l'}(\mu_{in}) B^{i-i'+j-j'+k-k'+l-l'}_{i-i',j-j',k-k',l-l'}(\mu_{out}) \tag{6.7}$$

For more details we refer to Ref. 95. The computation of the overall attenuation is performed using OpenGL fragment shaders as proposed by Ehlke[32]. Sample virtual X-ray images rendered from the different parts and instances of the constructed SSIM model are depicted in Figure 6.2 middle.

6.3.3 *Intensity-based Registration*

The intensity-based registration is performed by minimizing differences between the original radiographs and the DRRs rendered from SSIM. As the CT imaging

is performed with higher X-ray energy than the plain radiography, the X-ray and DRR images may differ in contrast of corresponding tissues. Therefore, we involve the normalized mutual information (NMI) similarity measure [52], commonly used in inter-modal registration.

We set the similarity vector F to be:

$$F(\beta) = \begin{pmatrix} \mathrm{NMI}_{AP}(\beta), & \mathrm{NMI}_{LAT}(\beta) \end{pmatrix} \tag{6.8}$$

where $\beta = (R, T, b)$ concatenates the rotation, translation and shape parameters of SSIM respectively. NMI_{AP} and NMI_{LAT} describe the similarity between the radiographs and corresponding DRRs rendered with respect to the β parameters. If the radiographs and DRRs are exactly the same images, then $F(\beta) = F_{max} = \begin{pmatrix} 2, & 2 \end{pmatrix}$. The optimisation recovers the ideal parameter vector β in non-linear least squares manner:

$$\underset{\beta}{\operatorname{argmin}} = \big(F_{max} - F(\beta)\big)\big(F_{max} - F(\beta)\big)^{T} \tag{6.9}$$

The least squares problem is solved using the Levenberg-Marquardt algorithm. The Levenberg-Marquardt method performs local optimisation and therefore the close initial estimate of the SSIM pose has to be provided by the user. In each iteration, the change δ of the parameter vector β is obtained by solving the equation:

$$\big(J_F^T J_F + \lambda \mathrm{diag}(J_F^T J_F)\big)\delta = J_F^T \big(F_{max} - F(\beta)\big)^{T} \tag{6.10}$$

where λ is a damping factor and J_F is the Jacobian matrix containing partial derivatives of the similarity measures with respect to the rotation, translation and shape parameters:

$$J_F = \frac{\partial F}{\partial \beta} = \begin{pmatrix} \dfrac{\partial \mathrm{NMI}_{AP}}{\partial [r_x, r_y, r_z]} & \dfrac{\partial \mathrm{NMI}_{AP}}{\partial [t_x, t_y, t_z]} & \dfrac{\partial \mathrm{NMI}_{AP}}{\partial [b_1, b_2, \ldots, b_{n_b}]} \\ \dfrac{\partial \mathrm{NMI}_{LAT}}{\partial [r_x, r_y, r_z]} & \dfrac{\partial \mathrm{NMI}_{LAT}}{\partial [t_x, t_y, t_z]} & \dfrac{\partial \mathrm{NMI}_{LAT}}{\partial [b_1, b_2, \ldots, b_{n_b}]} \end{pmatrix} \tag{6.11}$$

As it is not possible to evaluate the J_F matrix using a closed-form solution, the finite differences approximation is used:

$$\frac{\partial f_p}{\partial \beta_q} \approx \frac{f_p(\beta_q + \epsilon) - f_p(\beta_q - \epsilon)}{2\epsilon} \tag{6.12}$$

where p, q denotes the J_F matrix row and column respectively. For the pose parameters, we set the $\epsilon_r = \epsilon_t = 1$. For the shape parameters $\mathbf{b}$ the best value of ϵ_b is investigated in Section 6.4.1. In case of pose parameters, the ϵ_r, ϵ_t are in units of [°] and [mm] respectively. For the shape parameters b_v, the ϵ_{b_v} are in units of standard deviations σ_k of the v-th principal component of the SSIM. Determining of the approximated J_F matrix of size $2 \times \mathrm{count}(\beta)$ requires rendering of $2 * 2 * \mathrm{count}(\beta)$ DRRs and consequently evaluation of the same number of NMI

similarity measures. Therefore, the evaluation of the J_F matrix is the most time consuming part of the optimisation. The optimisation stops when the J_F is a zero matrix.

6.3.4 *Black & White Registration (BW)*

In contrast to the intensity-based registration, the *Black & White* pixel-based reconstruction involves a plain PDM model instead of the SSIM. In case of PDM, the DRR images are replaced by binary masks, as shown in Figure 6.2 right. The binary masks must be extracted from the original radiographs as well. The BW registration can be formulated in two ways, depending on involvement of the explicit image similarity measure.

6.3.4.1 *Sum of Squared Differences (SSD) Approach*

Beyond the binary form of the X-ray and DRR images, this approach differs from the intensity-based registration by involvement of the SSD image similarity measure instead of the NMI metric:

$$\mathrm{SSD}(\text{X-ray}, \mathrm{DRR}) = \sum_{x,y} \big(\text{X-ray}(x,y) - \mathrm{DRR}(x,y)\big)^2 \tag{6.13}$$

where the x, y are the pixel coordinates. The usage of the SSD measure is advantageous for its straightforward parallelization and consequent acceleration using the `OpenGL` fragment shaders.

6.3.4.2 *Pixel Differences (PD) Approach*

In pixel differences approach the similarity between the X-ray and DRR images is evaluated directly by the Levenberg-Marquardt method. The vector F is reformulated to contain all pixels from both AP and LAT rendered binary masks, F_{max} contains pixels from the original radiograph masks:

$$F = \begin{pmatrix} \mathrm{DRR}_{AP}\ (1,1) \\ \vdots \\ \mathrm{DRR}_{AP}\ (w_{AP}, h_{AP}) \\ \\ \mathrm{DRR}_{LAT}(1,1) \\ \vdots \\ \mathrm{DRR}_{LAT}(w_{LAT}, h_{LAT}) \end{pmatrix}^T, \quad F_{max} = \begin{pmatrix} \text{X-ray}_{AP}\ (1,1) \\ \vdots \\ \text{X-ray}_{AP}\ (w_{AP}, h_{AP}) \\ \\ \text{X-ray}_{LAT}(1,1) \\ \vdots \\ \text{X-ray}_{LAT}(w_{LAT}, h_{LAT}) \end{pmatrix}^T \tag{6.14}$$

The Jacobian matrix is reformulated in a straightforward way. Instead of the two gradient vectors for AP and LAT view, the J_F is formed by gradient vectors for each pixel of the rendered binary masks. Despite the size of the approximated J_F matrix is changed to $w_{AP}h_{AP} + w_{LAT}h_{LAT} \times count(\beta)$, the number of required rendered images remains $2 * 2 * count(\beta)$ and no evaluation of an explicit similarity measure is performed.

Instead of the global similarity between the DRR and X-ray images, this formulation enables the optimisation to focus on the similarity of the local bone features. As more precise similarity information is available for the optimisation, the convergence of the Levenberg-Marquardt method is enhanced and consequently, the higher accuracy of the deformable registration is achieved.

6.3.5 *Optimisation Scheme*

For all the methods, the process of reconstruction consists of three subsequent optimisations.

In the first stage, the rigid 2D-3D registration of the mean shaped bone to the original X-ray images is performed. As the shape variability is Gaussian-distributed and the mean shape is *a priori* the most probable to occur, the principal components $\mathbf{b}$ are set to zero values. This step is involved to avoid getting stucked local minima. The vector β is reduced only to the rotation and translation parameters:

$$\beta_1 = ([r_x, r_y, r_z], [t_x, t_y, t_z]) \tag{6.15}$$

The second stage performs reduced deformable registration. As the time consumption caused by the J_F matrix evaluation linearly depends on the number of optimised parameters, the main purpose of the stage is to speed-up the registration. The pose is optimised simultaneously with a reduced subset of the first $u < n_b$ shape parameters:

$$\beta_2 = ([r_x, r_y, r_z], [t_x, t_y, t_z], [b_1, b_2, \ldots, b_u]) \tag{6.16}$$

To reach the maximal accuracy, the pose and all the shape parameters are optimised in the last stage:

$$\beta_3 = ([r_x, r_y, r_z], [t_x, t_y, t_z], \mathbf{b}) \tag{6.17}$$

In case of the intensity-based registration, the bone densities are set to the mean values during the whole registration.

6.4 RESULTS

The proposed methods have been evaluated on the set of virtual radiographs ray-casted from segmented CT images of femora. From each CT image, 12 virtual X-rays were rendered, rotated around longitudinal axis for $0, 30, 60, \ldots, 330°$, resulting in the data set of 96 images in total. The virtual radiographs were cropped to the average size of 205×477 pixels. The initial poses of the shape model were generated randomly with a uniform distribution. According to Baka [11], the maximum difference between the initial and the ground-truth pose was limited to 10° rotation and 10 mm translation in each direction and along each axis.

Beyond the synthetic data set, the methods were evaluated using real X-ray images of phantom bones. The images were taken from AP and LAT view, their relative pose was recovered using a custom L-shaped marker. Sample phantom images are shown in Figure 6.5.

The optimisation scheme detailed in Section 6.3.5 was involved for each performed reconstruction. The subset of the first 5 principal components ($u = 5$, see Equation 6.16) was optimised in the second stage of the registration process. In case of intensity-based method, the joint histogram of size 64×64 bins is used for the NMI similarity measure evaluation.

6.4.1 *Accuracy evaluation*

To evaluate the registration accuracy, we measured the mean and maximum symmetric Hausdorff distance between the surfaces[10] of the ground-truth and the reconstructed bone model. We employed both leave-one-out and leave-all-in methodologies.

We investigated the influence of the parameter ϵ_b (see Equation 6.12) on the registration accuracy, the results are shown in Figure 6.3. The best accuracy was achieved when the value of the ϵ_b parameter was set between 1 and 1.5 standard deviation. For the rest of experiments, we set $\epsilon_b = 1\sigma$.

During the leave-one-out methodology, the bone model of currently used X-ray images was always discarded from the training data set of the used shape model. The shape models used for the evaluation were described by 18 principal components. Average results for the proposed methods are shown in Table 6.1.

During the leave-all-in methodology, the ground-truth tetrahedral model of the reconstructed bone was present in the PDM training set. For the leave-all-in evaluation, a shape model described by 20 components was used. This methodology is involved to reveal the reconstruction accuracy without the influence of PDM generality. Results of the leave-all-in methodology are shown in Table 6.2.

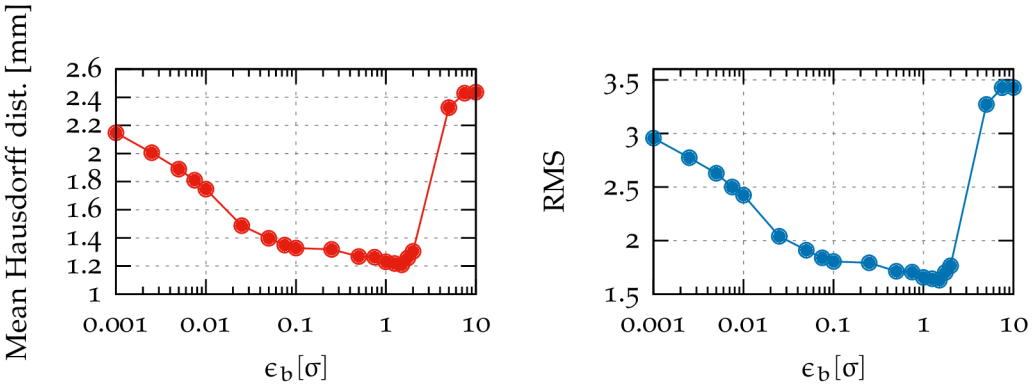

Figure 6.3: The influence of the ϵ_b parameter on the BW SSD method accuracy. The dependency of the average mean Hausdorff distance (left) and root mean square (RMS) (right) on the ϵ_b. The evaluation was performed using the leave-one-out methodology.

Table 6.1: Average reconstruction accuracy reached using the leave-one-out methodology, described by mean and maximal symmetric Hausdorff distance, rotation and translation error. Corresponding performance results are shown in Table 6.4.

Method type	Mean [mm]	RMS	Max. [mm]	r_x [°]	r_y [°]	r_z [°]	T [mm]
Intensity-based (6.3.3)	1.18	1.57	7.21	0.17	0.29	2.43	0.63
BW SSD (6.3.4.1)	1.23	1.65	7.69	0.25	0.33	2.84	0.78
BW PD (6.3.4.2)	1.02	1.35	7.10	0.16	0.18	1.55	0.55

Table 6.2: Accuracy of the methods reached using the leave-all-in methodology.

Method type	Mean [mm]	RMS	Max. [mm]	r_x [°]	r_y [°]	r_z [°]	T [mm]
Intensity-based (6.3.3)	0.71	0.94	3.99	0.11	0.22	1.83	0.48
BW SSD (6.3.4.1)	0.77	1.02	4.48	0.18	0.18	2.53	0.57
BW PD (6.3.4.2)	0.43	0.51	1.78	0.09	0.09	1.04	0.36

The results reveal that the best accuracy was reached by the BW PD method, while the accuracy of the BW SSD method was slightly worse than the results reached by the intensity-based method. The accuracy of the DW PD method is detailed using the graphs of the cumulative distributions of the Hausdorff distances in Figure 6.4. As the results show, the rotation around the longitudinal axis is difficult to recover accurately for all of the proposed methods.

The distal femur of the experimental phantom was reconstructed using the BW PD (6.3.4.2) approach. The mean Hausdorff distance between the reconstructed and the ground-truth bone surface was 1.26 ± 1.66 mm, the maximal distance was 6.62 mm. The distance between the surfaces is visualized in Figure 6.6. The silhouettes of the reconstructed model back-projected to the original X-ray images are shown in Figure 6.5.

6.4.2 *Speed Performance Evaluation*

The speed performance of the proposed methods was evaluated on a desktop machine equipped with the NVidia 980 GTX Ti 6GB graphics card, Intel i5-4460 CPU and 24GB of memory. The evaluation was focused on the number of iterations, rendered images and amount of time needed for the reconstruction.

The rendering of one DRR image and one binary mask took 0.94 ms and 0.34 ms on average respectively. We also implemented the image similarity measures computation using the OpenGL fragment programs. The OpenGL implementation was chosen to minimize the data transfers between the CPU and GPU memory and to increase the performance by the parallel computation of the similarity measures. The results of the OpenGL acceleration of the similarity metrics are shown in Table 6.3.

The acceleration led to more than twice faster evaluation of the NMI measure and more than eight times faster computation of the SSD metric. For the whole pipeline evaluation, we used the CPU implementation of the Levenberg-Marquardt method provided by the `dlib` library [62]. The speed performance results for the leave-one-out methodology are shown in Table 6.4.

The best speed-up was achieved using the BW SSD method. The OpenGL acceleration of the similarity measures computation led to the nearly double speed-up

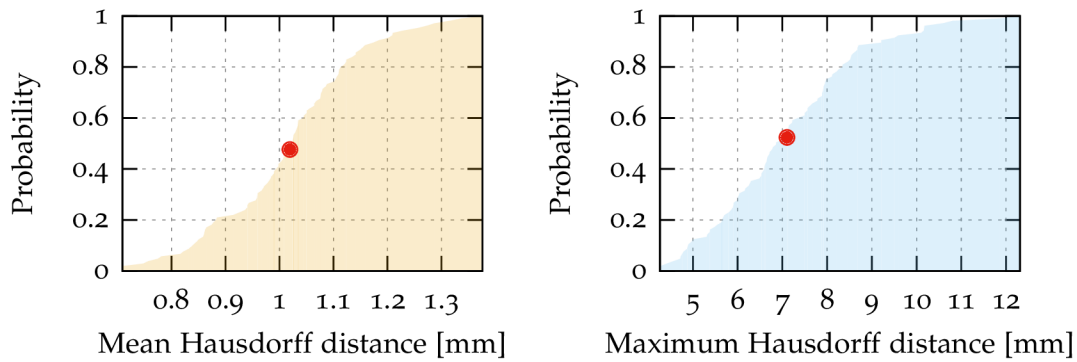

Figure 6.4: Detailed accuracy of the BW PD method. Cumulative distribution of the mean symmetric Hausdorff distance (left), cumulative distribution of the maximum error (right). The average case is highlighted by the red point.

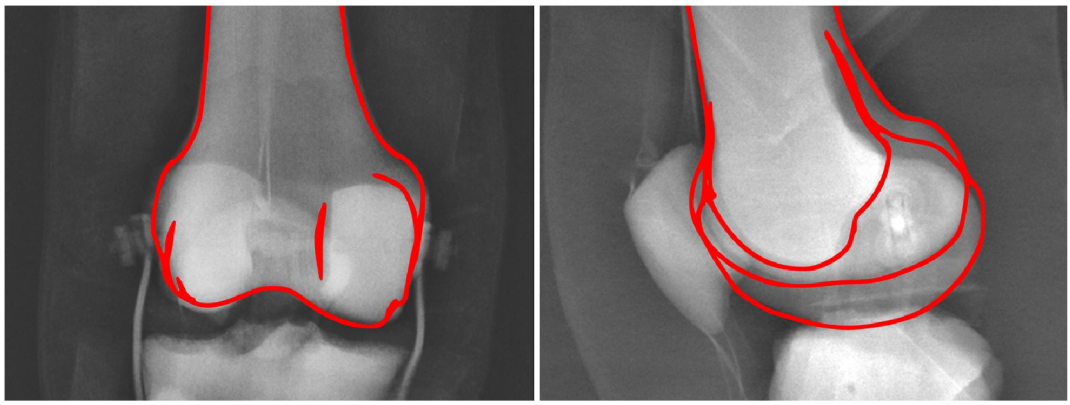

Figure 6.5: Silhouettes of the shape model fitted to the original X-ray images of a phantom. Radiographs are capturing distal femur from anterior-posterior (left) and lateral (right) view. The corresponding model of the reconstructed bone is shown in Figure 6.6.

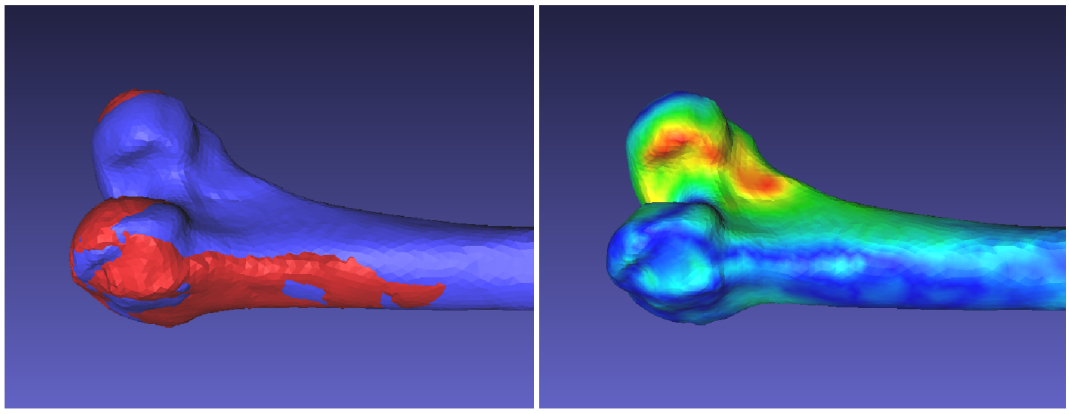

Figure 6.6: A comparison between the reconstructed and ground-truth surfaces of the phantom bone. The red colored ground-truth bone aligned to the reconstructed, blue colored bone (left). Heat-map visualization of the symmetric Hausdorff distance (right); the blue color highlights the most accurately reconstructed parts (0 mm difference), the red color shows the places with the highest registration error (6.62 mm). The original X-ray images are shown in Figure 6.5.

Table 6.3: Average time needed for a single similarity measure evaluation using the CPU and OpenGL implementations. The measurements do not include the time needed to transfer the data between the GPU and CPU memory.

Measure type	CPU time [ms]	GPU time [ms]
NMI	2.51	1.10
SSD	2.03	0.23

of the evaluated methods. The pixel differences approach faced worse performance due to the non-accelerated implementation of the Levenberg-Marquardt solver, as

Table 6.4: Comparison of an average count of iterations, images and time required by the proposed methods. The total registration time was measured using CPU and GPU implementations of the similarity measures, including the time needed for the data transfers between the system memory and a video adapter. The DRR and binary mask rendering is always performed using GPU. The total GPU time for BW PD method is not available, as the method does not involve an explicit similarity measure and the CPU implementation of Levenberg-Marquardt method is used. Corresponding accuracy results are shown in Table 6.1. The average convergence graphs of the BW SSD method are shown in Figure 6.7.

	Iterations			Images			**Total time**	
Method type	st. 1	st. 2	st. 3	st. 1	st. 2	st. 3	CPU [s]	GPU [s]
Intens.--based	23.45	22.11	16.44	668.72	1079.07	1736.08	15.77	**8.76**
BW SSD	19.56	21.35	14.04	541.09	1041.39	1489.07	6.24	**3.19**
BW PD	34.89	16.13	13.79	934.42	794.99	1459.71	14.46	-

the matrices F,F_{max} and J_F have significantly larger dimensions in comparison to the intensity-based and BW SSD methods (see Section 6.3.4.2).

6.5 CONCLUSIONS

We have proposed novel methods for the multiview 2D/3D reconstruction of the femoral bone. The formulation of the registration as a non-linear least squares problem and consequent optimisation using the well-established Levenberg-Marquardt algorithm leads to significantly faster and more reliable 2D/3D reconstruction method that requires a lower number of iterations to converge. Ehlke [32] reported that, for a pelvic bone reconstruction using his gradient-descent based optimisation aproach, approximately 6000 digitally reconstructed radiographs were rendered on average during the registration and the whole reconstruction took 1:41 minutes on average. In comparison, approximately 3500 digitally reconstructed radiographs were needed to reconstruct the femoral bone using our intensity-based approach on average, which results in significant reconstruction speed-up. The intensity-based registration took 8.76 seconds on average. It should be said that this comparison is rather sketchy because of the different involved graphics hardware, number of X-ray images, size of the shape model, *et cetera*.

Due to its straightforward parallelization, the BW SSD method reaches the highest registration speed-up, as the average time of the reconstruction is less than 4

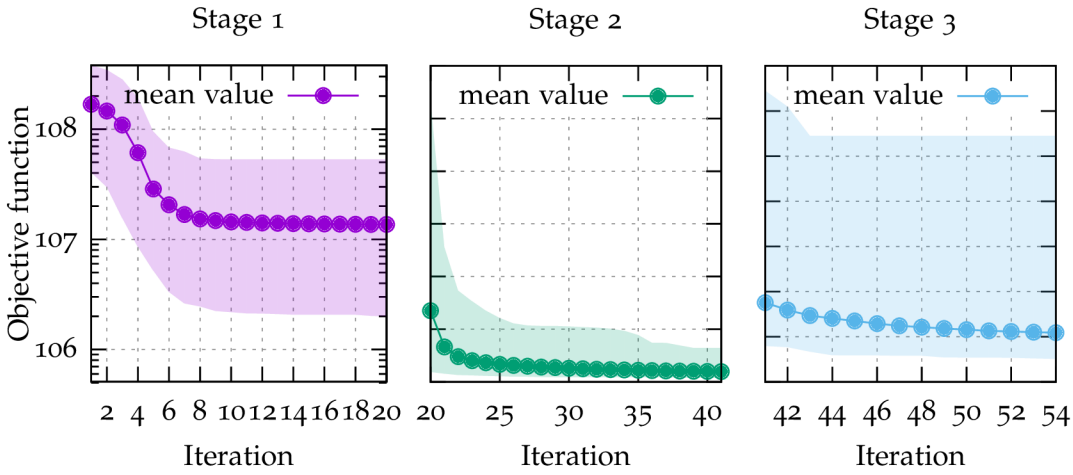

Figure 6.7: Convergence of the objective function (Equation 6.9) in particular stages of the optimisation: the rigid and reduced deformable registration stages (left), full deformable registration (right). The vertical axis are in logarithmic scale.

seconds. On the other hand, this method faces less registration accuracy caused by the global character of the SSD similarity measure which averages differences among the whole image. In the BW PD method, we overcome this drawback by the reformulation of the measure and the optimization focusing on similarities of local bone features. Here, the Levenberg-Marquardt method updates the optimised parameters with respect to derivatives of individual pixels of the X-ray and DRR binary masks instead of derivatives of the global similarity measures. This leads to very accurate registration method, the accuracy reached 1.02 ± 1.35 mm, so the BW PD method outperforms most methods that can be found in a brief summary of the state of the art methods presented by Baka [11]. Both the BW methods require precise X-ray images segmentation. Thanks to the presence of intensity information, the intensity-based method has the potential to work with original not segmented radiographs and at the same time to reach better accuracy than the BW SSD method.

Moreover, the least squares formulation of the registration allows straightforward extension to the multifragment 2D/3D reconstruction. Our future work will be focused on the simultaneous 2D/3D reconstruction and 3D reduction of a fractured femoral bone. The rendering part and the similarity measures part is distributed as open-source software and can be found at `https://github.com/klepo/ssimrenderer`.

ACKNOWLEDGEMENTS

This work has been funded by the Technology Agency of the Czech Republic grant TA04011606 Modern Image Processing Techniques and Computer-based Planning

in Trauma Treatment. We thank the University Hospital in Ostrava for providing CT and X-ray images of a phantom and bone models. We specially thank Roman Madeja and Petr Novobilsky for their effort provided during creating the data sets. We also thank Petr Krupa and Leopold Pleva for their useful advice.

6.6 APPENDIX

The *Black&White Pixel-Differences* method is also referred to as the intensity-based non-overlapping area registration. The intensity-based registration approach using digitally reconstructed radiographs capturing the bone internal structures and densities is also referred to as the density-based registration. Subsequent iterations of the density-based registration are illustrated in Figure 6.8.

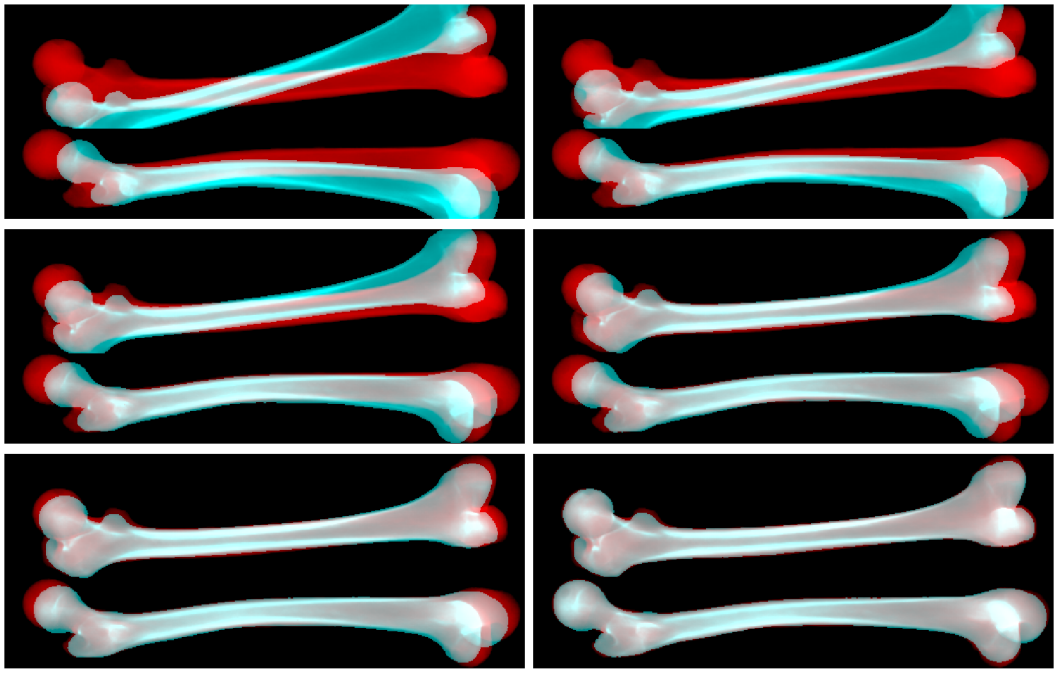

Figure 6.8: Illustration of the density-based registration. Full video of the density-based registration is available at https://youtu.be/bkGdJhEbjkA, a video of non-overlapping area registration is available at https://youtu.be/WjFwkoYojC0.

7

A STUDY ON PERFORMACE OF LEVENBERG-MARQUARDT AND CMA-ES OPTIMIZATION METHODS FOR ATLAS-BASED 2D/3D RECONSTRUCTION

CITATION

[KCZ+16] Ondřej Klíma, Adam Chromý, Pavel Zemčík, Michal Španěl, and Petr Klepárník. A study on performace of Levenberg-Marquardt and CMA-ES optimization methods for atlas-based 2D/3D reconstruction. *IFAC-PapersOnLine*, 49(25):121–126, 2016. 14th IFAC Conference on Programmable Devices and Embedded Systems PDES 2016. doi: 10.1016/j.ifacol.2016.12.021

ABSTRACT

In this study, we compare the performance of our previously proposed deformable 2D/3D registration approach based on the Levenberg-Marquardt optimization with methods exploiting Covariance Matrix Adaptation (CMA) and Covariance Matrix Self Adaptation (CMSA) evolution strategies. The aim of the registration is to reconstruct a patient-specific 3D bone model from a small set of plain 2D X-ray images what is achieved by fitting a deformable bone atlas onto the X-ray images. The comparison of different optimization methods is focused on both the robustness and the speed. The results were obtained using a large-scale data set of synthetic X-ray images. We show that our method is several times faster in comparison with the approaches based on evolution strategies while the robustness of the reconstruction is preserved. To speed-up the reconstruction process, certain parts of the registration pipeline are accelerated using graphics hardware. The median error of our proposed method was 1.12 mm and the median reconstruction time was 7.2 s. The median time reached by the CMA-ES and CMSA-ES methods was 48.5 s and 138.5 s respectively.

KEYWORDS

2D/3D reconstruction, Levenberg-Marquardt optimization, CMA-ES, CMA-ES, Statistical Shape and Intensity Model

7.1 INTRODUCTION

An identification of the best fitting bone plate for a specific patient is a one of common tasks in the field of orthopedic surgery. The plate shape identification can be performed during a preoperative planning stage. The planning process typically exploits a 3D model of the injured bone which is usually derived from a Computed Tomography (CT) scan of the patient. In recent years, the possibilities of a preoperative planning based only on plain 2D X-ray images have been brought to focus, as the plain X-ray imaging exposes patients to lower doses of ionizing radiation and it is less expensive in comparison with the CT examination. The key moment of such planning is a reconstruction of the 3D bone model from a small count of 2D X-ray images. This reconstruction is achieved by a non-rigid 2D/3D registration of a deformable 3D femoral atlas onto the images. The 2D/3D registration is solved as a numerical optimization. The accuracy of the reconstruction depends on the choice of the optimization method. The registration speed is crucial, especially for use in clinical cases, and is closely related to the convergence rate of the chosen numerical optimization approach.

In [KKŠZ15, KKŠZ16a], we have proposed a 2D/3D registration method based on the Levenberg-Marquardt algorithm which is a highly effective non-linear least squares problem solver, see [59]. In this study, we compare the performance of our previously proposed method against approaches based on Covariance Matrix Adaptation Evolution Strategy (CMA-ES), see [42], which is frequently used for the purpose of 2D/3D registration, and its Covariance Matrix Self Adaptation Evolution Strategy (CMSA-ES) variant proposed by [15]. The results reveal that our Levenberg-Marquadt based method is several times faster than the methods using the evolution strategies while reaching the same reconstruction accuracy.

7.2 RELATED WORK

Most of previously published 2D/3D registration approaches can be classified as feature-based or intensity-based methods. Feature-based registration methods rely on bone edges, or silhouettes detected in the original X-ray images. The pre-trained bone atlas is usually a deformable Statistical Shape Model (SSM) which is capable to learn bone surface variations within a population. Consequently, such feature-based methods reconstruct only a shape of a bone. In contrast, intensity-based methods proposed by [132, 97, 35, 32] work with original X-ray images and use Statistical Shape and Intensity Model (SSIM). In addition to the bone shape, appearance models capture the bone densities. Hence the anatomical structures such

as a compact and spongy bone can be reconstructed as well. In this study, we focus on the intensity-based methods.

Previous 2D/3D registration approaches use various optimization methods, i. e. modifications of the gradient-descent algorithm [32]. Strong attention is currently paid to the gradient-free CMA-ES method involved by [36, 35, 37, 61, 86, 60, 27]. The main benefit of the CMA-ES method is no requirement of the Jacobian matrix numerical approximation during the registration.

Many previously published comparisons of various atlas-based 2D/3D registration methods were only tentative. The main reason was the evaluation data sets were not shared between the authors and typically consisted only of a small number of cases. Moreover, the evaluations were performed on different hardware configurations and the experimental implementations were not equally sophisticated. The *main contribution* of this paper is a fair comparison of the mentioned methods on a reasonably large evaluation data set.

7.3 METHOD

Approaches evaluated in this study reconstruct bones from two co-registered orthogonal X-ray images. The background of the bone must be segmented out from the original X-ray images and a rough initial estimate of the appearance model pose must be provided interactively by a user. The rest of the registration pipeline is built as an iterative process. Virtual X-ray images, refered as Digitally Reconstructed Radiographs (DRRs), are rendered from the appearance model in each step of the registration using our OpenGL-based GPU implementation, proposed in [KKŠZ16a]. The dissimilarities between original and virtual X-ray images are evaluated using Normalized Mutual Information (NMI) image similarity measure, detailed in [52]. Due to performance reasons, evaluation of the NMI similarity metric is accelerated using GPU as well. The pose and the shape parameters of the appearance model are adjusted in each iteration until the dissimilarities are minimized. Finally, the bone is reconstructed as a specific instance of the 3D appearance model.

7.3.1 *Statistical Shape and Intensity Model (SSIM)*

We adopted SSIM appearance model based on volumetric meshes proposed by [132]. Tetrahedral meshes of femoral bones derived from CT scans were brought into correspondence using `Elastix` toolbox created by [64]. Registered meshes were aligned using Generalized Procrustes Analysis (GPA), while the size of models remained unchanged. A linear model describing the shape variability of

Figure 7.1: A digitally reconstructed radiograph of a femoral bone rendered from the involved SSIM model.

femoral bones was obtained after applying the Probabilistic Principal Component Analysis (PPCA):

$$S = \phi \mathbf{b} + \overline{S} + \epsilon \tag{7.1}$$

where S is a vector formed by concatenated coordinates of tetrahedral model vertices, $\overline{S}$ is a mean shape vector, ϕ is a matrix of principal components, $\mathbf{b}$ is a vector of independent shape parameters and ϵ is a zero-mean Gaussian noise. The bone density is described in each tetrahedron using Bernstein polynomials:

$$D(\mu) = \sum_{\forall i,j,k,l \in i+j+k+l=n} C_{i,j,k,l} B^n_{i,j,k,l}(\mu) \tag{7.2}$$

where μ are barycentric coordinates of a point inside the tetrahedron, $D(\mu)$ is a bone density at that point, $B^n_{i,j,k,l}$ is a Bernstein basis for n-th degree polynomial and $C_{i,j,k,l}$ is the corresponding coefficient. For more details about the SSIM models and their training we refer the reader to works published previously by [132], [KKŠZ16a].

For the rendering of DRR images from the SSIM model, the `OpenGL` accelerated approach originally proposed by [32] has been adopted. The integrals of Bernstein polynomials along the virtual rays intersecting the appearance model are evaluated using a closed form solution proposed by Sadowsky [97]. A sample virtual X-ray rendered from the SSIM model is illustrated in Figure 7.1.

7.3.2 *2D/3D Registration*

We formulate the double-view 2D/3D registration as a non-linear least squares problem:

$$x^* = \underset{x}{\operatorname{argmin}} \frac{1}{2} F(x)^T F(x) \tag{7.3}$$

where $x = (R, T, \mathbf{b})$ is a vector containing rotation, translation and shape parameters of the appearance model respectively and $F(x)$ is a column vector of residuals to be minimized defined as follows:

$$F(x) = \begin{pmatrix} NMI_1(x) - 2 \\ NMI_2(x) - 2 \end{pmatrix} \tag{7.4}$$

where $NMI_{\{1,2\}}(x)$ is a similarity between the original X-ray image and the DRR image rendered according to the parameters x, evaluated for the views 1 and 2 respectively. If the corresponding X-ray and DRR images are the same, the value of NMI similarity measure is equal to 2.

The speed of the reconstruction is determined by the total number of images rendered during the optimization, as the rendering and the similarity measure evaluation are the most time-demanding parts of the registration pipeline. The total number of images depends on the convergence of the chosen optimization method and on the amount of virtual X-rays rendered in a single iteration.

The Levenberg-Marquardt method requires evaluation of the Jacobian matrix J_F. Size of the matrix is given as $N_{views} \times N_x$, where N_{views} is the number of X-ray views and N_x is the number of optimized parameters. As a closed formula solution of the J_F does not exists, the central differences approximation of the matrix is typically used. In consequence, two images are rendered for each J_F element. Because the study is focused on the two-view reconstruction, the count of images N_{LM} rendered in each iteration is approximately given by:

$$N_{LM} \approx 4N_x \tag{7.5}$$

In our experiments, we use implementation of the Levenberg-Marquardt algorithm provided by the `dlib` library, proposed in [62].

The CMA-ES and CMSA-ES methods require to set parameters describing population size λ, parents count μ and an initial step size σ. We use the estimations $\lambda_{CMA} = \max[5, \min(N_x, 4 + 3\lfloor \log N_x \rfloor)]$, $\sigma_{CMA} = N_x^{-\frac{1}{2}}$ for the CMA-ES method and $\lambda_{CMSA} = 4N_x$, $\sigma_{CMSA} = 1$ for the CMSA-ES method. The $\mu = \lfloor \frac{\lambda}{2} \rfloor$ is same for both the methods. Consequently, the number of images rendered during a single iteration N_{CMA} and N_{CMSA} is equal to:

$$N_{CMA} \approx 2\lambda_{CMA} \tag{7.6}$$

$$N_{CMSA} \approx 8N_x \tag{7.7}$$

The reference implementations of the CMA-ES and CMSA-ES methods from the `Shark` library by [49] were adopted in this study. The optimizations are terminated when the values of the objective function in two subsequent iterations are equal. Comparison of the number of images is shown in Figure 7.2.

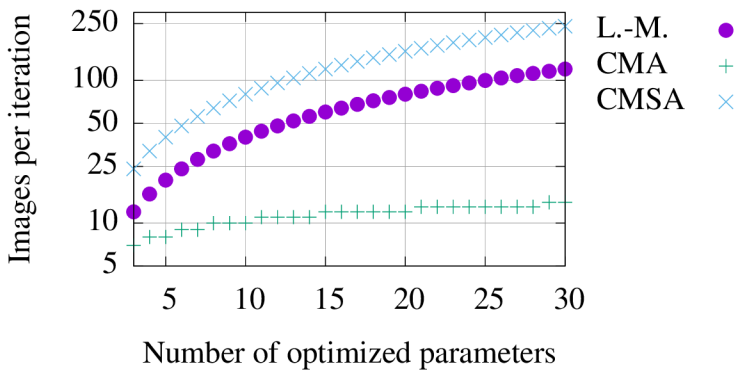

Figure 7.2: A growth of the number of images rendered in a single iteration with respect to the number of optimized parameters. The vertical axis is in a logarithmic scale.

7.3.3 *Optimization Scheme*

The whole reconstruction process comprises of 3 subsequent registrations:

1. *Rigid registration* - only the pose of the mean shaped SSIM model is being optimized.
2. *Reduced deformable registration* - the pose of the appearance model is optimized together with a subset of the first shape parameters.
3. *Full deformable registration* - all shape parameters are optimized together with the pose.

The first and the second stages are involved to prevent the registration from getting stucked in a local minima and to speed-up the process by reducing the amount of simultaneously optimized parameters. The last stage is performed to reconstruct fine details of the bone. During the registration, the bone densities are set to mean values.

7.4 EXPERIMENTAL RESULTS

The evaluation was focused on the accuracy and time consumption of the registration procedure. We involved leave-one-out and leave-all-in evaluation methodologies. During the leave-all-in evaluation, the reconstructed bone was present in the training set of the appearance model and consequently, the accuracy of the registration was not affected by the appearance model generalization ability. In contrast, during the leave-one-out methodology, the reconstructed bone was discarded from the SSIM trainig set so the results reflect the real-world usage situation.

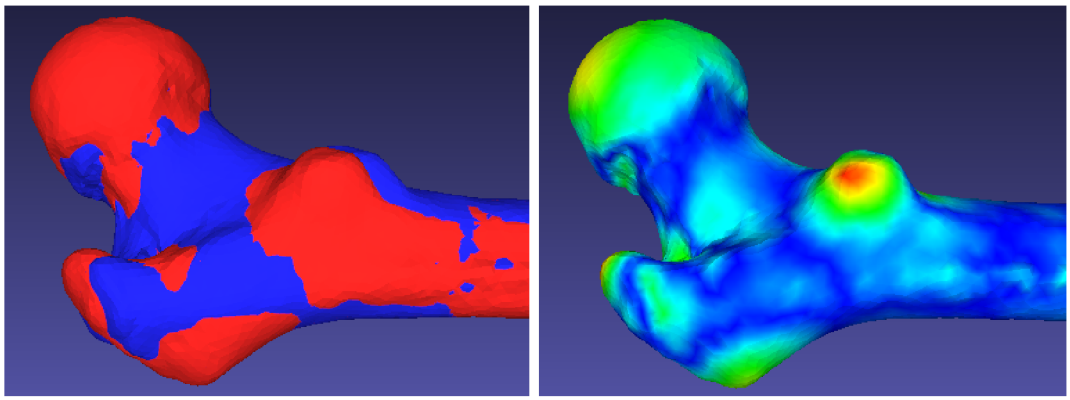

Figure 7.3: A proximal part of a femoral bone reconstructed with mean error of 1.12 mm. The reconstructed bone highlighted by a red color is aligned to the ground-truth bone model obtained from CT image (left). The reconstruction error is visualized by a heatmap, the red color shows places with the highest error of 5.68 mm (right).

7.4.1 *Evaluation Data Sets and Measurements*

We used SSIM models created from 21/22 CT images obtained from `Virtual Skeleton Database`, proposed by [63], for leave-one-out/leave-all-in evaluations respectively. The reference tetrahedral mesh contained 26,000 vertices and 104,000 tetrahedra. The density was described using Bernstein polynomials of the 2^{nd} degree, resulting in 10 density coefficients per tetrahedron. The appearance models were described using 19/20 shape parameters for leave-one-out/leave-all-in methodologies respectively.

Table 7.1: Summary of time consumption in seconds.

Method	Minimum	Q1	Median	Q3	Maximum
Leave-one-out evaluation					
Levenberg-Marquardt	**3.54**	**5.84**	**7.15**	**8.88**	**15.49**
CMA-ES	14.61	39.95	48.51	61.07	137.59
CMSA-ES	38.06	111.54	138.47	172.01	331.90
Leave-all-in evaluation					
Levenberg-Marquardt	**4.11**	**7.79**	**8.92**	**10.74**	**16.49**
CMA-ES	13.04	42.23	51.42	66.05	133.33
CMSA-ES	32.72	119.39	145.14	179.05	344.07

The methods were evaluated on a data set containing 100 orthogonal pairs of virtual X-ray images, ray-casted from CT images of 8 individuals. An average size

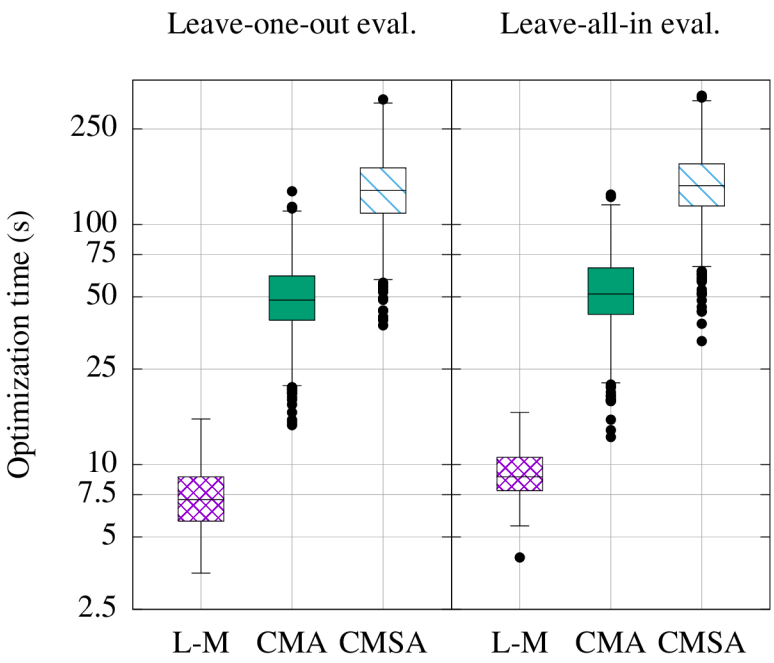

Figure 7.4: Distributions of the reconstruction time. The vertical axis is in logaritmic scale.

of X-ray images was 201 × 474 pixels. The initial poses were generated randomly with a uniform distribution. The maximum error of initial pose was limited to ±10 mm in translation and ±10 ° in rotation.

The evaluations were performed on a desktop machine equipped with `NVidia GTX980Ti 6GB` video adapter, `Intel i5-4460` processor and 24GB of RAM.

As the evolution strategies are stochastic, we repeated CMA-ES and CMSA-ES reconstructions 10 times resulting in 1000 test cases for each evolution strategy. The reconstruction accuracy was evaluated using the mean symmetric Hausdorff distance, proposed by [10], measured between the reconstructed surface and the ground-truth bone models obtained from CT images. We considered the reconstruction successful when the RMS error between the surfaces was less than 3. Except two cases for the Levenberg-Marquardt optimization and three cases for CMSA-ES leave-all-in evaluation, all reconstructions were successful. The unsuccessful cases were discarded from the following plots.

In the first stage, only 6 parameters describing the appearance model pose were optimized. In the following stage, the pose parameters were optimized together with the first 5 shape parameters of the appearance model. During the full deformable registration, 25/26 parameters were optimized in total.

The measured number of iterations is shown in Table 7.2, number of images rendered per iteration and in total are shown in Table 7.3. The average time for one image rendering and for one metric evaluation was 0.94 ms and 1.10 ms respectively. The resulting reconstruction times are shown in Figure 7.7 and Table 7.1.

Table 7.2: Average number of iterations per stage.

	Leave-one-out			*Leave-all-in*		
Method	Stage 1	Stage 2	Stage 3	Stage 1	Stage 2	Stage 3
Levenberg-Marquardt	**24**	**22**	**16**	**25**	**22**	**24**
CMA-ES	310	191	641	310	196	694
CMSA-ES	154	109	272	153	111	280

Table 7.3: Number of images rendered in each iteration and average total number of images for leave-one-out/leave-all-in evaluations.

	Images per iteration			Total images
Method	Stage 1	Stage 2	Stage 3	Stages 1 - 3
Levenberg-Marquardt	24	44	100 / 104	**1144** / **1452**
CMA-ES	**6**	**11**	**13** / **13**	8195 / 8700
CMSA-ES	48	88	200 / 208	23822 / 25107

Table 7.4: Summary of the mean Hausdorff distance distributions (values in millimeters).

Method	Minimum	Q1	Median	Q3	Maximum
Leave-one-out evaluation					
Levenberg-Marquardt	0.84	0.99	1.12	1.25	2.02
CMA-ES	0.81	0.98	1.09	1.20	1.72
CMSA-ES	0.81	0.99	1.09	1.21	1.76
Leave-all-in evaluation					
Levenberg-Marquardt	0.34	0.56	0.64	0.78	1.87
CMA-ES	0.28	0.47	0.56	0.63	1.08
CMSA-ES	0.22	0.50	0.59	0.69	1.48

The corresponding results for reconstruction accuracy are shown in Figure 7.5 and summarized in Table 7.4. The case of Levenberg-Marquardt leave-one-out reconstruction, that reached a median accuracy, is visualized in Figure 7.3.

We also investigated a correlation of the results reached by the methods. The correlation of reconstruction accuracy is illustrated in Figure 7.6, the time-

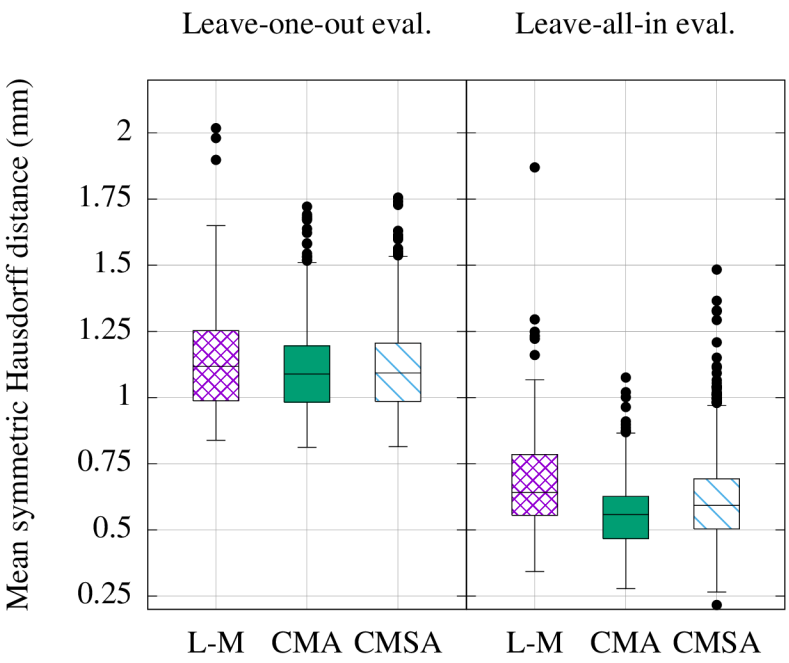

Figure 7.5: Distributions of the symmetric mean Hausdorff distance.

consumption correlation is shown in Figure 7.7. The corresponding coefficients are summarized in the Table 7.5.

7.4.2 *Discussion on results*

The results reveal that reconstruction based on the LM optimization is several times faster than CMA-ES and CMSA-ES based methods while reaching similar accuracy.

Table 7.5: Correlation coefficients for leave-one-out/leave-all-in evaluations of reconstruction accuracy and time consumption.

Methods		Hausdorff distance	Time
Levenberg-Marquardt	CMA-ES	0.5440 / 0.5002	0.3397 / 0.2764
Levenberg-Marquardt	CMSA-ES	0.5828 / 0.5762	0.3463 / 0.2834
CMA-ES	CMSA-ES	0.8321 / 0.7324	0.4207 / 0.3491

The median time of the registration using the LM method was more than 16-19 times lower in comparison to the CMSA-ES method and approximately 6-7 times lower in comparison to the CMA-ES method (see Table 7.6). Although the number of images rendered in a single iteration scales the best in case of CMA-

ES method, the rate of convergence was significantly lower in comparison with the Levenberg-Marquardt algorithm. On average, the CMA-ES based registration required approximately 6-7 times more image renderings and metric evaluations to converge and consequently the registration time was proportionally longer. We also observed that the most iterations were spent on the refinement of fine details of the reconstruction.

Table 7.6: Speed-up factors between Levenberg-Marquardt and ES-based methods.

	Time		Images	
	CMA-ES	CMSA-ES	CMA-ES	CMSA-ES
Leave-one-out	6.78	19.37	7.16	20.82
Leave-all-in	5.76	16.27	5.99	17.29

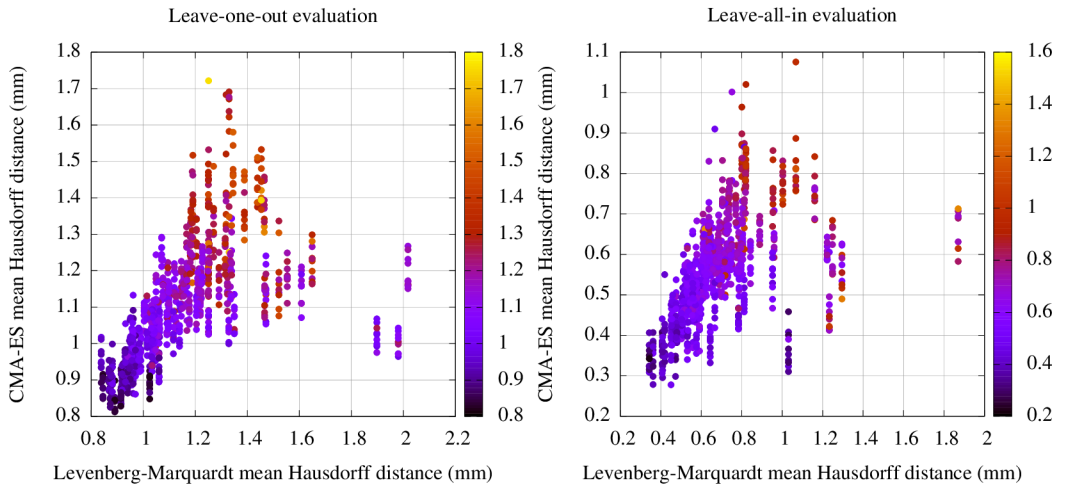

Figure 7.6: Correlation of the mean Hausdorff distance. The results of CMSA-ES are visualized using heatmap.

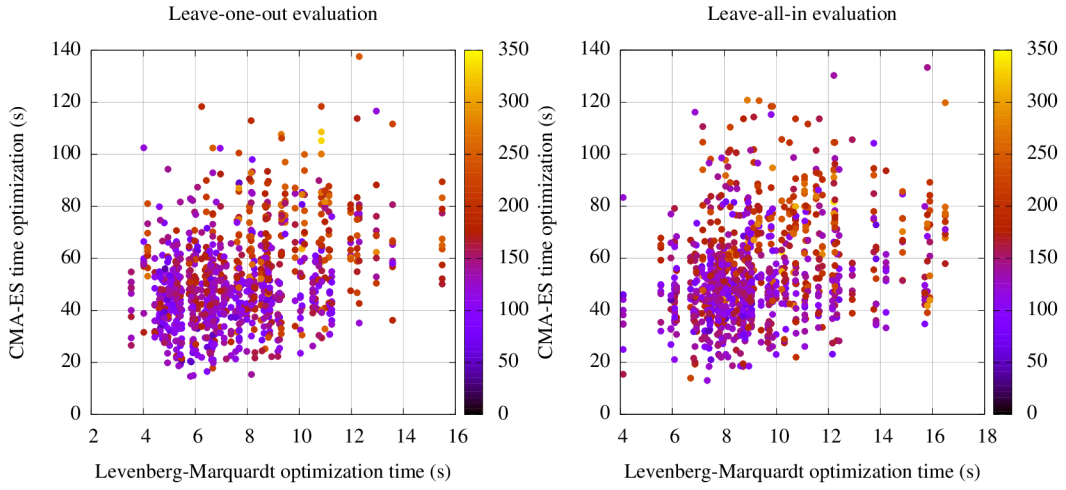

Figure 7.7: Correlation of the time consumptions. The heatmap shows CMSA-ES values.

The correlation was high in case of accuracy results and significantly lower in case of time consumption. This was caused by the stochastic nature of the evolution strategies, when the most while random amount of time was spent on a refinement of fine details, while the accuracy gain of fine details tuning was always low.

7.5 CONCLUSION

Although the CMA-ES optimization is more convenient for the usage in the 2D/3D registration, as the method does not require a non-trivial approximation of the Jacobian matrix, the Leveberg-Marquardt method provides several times faster registration and consequently is more suitable for the cases when the reconstruction time is crucial.

ACKNOWLEDGEMENTS

This work was supported by the Internal Science Fund of Brno University of Technology grant no. FEKT/FIT-J-16-3485 Application of 3D Modeling in Health-care, and by the Technology Agency of the Czech Republic grant no. TA04011606 Modern Image Processing Techniques and Computer-based Planning in Trauma Treatment.

8

LOSSY COMPRESSION OF 3D STATISTICAL SHAPE AND INTENSITY MODELS OF FEMORAL BONES USING JPEG 2000

CITATION

[KBK+16] Ondřej Klíma, David Bařina, Petr Klepárník, Pavel Zemčík, Adam Chromý, and Michal Španěl. Lossy compression of 3D statistical shape and intensity models of femoral bones using JPEG 2000. *IFAC-PapersOnLine*, 49(25):115 – 120, 2016. 14th IFAC Conference on Programmable Devices and Embedded Systems PDES 2016. doi: 10.1016/j.ifacol.2016.12.020

ABSTRACT

Recent development of computer-assisted medical systems, based on statistical shape analysis, leads to a growing number of emerging shape and appearance models. In this paper, we propose a novel method for a lossy compression of 3D statistical shape and intensity models exploiting the JPEG 2000 image coding system. We also investigate the influence of the lossy compression on the accuracy of an atlas-based 2D/3D reconstruction, which is one of the common applications of the statistical appearance models. The results revealed the method is highly effective for the intensity information, reaching thousandfold compression ratios without affecting the 2D/3D reconstruction accuracy. The bitrate of shape information can be compressed several times without significant influence on the reconstruction accuracy.

KEYWORDS

medical data processing, statistical shape and intensity model, lossy compression, JPEG 2000, 2D/3D reconstruction

8.1 INTRODUCTION

In recent years, a statistical shape and appearance modeling became an essential part for a number of medical systems for computer assisted interventions, such as surgical navigation, preoperative planning, bio-mechanical simulation and others, as summarized by [80]. The ever increasing number of produced shape and appearance models capturing variations of human anatomy gave rise to attempts for the unification of the shape models file format and construction of databases for the shape model sharing within the research community. A unifying framework `Statismo` was proposed by [72]. A platform `Virtual Skeleton Database` for the shape model sharing was created by [63].

With respect to the rising amount of emerging shape models, we propose a method for a lossy compression of statistical appearance models and investigate the influence of the induced distortion on the appearance model quality. For the compression we exploit the JPEG 2000 standard, originally designated for the natural image compression. We also investigate the usability of distorted appearance models in terms of 2D/3D reconstruction.

8.2 RELATED WORK

With respect to our previous work on 2D/3D reconstruction of femoral bones, proposed in [KKŠZ16a, KCZ+16], we focus on the compression of the statistical shape and intensity model (SSIM) proposed by [132], which has been largely adopted for the purposes of the atlas based 2D/3D non-rigid registration. The aim of the 2D/3D registration is a reconstruction of a patient-specific bone model from a small count of X-ray images. Similar approaches based on the SSIM model were proposed by [37, 35, 36, 32, 97].

JPEG 2000 is an image coding system based on the wavelet compression technique. The Discrete Wavelet Transform (DWT) is a signal-processing method suitable for decomposition of a signal into several scales. It is often used as a basis for sophisticated compression algorithms. The JPEG 2000 format has wide application, especially with professional use cases. For example, Digital Cinema Initiatives (DCI) established uniform specifications for digital cinemas in which JPEG 2000 is the only accepted compression format. Other applications include medical imaging, meteorology, image archiving (printed books, handwritten manuscripts), or aerial documentation.

This work is based on our previous works in [BKZ16a, BKZ16b], where we have proposed DWT transform engine for JPEG 2000 encoders. We have also integrated

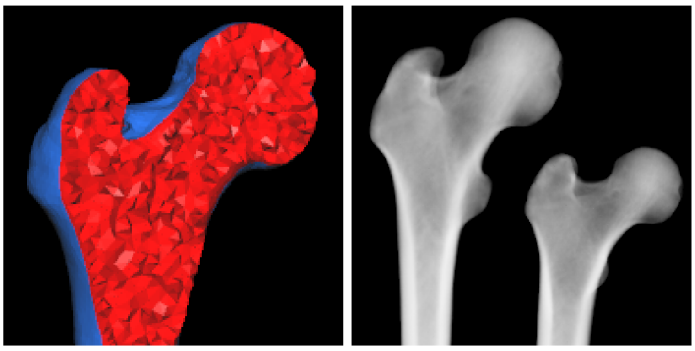

Figure 8.1: A cross-section of a proximal part of a femoral bone tetrahedral model (left) and two digitally reconstructed radiographs rendered from the statistical shape and intensity model (right).

this engine into OpenJPEG library (the reference JPEG 2000 software). In this paper, we build on these works and extends the compression chain to medical data.

8.3 APPEARANCE MODEL COMPRESSION

The statistical shape and intensity model describes a shape variations of bone anatomy within the population. It consists from a reference tetrahedral model, point distribution model (PDM), and a set of Bernstein polynomials describing the bone density. The point distribution model, proposed by [24], describes poses of the tetrahedral model vertices. It is obtained from a set of bone models using a generalized Procrustes analysis (GPA) followed by a probabilistic principal component analysis (PPCA), detailed in [16], which results into a linear model of the following form:

$$S = \psi \mathbf{b} + \overline{S} + \epsilon, \tag{8.1}$$

where $\mathbf{b}$ is a vector of orthogonal shape parameters, S is a vector containing coordinates of the tetrahedral vertices, $\overline{S}$ is a vector of mean vertices, ψ is a matrix of principal components, and ϵ is a zero-meaned Gaussian noise.

The reference tetrahedral model is illustrated in Figure 8.1. The density is described in each tetrahedron independently using Bernstein polynomials of the n-th degree:

$$D(\mu) = \sum_{i+j+k+l=n} C^{\alpha}_{i,j,k,l} B^{n}_{i,j,k,l}(\mu), \tag{8.2}$$

where μ is a barycentric coordinate inside the α-th tetrahedron, $D(\mu)$ is the bone density in the point, $C^{\alpha}_{i,j,k,l}$ are coefficients learned from a CT image, and $B_{i,j,k,l}$ is a Bernstein basis defined as:

$$B^{n}_{i,j,k,l}(\mu) = \frac{n!}{i!j!k!l!} \mu_x^i \mu_y^j \mu_z^k \mu_w^l \tag{8.3}$$

The number of coefficients N_c describing the density in a single tetrahedron depends on the degree of Bernstein polynomial and is given by:

$$N_c = \binom{n+3}{n} \tag{8.4}$$

Sample X-ray images rendered from two instances of the appearance model are shown in Figure 8.1 right.

We focus on the compression of both shape and density information of the Yao's appearance model. The tetrahedral net of the model is not suitable for the lossy compression due to the discrete nature of the data and thus is beyond the scope of this paper.

8.3.1 *Density Coefficients Compression*

Data describing density in the whole tetrahedral model have a form of $N_t \times N_c$ matrix, where N_t is a count of tetrahedra:

$$M_D = \begin{pmatrix} C^1_{i_1,j_1,k_1,l_1} & C^1_{i_2,j_2,k_2,l_2} & \cdots & C^1_{i_{N_c},j_{N_c},k_{N_c},l_{N_c}} \\ C^2_{i_1,j_1,k_1,l_1} & C^2_{i_2,j_2,k_2,l_2} & \cdots & C^2_{i_{N_c},j_{N_c},k_{N_c},l_{N_c}} \\ \vdots & \vdots & \ddots & \vdots \\ C^{N_t}_{i_1,j_1,k_1,l_1} & C^{N_t}_{i_2,j_2,k_2,l_2} & \cdots & C^{N_t}_{i_{N_c},j_{N_c},k_{N_c},l_{N_c}} \end{pmatrix} \tag{8.5}$$

Elements of the M_D matrix have a single float precision. Columns of the matrix are compressed separately. Using a linear passage, each column is reshaped into a square 2D matrix with some padding. In the next step, data are rescaled to 16 bit unsigned integers. As illustrated in the left bottom picture in Figure 8.2, these square matrices have a form of noise when treated as images. The important step before the compression is a reduction of the noise by rearranging the elements in the images, as the quality of JPEG 2000 compression is affected by the amount of present noise.

The key observation enabling the effective rearrangement is that the order of rows in M_D matrix can be arbitrarily changed on assumption that the order of tetrahedra in the tetrahedral model is changed the same way, with no influence on the appearance model quality. Consequently, no additional information describing the original tetrahedral order has to be stored with the compressed model. The second important observation reveals there is a significant correlation between the columns of the M_D matrix. Therefore, we propose to sort the M_D rows with respect to the summation of their elements:

$$f(T^\alpha) = \sum_{i+j+k+l=n} C^\alpha_{i,j,k,l} \tag{8.6}$$

$$T^\alpha \leq T^\beta \quad \Leftrightarrow \quad f(T^\alpha) \leq f(T^\beta) \tag{8.7}$$

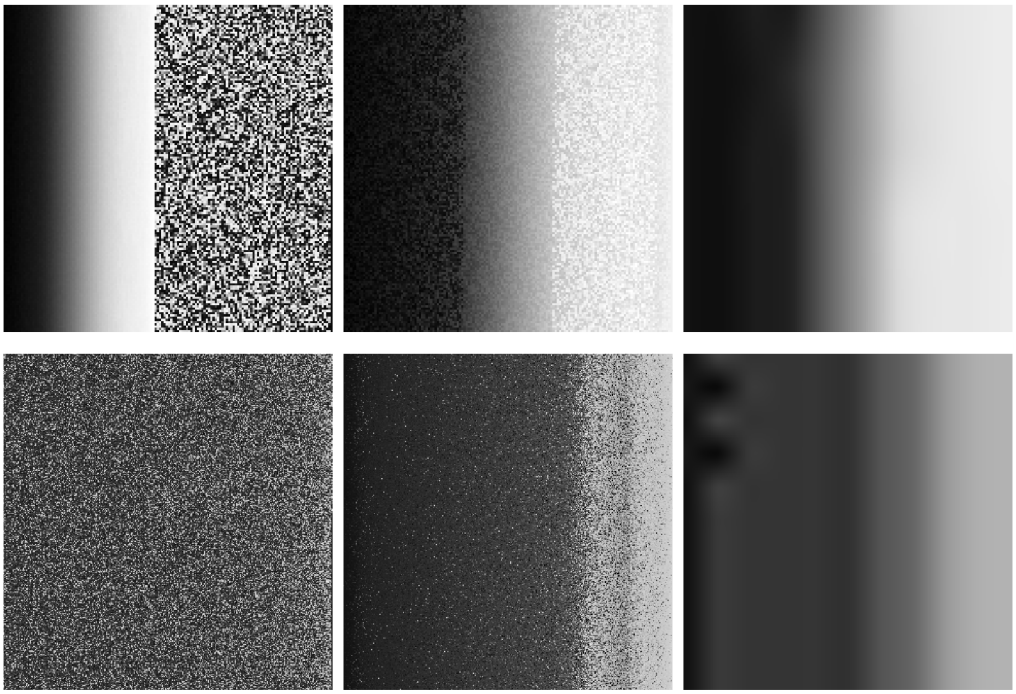

Figure 8.2: Rearrangement of the z coordinates (top row) and C_{i_1,j_1,k_1,l_1} density coefficients (bottom row) into 2D images. Each image contain data from a single column of the mean shape matrix z or the density matrix M_D respectively. The unsorted images are shown in the left, rearranged image is in the middle. The distortion induced by the the lossy compression is illustrated in the right column.

where T^{α}, T^{β} are α-th, β-th rows respectively. The final step is the compression of the sorted images using the `OpenJPEG` library. The sorting-based reduction of noise and the distortion induced by the lossy compression are shown in the middle and right pictures in Figure 8.2.

8.3.2 *Point Distribution Model Compression*

A similar pipeline as described in Section 8.3.1 is used for the compression of the mean shape vector $\overline{S}$, as there is a significant correlation between the x, y, z coordinates in case of long bones. The rows of matrix ψ must be sorted correspondingly to rearrangement of vector $\overline{S}$. The effect of rearrangement on the z coordinate is illustrated in the top row in Figure 8.2.

However, there is no correlation between the columns of matrix ψ. The matrix ψ is only reshaped to a square size and values are rescaled to 16 bit unsigned integers.

8.4 RESULTS AND DISCUSSION

For the evaluation of the compression chain we created a shape and intensity model of femoral bone from a data set of 22 CT images. The shape was described using 20 principal components, the size of matrix ψ was 65031×20 elements. The model contained 104473 tetrahedra and 21677 vertices. We also created mean density matrices M_D for Bernstein polynomials of the degrees $n \in \{0, 1, 2, 3\}$.

8.4.1 *Density Compression Accuracy*

We measured the distortion of the bone density with respect to the reached bitrate, which also depends on the degree of the Bernstein polynomial. For a ground-truth density we used the 3^{rd} degree Bernstein polynomials representation with bitrate 640 bits per tetrahedron (bpt). To evaluate the distortion, we computed the density in each vertex of the model for various bitrates and polynomial degrees n. The distorted density was compared with the ground-truth values using the root mean squared error (RMSE), measured in Hounsfield Units (HU). The results are shown in Figure 8.3. Tables 8.1 and 8.2 show the distortion values in significant points for the individual polynomial degrees.

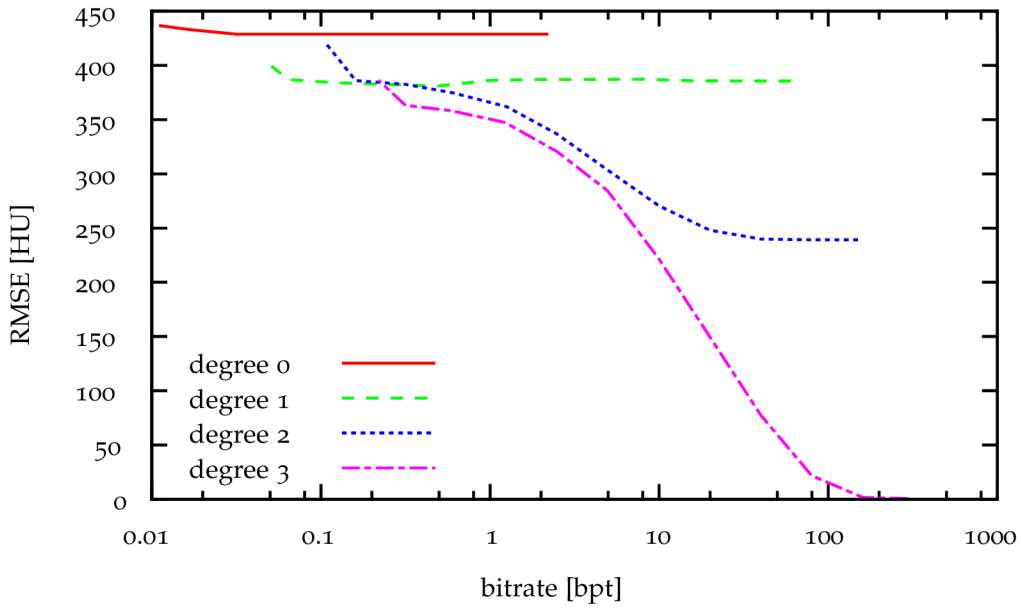

Figure 8.3: Dependency of the density distortion on the bitrate.

The results reveal that the bitrate of the density data can be several times lowered while inducing only a small distortion. When a larger distortion is acceptable, highly effective compression can be achieved, as summarized in Table 8.3.

Table 8.1: Significant bitrate points of density compression.

degree	maximal [bpt]	mean [bpt]	optimal [bpt]
0	2.166	0.500	0.011
1	59.028	1.992	0.045
2	146.907	4.988	0.109
3	289.703	9.937	0.222

Table 8.2: Density distortion in the significant bitrate points.

degree	maximal [HU]	mean [HU]	optimal [HU]
0	428.737	428.736	436.557
1	385.644	386.915	405.760
2	239.132	303.178	418.921
3	0.703	221.820	385.415

Table 8.3: The bone density compression ratios.

degree	min. ratio	max. ratio
0	14.773	2909.091
1	2.168	2844.444
2	2.178	2935.780
3	2.209	2882.883

8.4.2 *Digitally Reconstructed Radiographs Distortion*

As the rendering of virtual X-ray images is an essential task related to the SSIM model within the scope of 2D/3D reconstruction, we investigate the influence of the density distortion on the quality of the rendered radiographs. The digitally reconstructed radiographs are rendered from the Yao's appearance model using the approaches proposed by [97] and [32], exploiting the `OpenGL` acceleration. We sampled the appearance model randomly with normal distribution. For each sample, we rendered a virtual radiographs using density representations of various bitrates and polynomial degrees. We evaluated the similarity between the radiographs and corresponding reference X-ray images rendered using the ground-truth density representation. The similarity was evaluated involving the joint histogram based

normalized mutual information (NMI) measure. The NMI metric, detailed in [52], is largely adopted for tasks of medical image registration. A value of the NMI metric for two identical images is equal to 2, the minimal value the metric is equal to 1. The results for the 64×64 bins large joint histogram are illustrated in Figure 8.4 and Table 8.4.

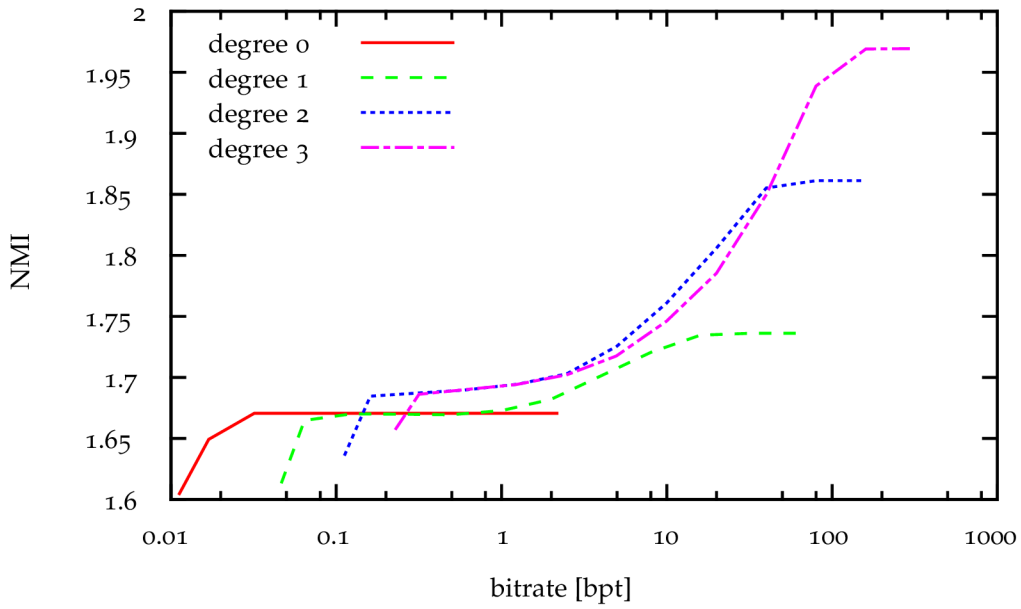

Figure 8.4: Dissimilarities between the reference and distorted radiographs measured using the NMI metric.

Table 8.4: Dissimilarities in the significant bitrate points evaluated using the NMI measure.

degree	maximal [–]	mean [–]	optimal [–]
0	1.6706	1.671	1.6493
1	1.7361	1.682	1.6728
2	1.8612	1.725	1.6846
3	1.9694	1.746	1.6861

As might be expected, the dissimilarities are proportional to the results presented in Section 8.4.1. Artifacts induced into the radiographs due to the density distortion are shown in Figure 8.5. Even with the lowest bitrate reached by the `OpenJPEG` library, the anatomical structures as spongy and compact bone are still clearly distinguishable in the rendered X-ray images. This is the contribution of the tetrahedral model rearrangement. Without the rearrangement, the radiographs rendered from models with lower bitrate would have a form of thickness images, illustrated in [68], as the 2D arrays depicted in Figure 8.2 would be distorted to images of a uniform color.

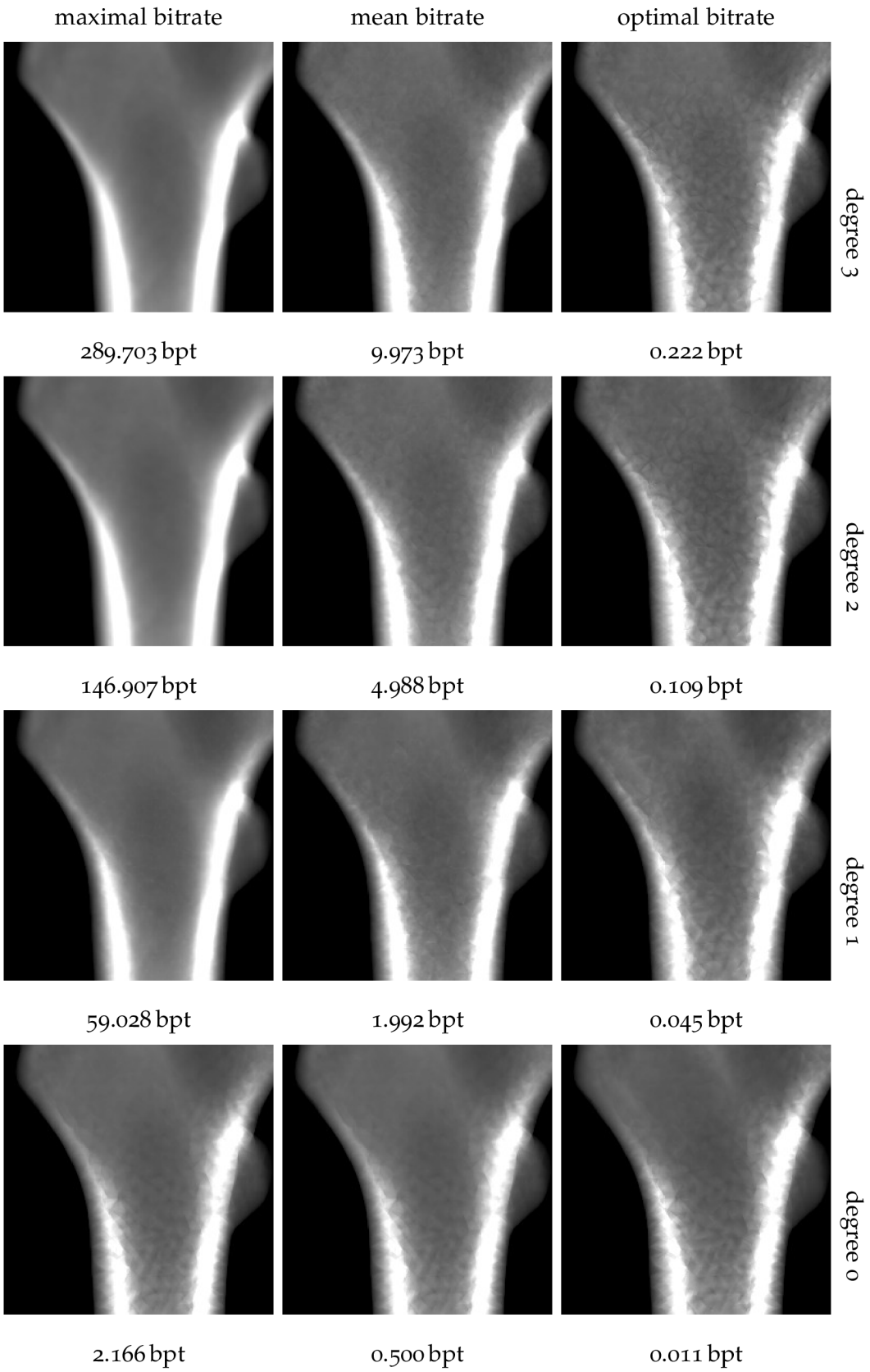

Figure 8.5: Density artifacts for various polynomial degrees and bitrates showed on the detail of a lesser trochanter.

8.4.3 *Mean Shape Compression*

We involved the distortion of the mean bone shape $\overline{S}$ using the symmetric Hausdorff distance, proposed by [10]. The distance was measured between the ground-truth mean shape and the mean shape compressed with various bitrates. The bitrate of the ground-truth bone was 96 bits per vertex (bpv). Reached Hausdorff distances are shown in Figure 8.6. Dissimilarities between the X-ray images rendered using the reference and distorted mean shapes are evaluated in Table 8.5. Only bitrates with Hausdorff distance RMS lesser than 1 mm are taken into ac-

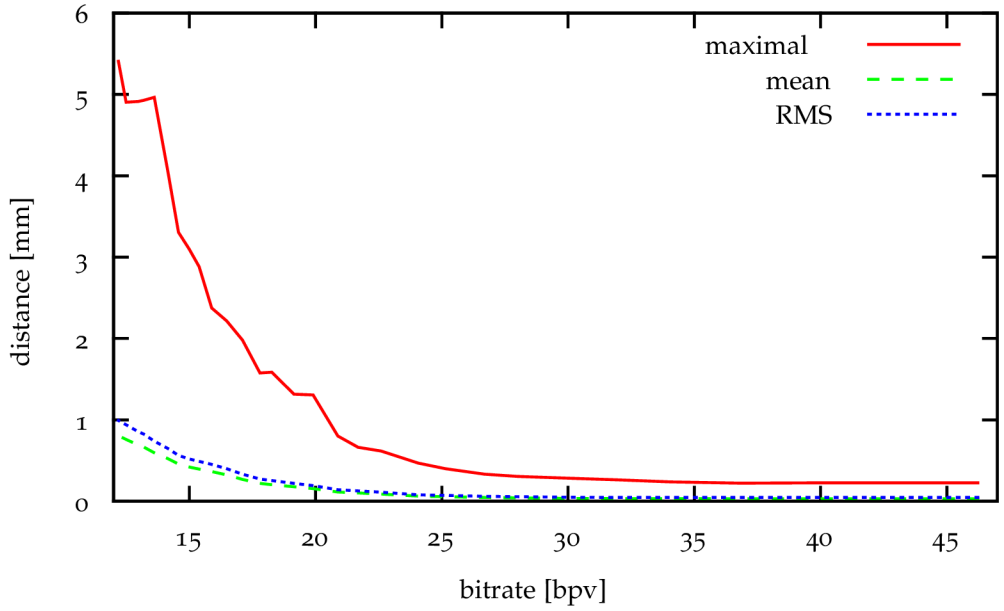

Figure 8.6: Dependency of the mean and maximal symmetric Hausdorff distance between the ground-truth mean shape $\overline{S}$ and the distorted mean shapes.

count. Artifacts induced into the mean bone shape and rendered X-ray images are illustrated in Figure 8.7.

Table 8.5: The mean bone compression bitrates with corresponding shape distortion errors.

bitrate [bpv]	NMI [–]	mean error [mm]	RMS [mm]	max. error [mm]
46.22	1.79	0.03	0.05	0.23
19.15	1.60	0.18	0.21	1.32
12.19	1.31	0.81	0.99	5.41

The results reveal that while the global shape of the mean bone is preserved even for lower bitrates, the smoothness of the model surface is rapidly distorted with the increasing compression ratio.

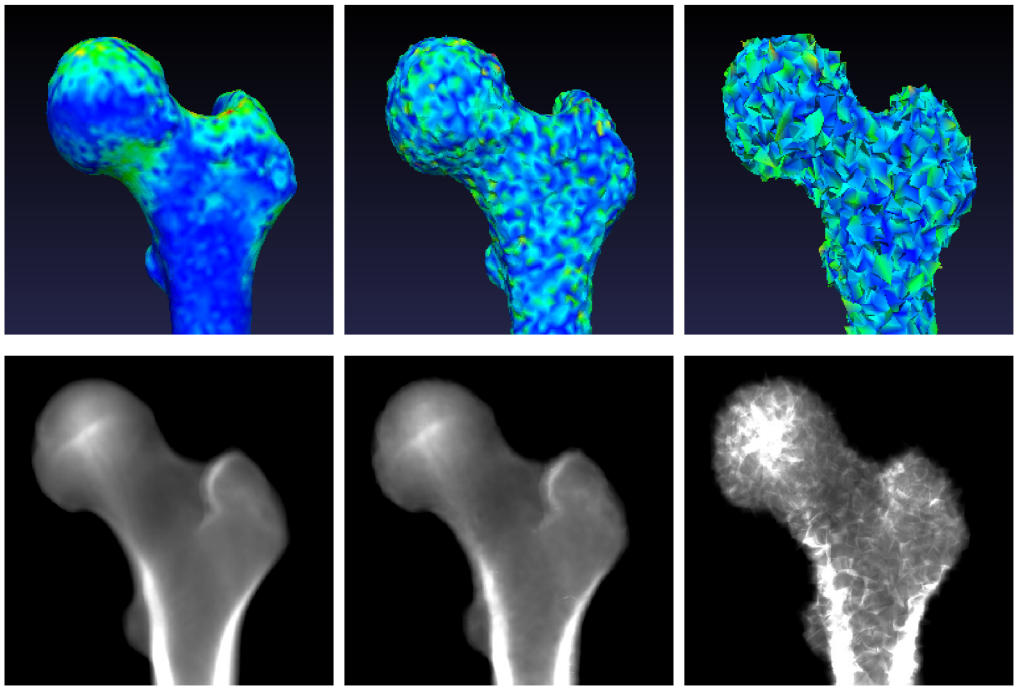

46.22 bpv 19.15 bpv 12.19 bpv

Figure 8.7: Shape artifacts affecting the bone surface smoothness (top row) and density artifacts caused by the shape distortion (bottom row). The heatmap visualizes differences from the ground-truth mean shape. The blue color marks no distortion, the red color show places with the highest error, corresponding distance values are in Table 8.5.

8.4.4 *2D/3D Reconstruction Accuracy*

We used the intensity-based 2D/3D reconstruction method proposed in [KKŠZ16a] to evaluate the influence of the compression artifacts on the 2D/3D reconstruction accuracy.

To investigate the influence of the distorted mean bone shape $\overline{S}$, we performed a set of hundred 2D/3D reconstructions for each tested bitrate. The accuracy of the reconstruction was evaluated using the mean symmetric Hausdorff distance between reconstructed and ground-truth bone models. During the registration, we used the ground-truth principal component matrix ψ and density matrix M_D, only the mean bone shape vector $\overline{S}$ was distorted by the compression. For the evaluation, we used a leave-all-in methodology, as the model of the reconstructed bone was always present in the training set of the involved SSIM model. The results are plotted in Figure 8.8 and Table 8.6.

We used a similar approach to evaluate the influence of the principal components matrix ψ compression. The results are shown in Figure 8.9 and Table 8.7. The bitrate of the ground-truth ψ matrix was 2080992 bits per component (bpc).

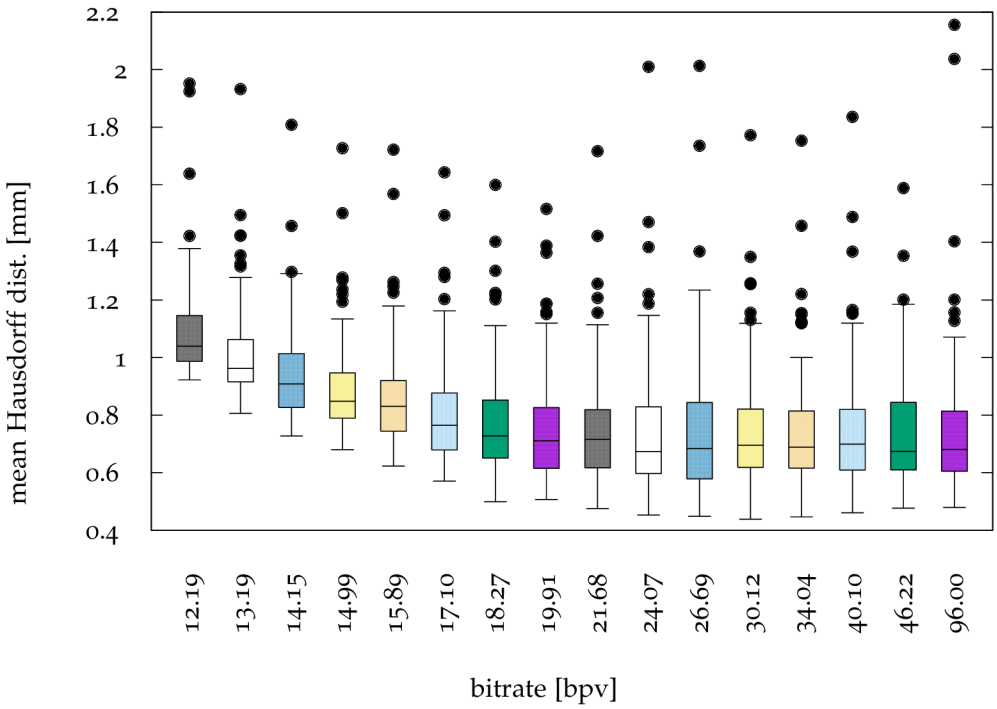

Figure 8.8: Dependency of the 2D/3D reconstruction accuracy on the bitrate of the compressed mean shape vector $\overline{S}$. The boxes show distribution of the mean symmetric Hausdorff error.

Table 8.6: The mean bone compression bitrates with corresponding shape distortion errors.

bitrate [bpv]	compression ratio	mean error [mm]	RMS [mm]	max. error [mm]
46.22	2.07	0.74	0.96	3.98
19.15	5.01	0.77	0.99	4.41
12.19	7.87	1.09	1.36	6.70

Table 8.7: Bitrates of the compresses matrix ψ and corresponding average 2D/3D reconstruction accuracy.

bitrate [bpc]	compression ratio	avg. mean error [mm]	avg. RMS [mm]	avg. max. error [mm]
1001980	2.07	0.71	0.91	3.76
230320	9.04	0.86	1.08	4.75
127860	16.28	1.84	2.27	10.55

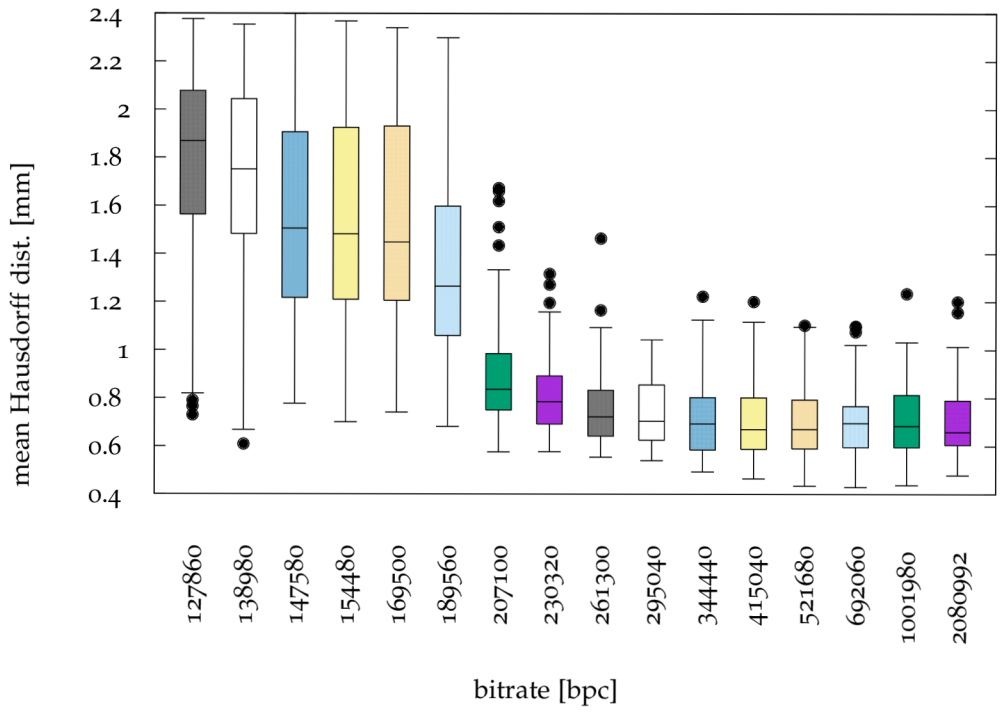

Figure 8.9: Accuracy of the 2D/3D reconstruction with respect to the bitrate of the compressed principal components matrix ψ.

The comparison in Figure 8.10 shows that the lossy compression of principal component matrix ψ is more efficient than the compression of the mean shape vector $\overline{S}$, as the reconstruction error rises faster with the compression ratio for the mean shape.

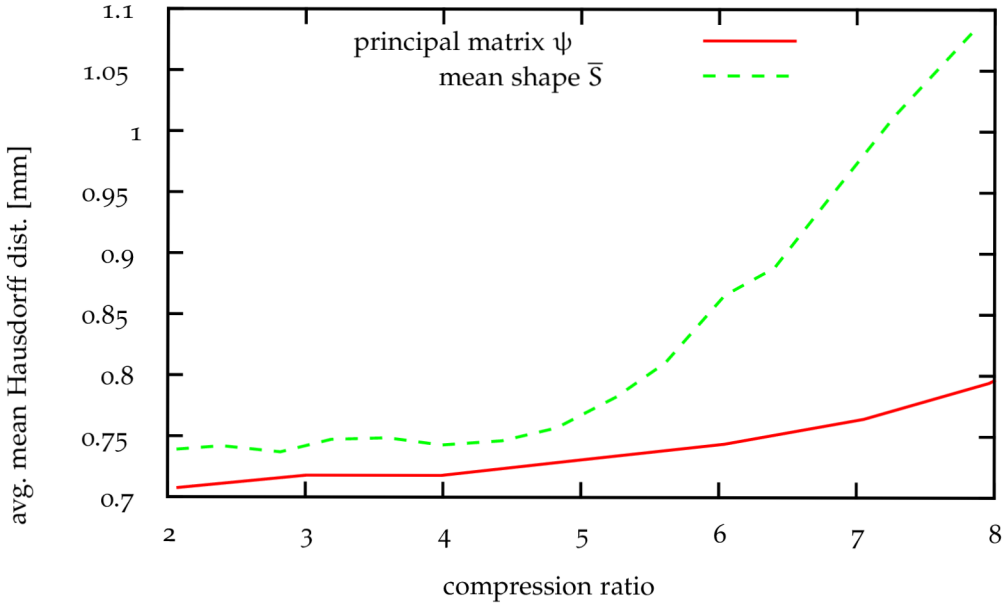

Figure 8.10: Dependency of the 2D/3D reconstruction accuracy on the ψ, $\overline{S}$ compression ratios.

We also investigated the influence of the density matrix M_D distortion on the reconstruction accuracy. Surprisingly, the accuracy was not affected by the induced artifacts for the evaluated bitrates, shown in Figure 8.3.

The results show that it is possible to compress the matrices ψ, M_D and the mean shape vector $\overline{S}$ with negligible influence on the 2D/3D reconstruction accuracy.

8.5 CONCLUSIONS

We have proposed a method for the lossy compression of the statistical shape and intensity model. The method is suitable for both density and shape compression. The results show the density compression can be highly effective while preserving an acceptable quality of virtual X-ray images for the involvement in 2D/3D reconstruction. The distorted models with lower bitrate can be conveniently shared as a shape model thumbnails for trial purposes.

ACKNOWLEDGEMENT

This work was supported by the Internal Science Fund of Brno University of Technology grant no. FEKT/FIT-J-16-3485 Application of 3D Modeling in Health-care, by the Ministry of Education, Youth and Sports from the National Programme of Sustainability (NPU II) project IT4Innovations excellence in science (no. LQ1602), and by the Technology Agency of the Czech Republic grant no. TA04011606 Modern Image Processing Techniques and Computer-based Planning in Trauma Treatment.

9

VIRTUAL 2D-3D FRACTURE REDUCTION WITH BONE LENGTH RECOVERY USING STATISTICAL SHAPE MODELS

CITATION

[KMŠ+18] Ondřej Klíma, Roman Madeja, Michal Španel, Martin Čuta, Pavel Zemčík, Pavel Stoklásek, and Aleš Mizera. Virtual 2D-3D fracture reduction with bone length recovery using statistical shape models. In *Shape in Medical Imaging*, pages 207–219, Cham, 2018. Springer International Publishing. doi: 10.1007/978-3-030-04747-4_20

ABSTRACT

Computer-assisted 3D preoperative planning based on 2D stereo radiographs has been brought into focus recently in the field of orthopedic surgery. To enable planning, it is crucial to reconstruct a patient-specific 3D bone model from X-ray images. However, most of the existing studies deal only with uninjured bones, which limits their possible applications for planning. In this paper, we propose a method for the reconstruction of long bones with diaphyseal fractures from 2D radiographs of the individual fracture segments to 3D polygonal models of the intact bones. In comparison with previous studies, the main contribution is the ability to recover an accurate length of the target bone. The reconstruction is based on non-rigid 2D-3D registration of a single statistical shape model onto the radiographs of individual fragments, performed simultaneously with the virtual fracture reduction. The method was tested on a syntethic data set containing 96 virtual fractures and on real radiographs of dry cadaveric bones suffering peri-mortem injuries. The accuracy was evaluated using the Hausdorff distance between the reconstructed and ground-truth bone models. On the synthetic data set, the average surface error reached 1.48 ± 1.16 mm. The method was built into preoperative planning software designated for the selection of the best-fitting fixation material.

KEYWORDS

Preoperative planning, Fracture reduction, Fixation devices, 2D-3D registration, Statistical shape model

9.1 INTRODUCTION

Plain radiography plays a key role in bone fracture diagnosis and treatment. In the case of surgical intervention, plain radiographs enable basic preoperative planning, such as bone fracture classification and the determination of an appropriate fixation technique for its stabilization. More advanced, computer-assisted planning of the osteosynthesis provides a virtual simulation of the intervention, which typically includes situating the fracture segments into anatomically correct and mechanically stable poses, measuring the bone morphology, or placing fixation devices [53]. The virtual simulations rely on 3D polygonal models of individual bone fragments, which are conventionally obtained from volumetric images provided by computed tomography (CT). However, during the CT examinations, the patients are exposed to substantially higher doses of radiation in comparison with plain radiography. Therefore, the indication of CT examinations is generally restricted only to cases of severe or complex fractures, while the treatment of rather common cases depends on plain radiographs. Nevertheless, computer-assisted planning can be still beneficial even for rather routine fractures, especially for long bone fractures of the lower limbs. One important contribution is the possibility of preoperative measurement of patient-specific bone morphology with aim of determining the features of the best-fitting fixation devices, such as the length of the intramedullary nail [50], the size of the bone plate, or the number and placement of bone screws. Therefore, a reconstruction of a 3D patient-specific anatomy based only on plain, clinically available radiographs instead of volumetric images is of great importance for the application of virtual planning in a broader spectrum of bone fracture treatment procedures.

In this paper, we propose a semi-automatic 3D virtual fracture reduction method, which is able to reconstruct a polygonal model of an intact bone from stereo radiographic images of the individual fracture segments. The method is focused on displaced diaphyseal fractures of the simple or wedge type.

9.2 RELATED WORK

In the field of orthopedic surgery, a somewhat similar challenge of computer-assisted 3D preoperative planning based only on plain radiographs was recently addressed by several projects [2, 1] focusing on total hip arthroplasty (THA), total knee arthroplasty (TKA), and lower extremity osteotomy. Other studies were focused on observing 3D joint kinematics from fluoroscopy sequences without the requirement of CT image acquisition [12, 111, 122]. Instead of CT scans, a non-rigid registration of 3D bone atlases onto the stereo radiographs was exploited to recon-

struct polygonal models of the bones. As proposed in works such as [76], statistical shape models were involved as the atlases to perform a shape-constrained 2D-3D registration. With respect to the statistical shape models, this reconstruction approach is straightforward when the target bone is not suffering any injuries, which is fulfilled for the total joint arthroplasty or observation of joint kinematics. However, arbitrarily shaped fracture segments make reconstruction based on statistical shape models a challenging task.

The first attempt to reconstruct injured bones using statistical atlases was proposed in a study focused on the reduction of multi-fragment fractures of the distal radius [35]. The goal of the study was to obtain a polygonal model of an intact bone from plain radiographs of the fracture segments. The reconstruction, together with the fracture reduction, were achieved at the same time by a 2D-3D registration of a single statistical appearance model of an intact distal radius into individual fracture segments. Splitting the statistical appearance model into fracture segments was performed automatically by the registration. The method was evaluated *in silico* using simulated fractures, concluding that the atlas-based reconstruction may provide a more accurate distal radius template than the conventionally used mirrored model obtained from the contralateral limb.

A later study, using a similar principle of a multi-fragment 2D-3D registration of a statistical shape model, focused on diaphyseal fractures of the long bones of the lower limbs [101]. In contrast with the previous work, its aim was to determine the rotation alignment between the proximal and distal fragments along the longitudinal axis. In addition to the rotation angles, the study considered the reconstruction of surface models of the individual fracture segments. However, the approach was unable to perform virtual fracture reduction and to provide a model of the intact bone, as the method was unable to determine the correct length of the target bone. Moreover, the shape model had to be divided into fragments in advance, without further refinement during the registration process. The bone length also had to be provided manually in a study focused on automatic fracture reduction using statistical atlases, working with mesh models of fracture segments obtained from CT scans [6].

In this paper, we address the challenge of accurate bone length recovery. Unlike [101], the division of the statistical shape model into segments is performed automatically by the registration, enabling optimization of the shape model length. In consequence, the proposed method is able to perform virtual fracture reduction and provide a 3D model of the intact bone.

Table 9.1: Characteristics of involved statistical shape models.

Statistical shape model	Size of training set	Modes of variation	Tetrahedral vertices	Tetrahedra
Femur	43 bones	41	20,843	93,480
Tibia	42 bones	40	22,003	106,436

9.3 METHOD

The method is based on a multi-fragment registration of a statistical shape model into stereo radiographs of individual fracture segments, extended by simultaneous optimization of the shape model length.

9.3.1 *Statistical Shape Models*

The statistical shape models involved in this study work as elastic tetrahedral models of bones. As their elasticity is shape-constrained, it is ensured the models always represent anatomically reasonable bones. The shape models involved were created using a procedure detailed in [KKŠZ16a]. As the models are based on probabilistic principal component analysis (PPCA), they are represented by the following generative model:

$$S = \phi \mathbf{b} + \overline{S} + \omega \tag{9.1}$$

where S is a vector containing tetrahedral vertices of the model, the shape of which is determined by independent modes of variation $\mathbf{b}$; $\overline{S}$ is a tetrahedral model of the mean bone; ϕ is a matrix of the principal components; and ω describes zero-meaned Gaussian noise.

Two statistical shape models, representing the femur and tibia, were created using CT images of intact bones, provided by the University Hospital in Ostrava. The characteristics of the models are shown in Table 9.1. Both tetrahedral models include a polygonal surface, formed by $19,996$ faces and by a subset counting $10,000$ tetrahedral vertices.

As previously described in [6], the length of the femoral or tibial shaft is relatively independent of the shape of the joint regions. Considering the statistical shape models of the involved bones, the length of the shaft is controlled mainly by the first mode b_1, while features such as the size or shape of the joint regions are modeled in particular by the rest of the modes $b_2 \dots b_n$ (Fig. 9.1). Therefore, it is impossible to determine the length of a bone based only on the shape of its distal and proximal parts.

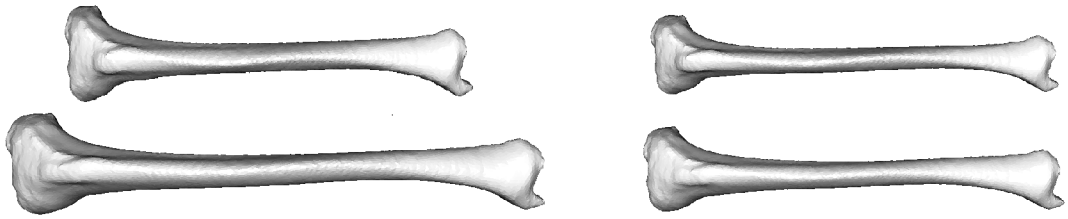

$b_1 = \pm 2\sigma$ $b_2 = \pm 2\sigma$

Figure 9.1: Statistical shape model of the tibia. The instances were generated by setting the first *(left)* and the second *(right)* parameter to $\pm 2\sigma$. The rest of the modes were set to zero.

9.3.2 *Reconstruction*

The reconstruction outcome comprises a model of a patient-specific intact bone, described by shape modes $\mathbf{b}$, and poses p_{prox}, p_{dist} of both fracture segments, forming a vector $\mathcal{P} = (\mathbf{b}, p_{prox}, p_{dist})$. The results are obtained by minimization of the reprojection error, evaluated using a non overlapping area (NOA) measure, together with a length criterion (LC):

$$(\mathcal{P}^*) = \underset{\mathcal{P}}{\operatorname{argmin}} \Big[\mathrm{NOA}(\mathcal{P}) + \mathrm{LC}(\mathcal{P}) \Big] \tag{9.2}$$

Both terms are evaluated using the input radiographs, though with different regions of interest (Fig. 9.2).

9.3.2.1 *Nonoverlapping Area*

The measure is evaluated between binary segmentations of the input digital radiographs (DR) and digitally reconstructed radiographs (DRR)[KKŠZ16a] with a reprojected statistical shape model, using only the intact regions of the bones. The nonoverlapping area is defined as the area that the segmentations do not have in common (Fig. 9.3). As shown in [KNM+18], it can be evaluated as a sum of the squared pixel differences (PD) between the input and virtual segmentations:

$$d(\mathcal{P}, x, y) = \mathrm{DR}(x, y) - \mathrm{DRR}(\mathcal{P}, x, y) \tag{9.3}$$

$$\mathrm{PD}(\mathcal{P}) = \big(d(x_1 \dots x_n, y_1 \dots y_m)\big) \tag{9.4}$$

$$\mathrm{NOA}(\mathcal{P}) = \|\mathrm{PD}(\mathcal{P})\|^2 \tag{9.5}$$

Instead of a count of different pixels, it is convenient to express the size of the nonoverlapping area relatively as $\frac{\mathrm{NOA}(\mathcal{P})}{\mathrm{NOA}(\mathcal{P})+\mathrm{OA}(\mathcal{P})}$, where $\mathrm{OA}(\mathcal{P})$ is the size of the overlapping area. The measure is an intensity-based similarity metric in the sense that the evaluation is perfomed directly with the input and reprojected pixels, leading to correspondence-free registration [KNM+18]. In contrast, the feature-based

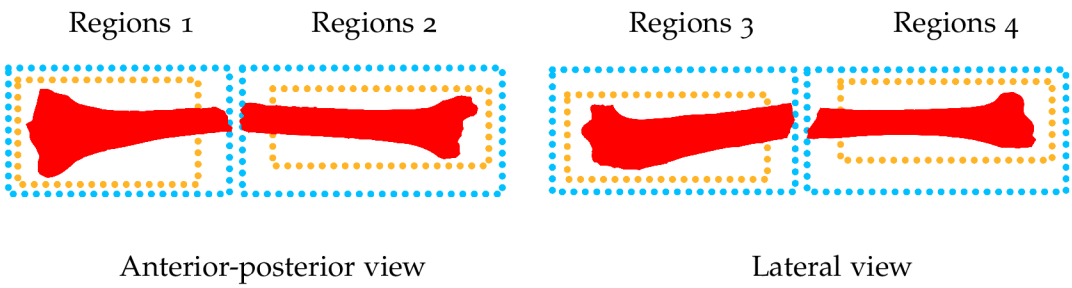

Figure 9.2: The input radiographs are divided into different regions of interest. The regions related to nonoverlapping area evaluation *(orange)* border the maximal intact parts of the bones. The boundaries of regions for length estimation *(blue)* are determined with respect to the detachement point of the bone fragments. The regions are estimated as scaled-up bounding boxes of the fragment segmentations, except the sides nearest to the fracture, which are set interactively by the user.

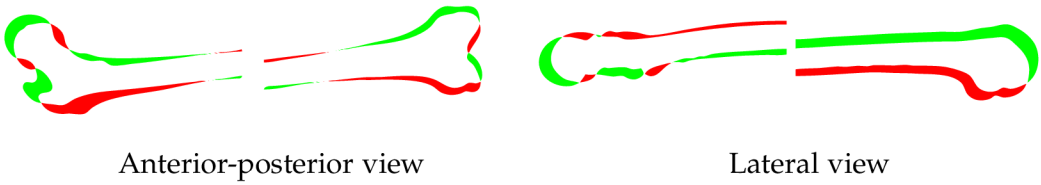

Figure 9.3: Nonoverlapping area between the input *(red)* and virtual *(green)* segmentations. The size of the depicted nonoverlapping area is 28.5%.

methods [11, 12] usually require establishing correspondences between the shape model vertices and the contours detected in the radiographs, which is a challenging and error-prone task.

9.3.2.2 *Bone Length Recovery*

As the method works with simple or wedge fractures, the injured bone is split into two main fragments. Each fragment is captured in two regions of interest forming a stereo pair, as shown in Fig. 9.2. The key idea of the recovery is to assign each vertex of the shape model to only one of the main fragments. In consequence, each vertex should be reprojected in precisely two regions, which is achieved by minimizing the length criterion:

$$\mathrm{RV}(\mathcal{P}) = \big(\mathrm{r}(\mathcal{P}, v_1 \dots v_n) - 2\big) \tag{9.6}$$

$$\mathrm{LC}(\mathcal{P}) = \|\mathrm{RV}(\mathcal{P})\|^2 \tag{9.7}$$

where $\mathrm{r}(\mathcal{P}, v)$ is the number of reprojections of the current vertex v. The relation between misassigned vertices and bone length is shown in Fig. 9.4. The regions of interest for the length recovery must be set with respect to a point of detachement (Fig. 9.2).

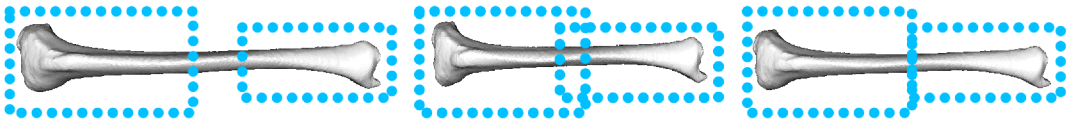

Too long Too short Correct length

Figure 9.4: Relation between vertex assignment and resulting bone length. No assignment of the vertices in the middle of the shaft to any of the fragments leads to a bone that is too long *(left)*. Assignment of the vertices to both fragments results in a bone that is too short *(middle)*. The correct length is ensured by assigning each vertex to exactly one fragment *(right)*.

9.3.2.3 *Optimization Scheme*

The registration is solved as a non-linear least squares (NLS) problem, using a numerical Levenberg-Marquardt optimizer [59]. Although a computationally demanding approximation of the Jacobian matrix is required, due to its high rate of convergence, the optimizer is able to outperform stochastic gradient-free methods [KCZ+16]. The Jacobian matrix J_F has the following form:

$$J_F = \begin{pmatrix} \partial PD_{prox}(\mathcal{P})/\partial p_{prox} & 0 & \partial PD_{prox}(\mathcal{P})/\partial \mathbf{b} \\ 0 & \partial PD_{dist}(\mathcal{P})/\partial p_{dist} & \partial PD_{dist}(\mathcal{P})/\partial \mathbf{b} \\ \partial RV(\mathcal{P})/\partial p_{prox} & \partial RV(\mathcal{P})/\partial p_{dist} & \partial RV(\mathcal{P})/\partial \mathbf{b} \end{pmatrix} \tag{9.8}$$

where the partial derivates are approximated using central differences as $\partial f(t)/\partial t \approx f(t+\epsilon) - f(t-\epsilon)/2\epsilon$.

The reconstruction is divided into three subsequent optimizations. At first, only poses p_{prox}, p_{dist} are considered. Next, the first five shape modes $b_1 \dots b_5$ are optimized together with the poses. Finally, all modes $\mathbf{b}$ are involved in the last stage. Before the optimization, a rough initial pose of the statistical shape model together with the regions of interest must be set interactively by the user, or estimated from the segmentations, as described in the following sections. The binary segmentations of the input radiographs are performed manually. The modes of variation of the shape model are initialized to zeros.

9.4 RESULTS

The accuracy and performance of the proposed method were evaluated on synthetic X-ray images of simulated fractures and on real radiographs of dry cadaveric bones suffering perimortem injuries. To evaluate the accuracy, the differences between the polygonal models reconstructed by the proposed method, and ground-truth surfaces obtained from CT data sets were measured using the symmetric Hausdorff distance [10]. The CT data sets of ground-truth bones were never in-

cluded into the training sets of the statistical shape models. Following the reconstruction convergence criterion stated in [11], the method converged in each evaluated case, as the RMS error was always lower than 3 mm. The ϵ for the Jacobian matrix approximation was set to 1 mm or 1° in the case of pose parameters and to 1 standard deviation σ for shape modes $\mathbf{b}$, as previously proposed in [KKŠZ16a].

The evaluations were performed using a 64-bit Windows 7 desktop machine, equipped with an Intel i5 processing unit, NVidia GTX 980Ti 6 GB graphics adapter and 24 GB DDR4 RAM.

9.4.1 *Simulated Injuries*

For the *in silico* evaluation of the fracture reduction, we adopted a data set of virtual X-ray images, previously presented in [KKŠZ16a]. The virtual radiographs were ray-casted from 8 already segmented CT images of femoral bones obtained from the `Virtual Skeleton Database (VSD)` [63]. From each CT image, 12 virtual stereo pairs of orthogonal radiographs were created, resulting in 96 cases in total. As the bones were rotated 30° along the longitudinal axis between the individual renderings, the data set contained X-ray images captured even from arbitrary views, in addition to standard anterior-posterior and lateral radiographs. The source-image distance (SID) was set to exactly 1 meter; the pixel spacing of the radiographs was set to 0.75 mm. To simulate transversal fractures of the femoral shaft, each radiograph was split into proximal and distal parts. A sample test case chosen from the evaluation data set is shown in Fig. 9.5.

Initial poses of the statistical shape model were generated randomly, with uniform distribution and maximum difference to the ground-truth poses limited to ± 10 mm and $\pm 10°$, respectively.

Fig. 9.5 shows the result of the virtual fracture reduction of the sample test case. As the virtual radiographs and the reference polygonal models were obtained from the same CT images, the reconstructed bones were compared directly with ground-truth surfaces. The accuracy evaluation for each bone, together with the size of the nonoverlapping area, the number of misassigned tetrahedral vertices, and the length error, as well as the performance evaluation, including the overall reconstruction time, number of iterations in each stage and a total number of rendered images, are shown in Table 9.2. The results for each bone were averaged from 12 evaluations using different stereo radiographic pairs.

The virtual reduction method extends the *Black & White Pixel Differences* (BW-PD) approach proposed in [KKŠZ16a], designated for a single-fragment 2D-3D reconstruction of the uninjured bones. Evaluated on the same synthetic data set, the `BW-PD` method reached an average accuracy of 1.02 ± 1.35 mm when reconstructing

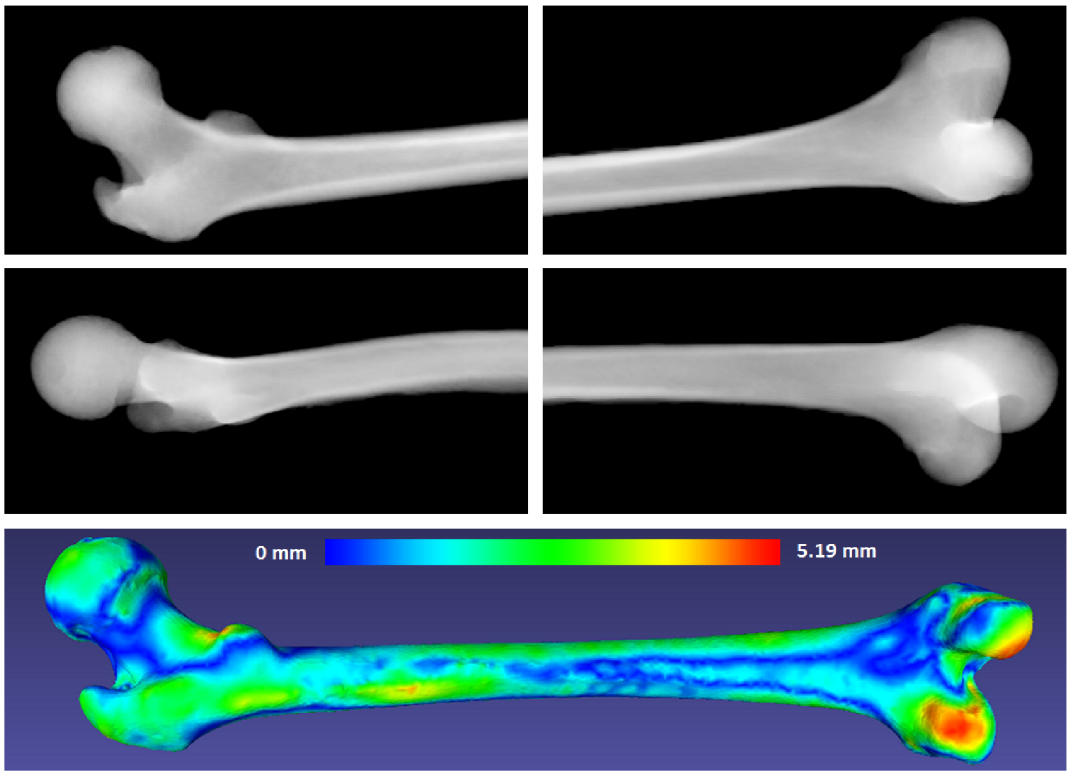

Figure 9.5: A sample test case of stereo radiographs with simulative transversal fracture of the femoral shaft, chosen from the virtual data set *(top)*. Accuracy of the sample case reconstruction *(bottom)*. The heatmap shows the differences between reconstructed and ground-truth surfaces, evaluated using the symmetric Hausdorff distance.

the uninjured bones, while the proposed method reached $1.48 \pm 1.16\,\text{mm}$ when performing virtual reduction of simulated shaft fractures.

9.4.2 *Dry Cadaveric Bones Study*

The cadaveric study involved archeological bones, two femoral and one tibial, suffering peri-mortem diaphyseal fractures. A sample bone from the study is shown in Fig. 9.6. The radiographs of individual fragments were taken sequentially, using a Kodak Carestream Directview DR 9500 System imaging system. Two computed radiography (CR) X-ray cassettes with dimensions of 35×43 cm and 0.168 mm pixel spacing were exploited for the captures. The source-image distance was set to approximately 1 meter. The radiographs were calibrated using a custom made radiostereometric biplanar calibration box, described in detail in [KNM+18]. The complete experimental set up for capturing radiographs is shown in Fig. 9.6. Individual bone fragments, sealed in a foil sleeve, were placed approximately in the center of the box, on Styrofoam underlays. Contrary to the synthetic data set, the radiographs were taken only from the anterior-posterior and lateral views. Af-

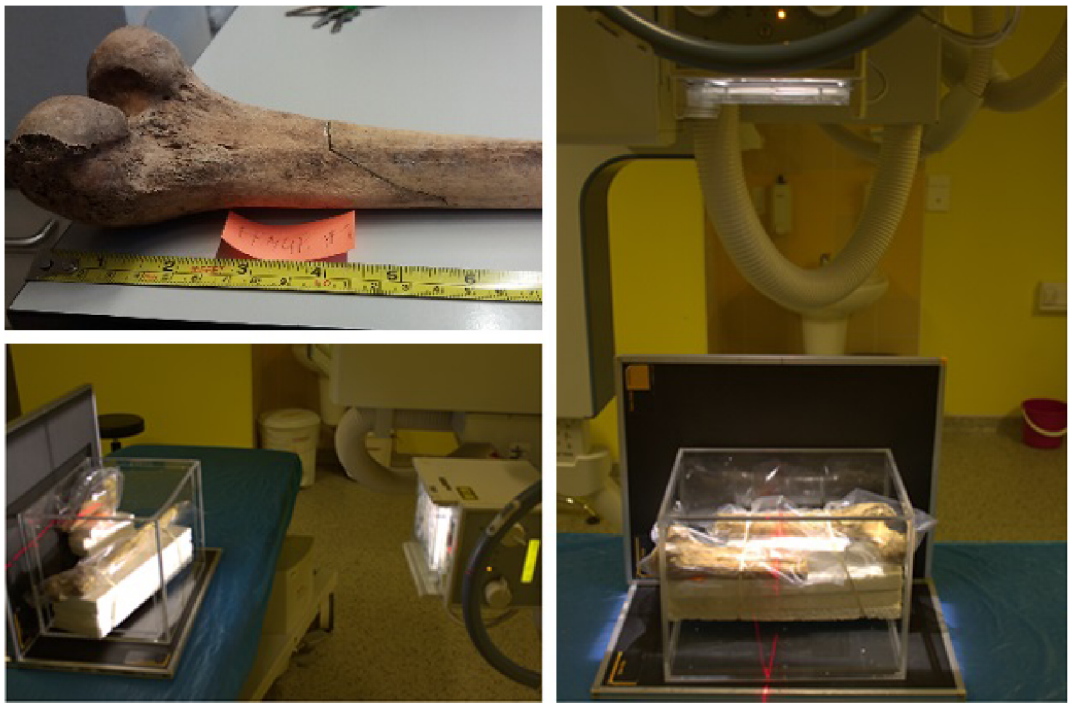

Figure 9.6: Physically reduced dry cadaveric femur involved in the study *(top-left)*, capturing an anterior-posterior radiograph of the experimental setup *(right)*, taking a lateral radiograph *(bottom-left)*.

ter capturing the radiographs, the fractures were actually reduced and fixed by gluing individual fragments together. Then, the reference polygonal models were obtained from CT images of the reduced bones. The poses of the statistical shape model were initialized interactively in a custom viewer.

In contrast with the *in silico* study, rigid registration of the reconstructed bones onto the reference models had to be performed before the Hausdorff distance evaluation. The results of the evaluation are shown in Table 9.2, revealing a slight decrease in accuracy for the cadaveric bones. The accuracy was affected by the manual segmentation and the real-world calibration of the radiographic images; the higher RMS error in comparison with the simulative data set was caused by certain degradations of the archeological bones involved. The higher number of misassigned tetrahedral vertices was related to a user estimation of the separation spot, which was, by contrast, ideal in the case of the *in silico* study.

Table 9.2: Results of the reconstruction accuracy and performance evaluation.

Bone	Nonoverlapping area (%)	Misassigned vertices	Length error (mm)	Mean Hausdorff dist. (mm)	RMS error	Overall time (mm:ss)	Iterations			Renderings
							Stage 1	Stage 2	Stage 3	
VSD identif.				*Simulated fractures*						
226	2.34	11.0	0.57	1.28	0.99	1:54.4	55.6	16.3	12.9	9,609
230	2.38	6.3	1.06	1.23	0.95	1:59.0	48.8	21.7	14.8	10,454
238	2.60	10.3	0.49	1.61	1.27	2:15.2	63.3	21.1	15.0	11,248
254	2.56	13.3	2.16	1.54	1.20	3:55.2	84.0	79.6	22.5	20,550
5900	2.85	6.7	4.07	1.31	1.02	3:04.5	80.2	66.3	12.7	15,387
5953	2.60	3.7	2.77	1.41	1.09	2:11.1	56.5	20.1	15.9	11,149
6009	2.85	8.1	1.44	1.70	1.35	2:57.6	66.1	58.5	16.3	15,343
5939	3.33	15.0	0.94	1.78	1.43	2:11.9	67.9	40.3	10.6	11,583
				Perimortem fractured dry cadaveric bones						
Femur 1	3.41	86	3.8	1.89	2.16	3:49.3	11	48	38	19,752
Femur 2	2.33	50	3.1	1.38	1.70	2:16.7	42	24	21	12,684
Tibia	3.50	131	2.0	1.73	2.16	1:13.0	17	34	13	9,160

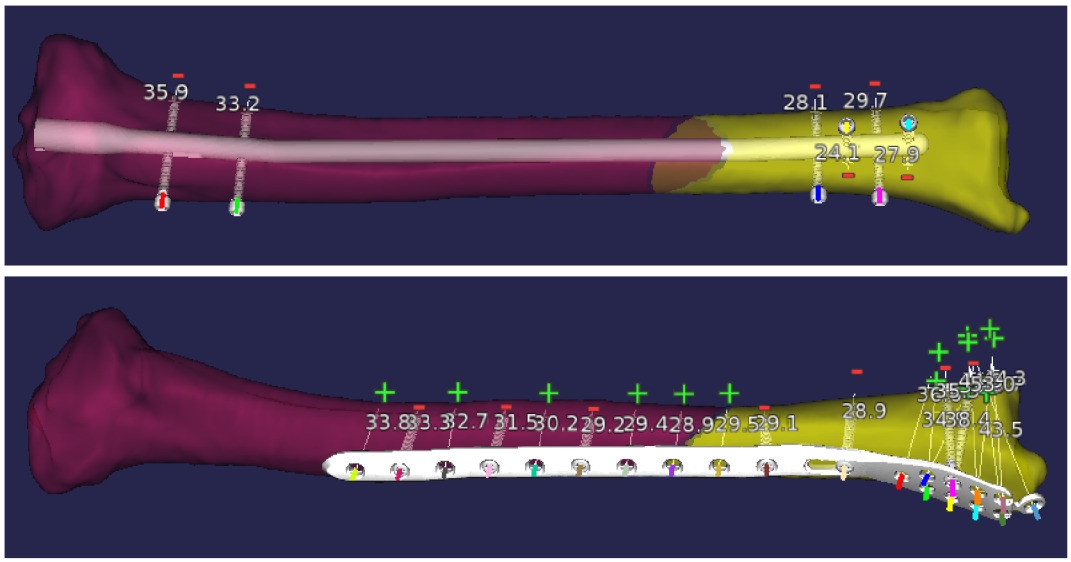

Figure 9.7: A virtual simulation of intramedullary nailing of a tibial shaft fracture *(top)*, and a virtual placement of a distal tibial bone plate *(bottom)*. The bone model was reconstructed from radiographs of a real traumatology case.

9.4.3 *Preoperative Planning Software*

The method has been built into preoperative planning software, which provides a large database of 3D models capturing bone plates and intramedullary nails. The user is able to select the intended device from the database, place it interactively onto the reconstructed bone model, possibly to perform a virtual bending of the bone plate, and finally refine its pose using an automatic procedure. The application also provides the cutting planes of the obtained polygonal model as a tentative approximation of the fracture detachment sites, or measurements of required screw lengths (Fig. 9.7). A mutual pose of stereo radiographs is determined using a calibration marker, which is usually attached to a lower limb splint. The shape model is initially aligned with the longitudinal axes of fragments, which are reconstructed in 3D from the binary segmentations.

9.5 DISCUSSION AND CONCLUSIONS

In this paper, we proposed a method for a virtual 2D-3D reduction of shaft fractures of the lower limbs. To the best of our knowledge, no other method considering multifragment 2D-3D reconstruction with a focus on accurate length estimation has been proposed so far. The accuracy of the method is comparable even with single-fragment reconstruction approaches, presented in a brief summary in [11]. The results revealed that the accuracy and performance are sufficient for involvement in preoperative planning software designed for the selec-

tion of the best-fitting fixation material. To omit the manual segmentation of input radiographs, which is a time-consuming and subjective task, the future work will focus on replacing the nonoverlapping area measure with density-based registration. We assume that the length estimation based on assigning the statistical shape model vertices to individual bone fragments is straightforwardly generalizable, even for application in virtual fracture reduction using 3D models of the fragments obtained from CT images, as proposed e.g. in [6]. The reconstruction method is distributed as open-source library and front-end application at `https://github.com/klepo/libmultifragmentregister`.

ACKNOWLEDGEMENTS

This work was supported by the Technology Agency of the Czech Republic Grant No. TE01020415 V3C - Visual Computing Competence Center and by the Ministry of Education, Youth and Sports of the Czech Republic within the National Sustainability Programme project No. LO1303 (MSMT-7778/2014).

9.6 APPENDIX

9.6.1 *Details on Cadaveric Data Set Evaluations*

Cadaveric bones from archeological research of the Slavkov gallows [26], with evidence of non-healed long bone fractures originated *perimortem*, were used for the reconstruction evaluation. A brief summary of involved bones is shown in Table 9.3. The bones suffered transverse or oblique diaphyseal fractures, the second femur had also degraded greater trochanter, as shown in Figure 9.8 *(right)*. The parts of radiographs related to the degraded trochanter were treated as drop-outs and omitted from the registration to prevent affecting the reconstruction accuracy. For the evaluation of the fracture reduction and length estimation, the bones were equipped with tantalum beads and packed into the foil sleeve, as illustrated in Figure 9.9. Radiographs of the individual fragments are shown in Figure 9.10, resulting models of reduced intact bones with accuracy visualisation are depicted in Figure 9.11.

Table 9.3: Summary on cadaveric bones used for the evaluation.

Bone	Fracture type	Bone length (cm)	Laterality
Femur 1	Oblique	47.5	Sinister
Femur 2	Transversal	47	Sinister
Tibia	Transversal	36	Dexter

Figure 9.8: Transverse diaphyseal fractures of cadaveric bones *(left and middle)*. Degraded greater trochanter of the second femur *(right)*.

Figure 9.9: Marking the bone fragments with tantalum *(left)* beads and packing into the foil sleeve *(right)*.

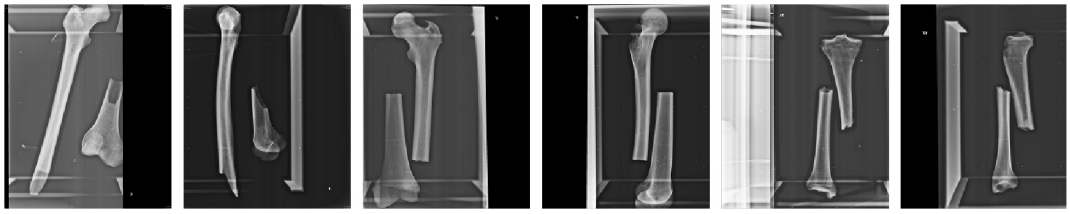

Figure 9.10: Captured radiographs of the cadaveric bones used for the evaluation. The corresponding reconstructed models are shown in Figure 9.11.

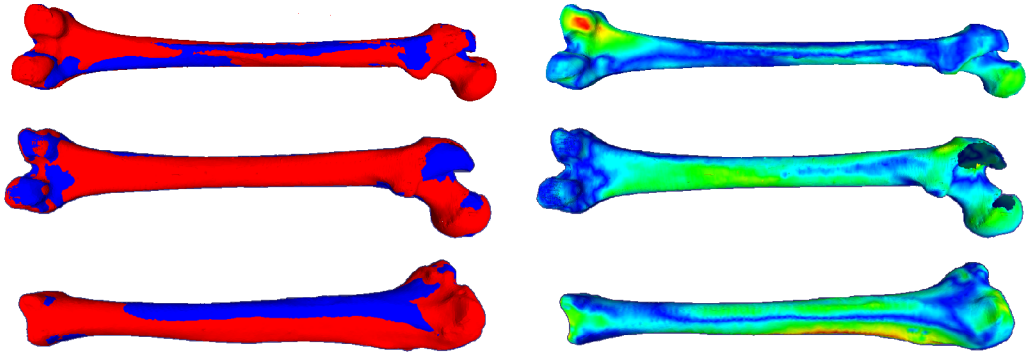

Figure 9.11: Reconstructed models of cadaveric bones femur 1, femur 2 and tibia. The reconstructed bones *(blue)* aligned to the ground-truth models obtained from computed tomography images *(red)*. Differences in the shape are visualised using heatmaps. The maximal differences, highlighted with red color, were 9.69, 8.83 and 6.24 mm respectively. The degraded trochanteric parts of the second femoral bone were discarded from the reconstruction.

Part III

SUMMARY

This part contains further discussions and concludes the thesis.

10 DISCUSSION

The main scientific contribution of the thesis was experimentally verified by designing a method for the reconstruction of intact bone models from radiographs of individual fragments, which overcomes the capabilities of the state-of-the-art reconstruction methods. Individual proposed steps were described and evaluated in the papers included above.

10.1 REVISION OF NON-OVERLAPPING AREA REGISTRATION

The proposed intensity-based non-overlapping area approach [KNM+18], formulated as a nonlinear least squares problem and optimised using a Levenberg-Marquardt solver, clearly outperforms the original contour-based solution [124], reaching similar accuracy as the state-of-the-art methods [54, 90] used in the field of the model-based radiostereometric analysis. On the other hand, in contrast with the feature-based methods, the revision does not require decimation of high poly models [56, 102], offers straightforward hardware acceleration and simple interpretation of the optimized objective function. The key factors influencing the registration accuracy are the ability to handle the drop-outs, the pixel-wise minimization of the uncommon area, and the coarse-to-fine strategy of the Jacobian matrix approximation.

The effect of the coarse-to-fine approximation strategy is visible between the preliminary results in Appendix A and the final study, presented in Chapter 5. Although slightly affected also by the different shape of the femoral stem and the radial plate, the involvement of the coarse-to-fine strategy [KNM+18] brought an order of magnitude improvement of the accuracy in contrast with the preliminary results [KCK+17]. Studies involving state-of-the-art methods usually use several subsequent combinations of the similarity metric and the optimization approach, while the coarse-to-fine strategy allows reaching the fine accuracy only by gradually increasing the resolution of the numerical approximation.

The effect of the pixel-wise optimization was experimentally verified in terms of patient-specific bone model reconstruction. The non-overlapping area, referred to as *Black&White Pixel-Differences*, was compared with *Black&White Sum of Squared Differences* method, which is a modification using a scalar-valued objective function. The pixel-wise formulation clearly outperformed the scalar-valued modification

in terms of the registration accuracy. The evaluation revealed the pixel-wise non-overlapping area takes into account local features differences, while the scalar-valued approach minimizes only a global similarity.

Results presented in Section 5.4.1 reveal a relatively high capture range of the method, however, the resulting accuracy is correlated with a proximity of the initial estimation to the ground-truth pose, which is usual for optimization based registration. The non-overlapping area is in contrast with other approaches easily interpretable, thus the resulting value of the optimized objective function may be used for an estimation of the reconstruction accuracy. As based on least squares formulation, the method is usable even without segmentation of the input radiographs in the case of highly radiopaque objects. However, with the non-segmented X-ray images, the objective function loses its uncommon area interpretation and the accuracy slightly decreases, while still reaching reliable values. The method is also quite robust, as within the scope of the performed experiments the optimization never failed when given a reasonable initial pose guess. To lower the resources consumption during the optimization, it is possible to crop the input X-ray images. However, it is necessary to preserve certain margins to keep space for the non-overlapping areas, taking into account the initial pose estimates.

10.2 RECONSTRUCTION OF MODELS OF UNINJURED BONES

The intensity-based non-overlapping area approach is suitable for the reconstruction of patient-specific 3D anatomy models [KKŠZ16a]. In contrast with feature-based methods, the non-overlapping area is computationally straightforward, as it does not require feature matching between the detected contour and the model silhouette or surface. The method also does not require a complete contour of the bone, as it supports drop-outs, which may be caused by occlusions, limited field of view, or pathologies However, the non-overlapping area is not capable of reconstructing the internal bone structures, such as spongy and compact tissues, which may also contribute to the preoperative planning, indicating the minimal required length of the bone screws for instance. Moreover, the density-based registration may be advantageous for usage with non-segmented radiographs, reducing the amount of user interaction during the process, although the user must still preprocess the input radiographs by providing the model initial pose estimation, which must be generally close to the ground-truth solution in such cases. On the other hand, the involvement of density information does not improve the accuracy of the reconstructed surface, when the segmentation is available, as shown in Section 6.4.1. The higher accuracy of the non-overlapping area approach is given by its sensitivity to local features, achieved by a pixel-wise resolution of the residual

vector and the corresponding Jacobian matrix. The experimental evaluations also reveal the Levenberg-Marquardt solver is for its high rate of convergence effective optimizer in terms of reconstruction speed.

In contrast with other studies [11, 133], the optimization does not include a regularizer term increasing the probability of the shape model instance, reached by favoriting shapes close to the mean. The penalizer term, formulated as $\sum_i s_i^2$, where s_i are shape modes of the involved atlas, is of importance for the model regression on a sparse feature set, for instance consisting of raw edges detected in radiographs, as proposed by [11]. The purpose of fitting the model to the edges is to avoid the manual assistance required during the contour detection, allowing the method to be used automatically, in case of [11, 12, 13] for fluoroscopic sequence analysis focusing on joint kinematics observation. On the other hand, evaluations suggest the contour or segmentation provides sufficiently dense information for accurate reconstruction itself, therefore the regularizer term is not necessary. Moreover, experiments involving a sufficiently large data set reveal the penalizer tends to shrink the shape variability to the average, negatively affecting the reconstruction accuracy.

10.2.1 *Comparison of Levenberg-Marquardt Solver with Evolution Strategies*

The evaluation of registration methods using different optimizers reveal the Levenberg-Marquardt optimisation outperforms the Covariance Matrix Adaptation and Covariance Matrix Self Adaptation Evolution Strategies in terms of the registration speed, although the stochastic methods do not require computationally demanding numeric approximation of the Jacobian matrix. The computation of the Jacobian matrix is compensated by the high rate of convergence of the Levenberg-Marquardt method, leading to its higher effectivity in comparison with the evolution strategies.

10.2.2 *Lossy Compression of Statistical Shape and Intensity Models*

The evaluations also revealed that the density information involved in the statistical shape and intensity models may be effectively compressed with only a slight effect on the reconstruction accuracy.

10.3 RECONSTRUCTION OF FRACTURED LONG BONES

The proposed method for a 2D-3D reconstruction with simultaneous reduction of injured long bones, suffering dislocated diaphyseal fractures, was experimen-

tally verified using virtual X-ray images and real radiographs of cadaveric bones. The evaluations clearly show the reconstruction of fractured bones is feasible and sufficiently accurate for purposes of digital 3D templating. The presented approach was built into an experimental preoperative planning application, focused on patient-specific identification of the best-fitting fixation material, with a focus on intramedullary nails and bone plates. In contrast with similar existing preoperative planning systems, the presented application is focused on osteosynthesis of fractured bones, instead of joint arthroplasties.

The main challenge related to fracture reduction is a correct estimation of the bone length. As the length is independent of the morphology of proximal or distal fragments, the estimation is based on the idea that every piece of the statistical shape model must belong to exactly one of the fragments. The idea is implemented in the form of a regularizer term, which penalizes vertices of the model assigned to none or both fragments at the same time. Thus, the penalizer performs splitting of the statistical shape model into the individual fragments, ensuring accurate estimation of the bone model length. Beyond the non-overlapping area approach, the length regularization is feasible also within the density-based method.

As the first shape mode of the long bones statistical models describe mainly the bone length, it is also possible to initiate the model to a certain length, previously measured in the radiographs. However, since the first mode has an essential, but not exclusive influence on the length, the optimization approach provides significantly better results. Also using the externally provided length estimate for a shape model initialization has limited benefits, as the length is optimized within the first iterations of the optimization and most of the time is spent for tuning the fine details and local features. In conclusion, the optimisation-based length recovery provides the most accurate estimation and does not require any special initialization of the statistical shape model.

11

CONCLUSION

The thesis presented novel model-based registration methods for the analysis of conventional radiographs in terms of preoperative planning and roentgen stereophotogrammetry.

The main research question of the thesis was focused on the verification if it is possible to reconstruct a three-dimensional model of a complete and intact bone only from radiographs capturing its proximal and distal fragments. The verification was performed by designing a novel method, based on automatic splitting of the statistical shape model into the individual fragments, leading to an accurate estimation of the bone length. The evaluations including virtual and cadaveric injuries revealed the resulting reconstruction accuracy is sufficient for involvement in preoperative planning with a focus on 3D digital templating. Designing the reconstruction pipeline required additional contributions, including revision of the non-overlapping area registration approach leading to significant improvements of its accuracy, comparison with a density-based registration revealing the higher accuracy of the non-overlapping area approach, and selection of effective optimisation method.

The method designed for reconstruction of fractured bones was included in the experimental part of the preoperative planning application called TraumaTech, intended for clinical evaluations. The application is focused on the digital 3D templating for the identification of the best-fitting fixation material for the treatment of the femoral, tibial, radial, and humeral fractures. The proposed method allows performing the templating without the necessity of previous computed tomography examination. Further descriptions of the application are available at the TraumaTech product website[1] and in the Youtube video[2]. The appearance models involved in the application for the patient-specific anatomy reconstruction are summarized in Supplement G.

Main possibilities for further development aim at reducing the amount of user assistance required during the registration process by using emerging deep learning methods. A straightforward solution to partially automatize the registration process is to perform the X-ray image segmentation using approaches based on convolutional neural networks [21, 107]. Another way is to exploit directly a

[1] https://www.tescan3dim.com/solutions/medical-software/digital-orthopaedics

[2] https://youtu.be/GJvV7M2ksvQ

learning-based registration method instead of the conventional optimization-based approach [69, 79, 120, 70, 78]. Current learning-based studies present mostly rigid 2D-3D registration methods focused on fitting computed tomography volumes or virtual models of instruments into fluoroscopic sequences for usage within the fields of computer-assisted procedures or navigation. In addition to the real-time performance, the learning-based approaches also offer a high degree of automatization, omitting the dependency on the initial pose estimation and its influence on the resulting accuracy. Thus, a formulation of a non-rigid learning-based method for shape-constrained atlas 2D-3D registration would be of great impact. In an ideal case, the whole system should work without the dependency on any calibration marker to be able to analyze a usual clinically available radiographs, perform in real-time, and with minimal contributions provided by the clinician.

Part IV

APPENDIX

This part consists of conference abstracts presenting the preliminary results of tge papers included above. The short paper [KCK+17] presents an evaluation of intensity-based non-overlapping area using a radial bone plate. In contrast with [KNM+18], the evaluation was performed without the coarse-to-fine strategy of the Jacobian matrix numerical approximation, thus reaching significantly lower accuracy. Abstract [KKŠZ15] is focused on the density-based registration pipeline construction and acceleration using graphics hardware. Extended abstract [KKŠZ16b] is focused on a fracture reduction using a statistical shape and intensity model, evaluated on a synthetic data set.

A

MODEL-BASED RADIOSTEREOMETRIC ANALYSIS USING INTENSITY-BASED 2D/3D REGISTRATION PIPELINE: FEASIBILITY STUDY

CITATION

Ondřej Klíma, Adam Chromý, Petr Klepárník, Michal Španěl, and Pavel Zemčík. Model-based radiostereometric analysis using intensity-based 2D/3D registration pipeline: Feasibility study. Conference Materials and Posters of Spring Conference on Computer Graphics SCCG 2017, pages 31–33. Mikulov: Vysoké učení technické v Brně, 2017. http://sccg.sk/ (*extended abstract*)

ABSTRACT

Model-based radiostereometric analysis (MBRSA) methods exploit, in most cases, feature-based 2D/3D registration. In this paper we focus on a feasibilty of the intensity-based 2D/3D registration approach applied in MBRSA. To evaluate the feasibility, we created a data set containing stereo pairs of both synthetic and real radiographic images of a metallic radius bone implant. Evaluation, we performed and present, reveals sufficient accuracy of the intensity-based registration pipeline and its robustness to image artifacts. The results obtained using synthetic radiographs show comparable accuracy with the feature-based non-overlapping area (NOA) approach. The registration process using real X-Ray images did not require preprocessing of the input radiographs neither was significantly affected by the presence of the metallic bone screws. This study presents an introductory part of an ongoing research.

KEYWORDS

Radiostereometric analysis, Implant migration, 2D/3D registration, Levenberg-Marquardt optimization

Model-based Radiostereometric Analysis Using Intensity-based 2D/3D Registration Pipeline: Feasibility Study

Ondrej Klima[a,*], Adam Chromy[b], Petr Kleparnik[a], Michal Spanel[a], Pavel Zemcik[a]

[a] *Brno University of Technology, Faculty of Information Technology, IT4Innovations Centre of Excellence, Božetěchova 1/2, 612 66 Brno, Czech Republic*
[b] *Brno University of Technology, Faculty of Electrical Engineering and Communication, Technicka 3082/12, 616 00 Brno, Czech Republic*

Abstract

Model-based radiostereometric analysis (MBRSA) methods exploit, in most cases, feature-based 2D/3D registration. In this paper we focus on a feasibilty of the intensity-based 2D/3D registration approach applied in MBRSA. To evaluate the feasibility, we created a data set containing stereo pairs of both synthetic and real radiographic images of a metallic radius bone implant. Evaluation, we performed and present, reveals sufficient accuracy of the intensity-based registration pipeline and its robustness to image artifacts. The results obtained using synthetic radiographs show comparable accuracy with the feature-based non-overlapping area (NOA) approach. The registration process using real X-Ray images did not require preprocessing of the input radiographs neither was significantly affected by the presence of the metallic bone screws. This study presents an introductory part of an ongoing research.

Keywords: Radiostereometric analysis, Implant migration, 2D/3D registration, Levenberg-Marquardt optimization

1. Introduction and Related Work

Radiostereometric Analysis (RSA), proposed by Selvik [1], is a method for monitoring the fixation of an implant within a bone [2]. The analysis allows an identification of a micromotion between the implant and the bone. The RSA method is indicated especially in cases of total joint replacement, such as total knee (TKA) or total hip (THA) arthroplasty [3, 4, 5]. The method is based on pairs of stereo radiographs. The traditional approach exploits tantalum markers injected into the bone together with markers attached to the implant. The tantalum markers are shown in Figure 1. Markers positions in the 3D space are obtained by triangulation from the radiographic stereo pair. The patient commonly undergoes several following-up examinations during the two years after the intervention [6]. The implant migration is revealed when the relative pose between the bone markers and the implant markers differs among the examinations.

However, several issues exist related with attaching markers to the implant. The markers attached to the implant may be occluded in the radiographs by the implant itself, the marked implants are significantly more expensive, and moreover, the implants may be weakened by the markers [2]. These issues are addressed by the model-based radiostereometric analysis (MBRSA), proposed first by Valstar [7]. The method is based on a 2D/3D registration of a virtual implant model into the radiographic stereo pair instead of marking the implant, while the bone markers remain involved.

*Corresponding author. Tel.: +420 54114-1402
Email address: iklima@fit.vutbr.cz (Ondrej Klima)

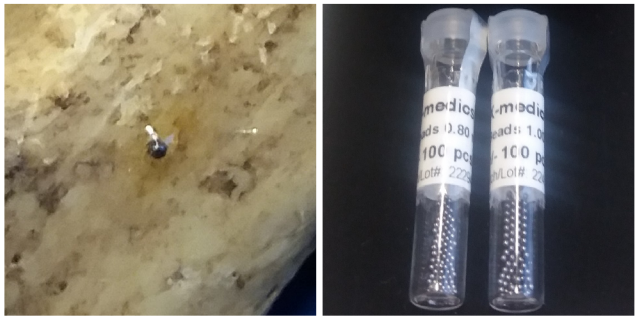

Figure 1: A tantalum bead of 0.8 mm in diameter glued to a dry cadaveric bone (left). A packing of two hundred tantalum markers (right).

Most of the model-based RSA methods depend on *feature-based* registration, exploiting the edges detected in the radiographs [7, 2, 4]. We have recently proposed an *intensity-based* method for the 2D/3D registration of a bone atlas into the X-Ray images [8]. The main goal of this preliminary study is to verify that the intensity-based registration is feasible in terms of the model-based radiostereometric analysis using the previously proposed approach.

2. Intensity-based Registration Method

The aim of the registration is to recover an accurate pose of the implant model within the 3D space of the stereo radiographic pair. A rough initial pose estimate provided by a user is required. The proposed method is designed for binary images.

The registration is performed as an iterative optimization. Digitally reconstructed radiographs (DRR) are rendered from

the implant model in current pose in each iteration. A similarity between the DRR images and the radiographs is evaluated using the mean square error (MSE) measure. The rotation and translation of the model are consequently adjusted to minimize the differences between the real and the virtual radiographs. The resulting pose of the implant model is obtained when the dissimilarities are minimal.

The registration is formulated as a non-linear least squares (NLS) problem:

$$p^* = \arg\min_p \frac{1}{N} F(p)^T F(p) \tag{1}$$

where $p = (R, T)$ is a pose vector formed by the rotation and translation of the implant model, N is a count of pixels contained in the radiographs and $F(p)$ is a vector of residuals between the original X-Ray and DRR images:

$$F(p) = \begin{pmatrix} \text{vec}(\text{DRR}_{AP}\ (x) - \text{XRay}_{AP}\ ) \\ \text{vec}(\text{DRR}_{LAT}(x) - \text{XRay}_{LAT}) \end{pmatrix} \tag{2}$$

where $|F(p)| = N$. The optimization is solved using the Levenberg-Marquardt algorithm [9], which is a highly effective method in terms of 2D/3D registration [10]. The accuracy of the method strongly benefits from the optimization on a pixel level [8]. The optimization can be interpreted as a minimization of a non-overlapping area (NOA) between the real and virtual radiographs, similarly to the approach proposed by Valstar [7].

3. Experimental Results and Discussion

3.1. Synthetic Radiographs

The accuracy of the intensity-based method was evaluated using synthetic radiographs. The radiographs were generated as binary images from a polygonal model of a radius bone implant consisting of 71,689 vertices and 143,762 faces. The virtual X-Ray images were of size 849 × 206 and 873 × 277 pixels respectively with horizontal and vertical pixel spacing equal to 0.143 mm. Consequently, the vector of residuals $F(p)$ was formed by 416,715 elements. The registration was repeated 10 times, initialized with various randomly generated pose estimates. The differences between the initial and the ground-truth poses were limited to ±9 mm in translation and ±9 ° in rotation. The registration took 55 iterations on average.

Table 1: Distributions of translational errors (n = 10).

	T_x [mm]	T_y [mm]	T_z [mm]
Mean	0.033	-0.010	-0.068
Std. Dev.	0.139	0.013	0.106

Table 2: Distributions of rotational errors (n = 10).

	R_x [°]	R_y [°]	R_z [°]
Mean	-0.107	-0.406	-0.009
Std. Dev.	0.133	0.566	0.231

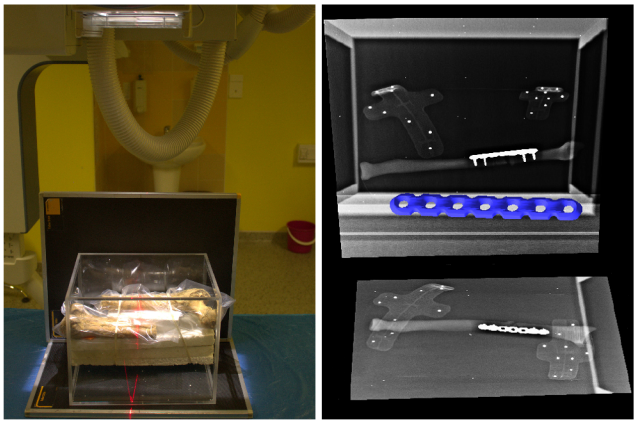

Figure 2: Illustration of the experimental setup placed in the X-Ray machine (left). The actual calibrated radiographs capturing the bone model with attached implant (right). In front of the radiographs there is a virtual model of the implant, highlighted by a blue color.

The results are shown in Table 1 and Table 2 as translational and rotational error distributions with respect to individual axis. The highest rotational and the lowest translational errors occurred in case of the y axis, which corresponds to the longitudinal axis of the implant model. This is an expected result as the virtual X-Ray images were taken approximately in xy and yz planes in the space of the implant model.

Table 3 shows comparison between the intensity-based registration pipeline and the feature-based NOA approach. The intensity-based method has slightly larger rotational error, but on the other hand is more accurate in translation. However, this comparison is rather tentative according to a different nature of evaluation data sets and a different kind of involved implants. The radius bone implant is not significantly asymmetric in comparison with implants dedicated for THA and TKA interventions.

Table 3: The largest standard deviations for translation and rotation.

	T [mm]	R [°]
NOA (Valstar [7])	0.221	**0.524**
Proposed approach	**0.139**	0.566

3.2. Real Radiographs

An illustration of the experimental setup is shown in Figure 2 left. The radiographs were taken using the X-Ray cassettes of size 35 × 43 cm and calibrated using a custom made biplanar RSA cage. The captured object is placed on the Styrofoam inside the Plexiglas calibration cage. For the real-world evaluation of the method we used a plastic model of a fractured radius bone with a metallic bone plate. The bone plate was attached to the plastic model using metalic screws. Radiographs of the model were taken serially from anterior-posterior and lateral views and calibrated using the DLT approach [11]. The actual radiographs are shown in Figure 2 right.

A rough initial pose of the implant model in the 3D space was set interactively. The initial pose is shown in detail in Fig-

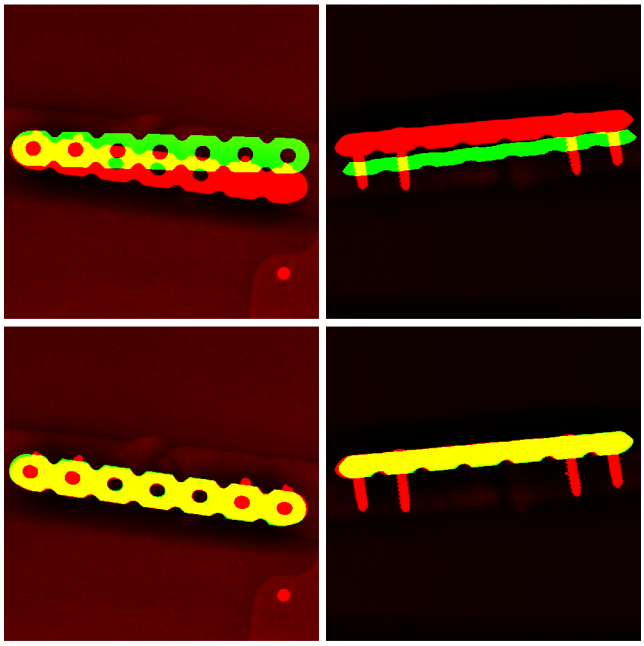

Figure 3: Initial pose of the implant provided by the user (top). The resulting pose recovered by the proposed 2D/3D registration method (bottom).

ure 3 in the top row. The original radiographs are visualized by a red color and overlayed by green shaded DRR images rendered from the implant model. The overlapping area is emphasized by a yellow color.

Although the method is dedicated for binary images, the original radiographs were used for the registration instead. This was possible due to high contrast between the metallic bone plate and the surroundings. The registration process took 72 iterations, the final result of the registration is shown in Figure 3 in the bottom row. It can be seen that the registration did not fail due to lower contrast surroundings, nor due to the high contrast bone screws which are not a part of the implant model.

4. Conclusion

We have verified that the intensity-based 2D/3D registration is clearly feasible in terms of model-based radiostereometric analysis. Moreover, the radiographs are suitable for the registration without further processing. The quantitative evaluation based on synthetic X-Ray images revealed that the intensity-based method and the feature-based non-overlapping area approach have tentatively comparable accuracy. The currently ongoing work is focused on the real-world accuracy evaluation using the implants dedicated for the THA and TKA interventions. The registration pipeline is publicly available at http://www.fit.-vutbr.cz/~iklima/prods.php?id=458 and http://www .fit.vutbr.cz/ ~iklima /prods.php?id=505.

ACKNOWLEDGEMENTS

This work has been supported by the Internal Science Fund of Brno University of Technology grant no. FEKT/FIT-J-17-4745 Intermodal Registration of 3D Data in Health-care and by the Technology Agency of the Czech Republic grant no. TA04011606 Modern Image Processing Techniques and Computer-based Planning in Trauma Treatment. The authors thank the 3Dim Laboratory s.r.o. for providing the radius bone plate and its virtual model and the University Hospital in Ostrava for capturing the experimental radiographs.

References

[1] Selvik, G.. Roentgen stereophotogrammetric analysis. Acta Radiologica 1990;31(2):113–126. URL http://dx.doi.org/10.1177/028418519003100201.

[2] Kaptein, B., Valstar, E., Stoel, B., Rozing, P., Reiber, J.. A new model-based rsa method validated using cad models and models from reversed engineering. Journal of biomechanics 2003;36(6):873–882.

[3] Madanat, R., Mäkinen, T.J., Aro, H.T., Bragdon, C., Malchau, H.. Adherence of hip and knee arthroplasty studies to rsa standardization guidelines: A systematic review. Acta Orthopaedica 2014;85(5):447–455. URL http://doi.org/10.3109/17453674.2014.934187.

[4] Nazari-Farsani, S., Finnilä, S., Moritz, N., Mattilla, K., Alm, J., Aro, H.. Is model-based radiostereometric analysis suitable for clinical trials of a cementless tapered wedge femoral stem? Clinical Orthopaedics and Related Research 2016;474:2246–2253.

[5] Shareghi, B., Johanson, P.E., Kärrholm, J.. Clinical evaluation of model-based radiostereometric analysis to measure femoral head penetration and cup migration in four different cup designs. Journal of Orthopaedic Research 2017;URL http://dx.doi.org/10.1002/jor.23177.

[6] Valstar, E.R., Gill, R., Ryd, L., Flivik, G., Börlin, N., Kärrholm, J.. Guidelines for standardization of radiostereometry (rsa) of implants. Acta Orthopaedica 2005;76(4):563–572. URL http://dx.doi.org/10.1080/17453670510041574.

[7] Valstar, E., de Jong, F., Vrooman, H., P.M., R., J.H.C., R.. Model-based roentgen stereophotogrammetry of orthopaedic implants. Journal of Biomechanics 2001;34(6):715–722.

[8] Klima, O., Kleparnik, P., Spanel, M., Zemcik, P.. Intensity-based femoral atlas 2d/3d registration using levenberg-marquardt optimisation. Proc SPIE 2016;9788:97880F–97880F–12. URL http://dx.doi.org/10.1117/12.2216529.

[9] Kelley, C.T.. Iterative methods for optimization. Frontiers in applied mathematics; Philadelphia: SIAM; 1999. ISBN 0-89871-433-8. URL http://opac.inria.fr/record=b1096699.

[10] Klima, O., Chromy, A., Zemcik, P., Spanel, M., Kleparnik, P.. A study on performace of levenberg-marquardt and cma-es optimization methods for atlas-based 2d/3d reconstruction. IFAC-PapersOnLine 2016;49(25):121 – 126. URL http://dx.doi.org/10.1016/j.ifacol.2016.12.021.

[11] Choo, A.M., Oxland, T.R.. Improved rsa accuracy with dlt and balanced calibration marker distributions with an assessment of initial-calibration. Journal of Biomechanics 2003;36(2):259 – 264. URL http://dx.doi.org/10.1016/S0021-9290(02)00361-5.

B

TOWARDS AN ACCURATE 3D RECONSTRUCTION OF FRACTURED LONG BONES FROM PLAIN 2D RADIOGRAPHS

CITATION

Ondřej Klíma, Petr Klepárník, Michal Španěl, and Pavel Zemčík. Towards an accurate 3D reconstruction of fractured long bones from plain 2D radiographs. Volume 11 of *CARS 2016—Computer Assisted Radiology and Surgery Proceedings of the 30th International Congress and Exhibition Heidelberg, Germany, June 21–25, 2016*, pages 180–181. International Journal of Computer Assisted Radiology and Surgery, 2016. doi: 10.1007/s11548-016-1412-5 (*extended abstract*)

KEYWORDS

Preoperative planning, Fracture reduction 2D-3D, reconstruction shape prior

Towards an accurate 3D reconstruction of fractured long bones from plain 2D radiographs

O. Klima[1], P. Kleparnik[1], M. Spanel[2], P. Zemcik[1]
[1]Brno University of Technology, DCGM, Brno, Czech Republic
[2]3Dim Laboratory s.r.o., Brno, Czech Republic

Keywords Preoperative planning · Fracture reduction · 2D-3D reconstruction · shape prior

Purpose

Radiographic examinations play an essential role during treatment of traumatized long bones. In case the treatment requires a surgical intervention, a preoperative planning with the aim of the identification of an ideal bone fragments reposition and the best fitting bone plate is commonly involved. Such planning is usually based on 3D models segmented from computed tomography (CT) images of the anatomy of interest. However, the CT examination exposes the patient to higher doses of ionizing radiation and adds more time and costs in comparison to the plain radiographic imaging. Therefore, the possibilities of the preoperative planning based only on plain radiographic images have been investigated in recent years. Reconstruction of the 3D bone shape from the small number of 2D X-ray images is a crucial moment of such planning approach. Most of the reconstruction methods proposed so far focus only on the 2D–3D reconstruction of a single part of the bone and only very few works deal with a 2D–3D reconstruction of the fractured bone [1].

The main goal of this work is a 2D–3D reconstruction with a simultaneous 3D reduction of the fractured bone. The proposed method focuses on the displaced oblique fractures of a femoral shaft. The main contribution of the method is an accurate 3D bone reconstruction and reduction without a prior knowledge of the ground-truth length of the bone. It is assumed that for each bone fragment, X-ray images taken from anterior-posterior and lateral views are available and the relative poses of the radiographs are known. Without loss of generality it is also assumed that each radiograph captures exactly one fully visible fragment of the injured bone.

Methods

The proposed method consists of two parts. The first part performs the shape reconstruction and works as an intensity-based deformable 2D–3D registration. It fits a single shape prior of a complete and uninjured femoral bone into the radiographs capturing the individual bone fragments. As a shape prior, the statistical shape and intensity model (SSIM) [2] created from 22 CT images is involved. Beyond the shape variations, the SSIM describes the bone densities using higher-degree Bernstein polynomials, allowing the rendering of digitally

reconstructed radiographs (DRRs) [3]. We formulate the registration as a non-linear least squares problem solved using the iterative Levenberg–Marquardt algorithm [4], which is the well-established optimization method with the high rate of convergence. In the each iteration, the DRRs are rendered from the SSIM, the similarity between the DRRs and the original X-ray images is evaluated using the normalized mutual information (NMI) measure and the poses and the shape parameters of the SSIM are adjusted for the next iteration. The registration is finished when the differences between the original X-ray and DRR images are minimal; the reconstructed 3D model of the patient's femur is represented by the specific instance of the shape prior.

The second part of the proposed method simultaneously performs the 3D bone reduction. As it might be expected, the shape of femoral bones varies mainly in the length, which is independent on other morphometric features of the bone. Therefore, it is not possible to estimate the bone length only by the deformable 2D–3D registration itself. With respect to the assumptions stated above, the key observation is that each vertex of the shape model must belong to exactly one fragment of the bone. Consequently, each vertex must be rendered only in the radiographs depicting the related fragment. As the least squares formulation of the problem allows involvement of multiple metrics, the registration is extended to maximize the count of the SSIM vertices that are assigned to exactly one fragment and rendered in all its DRRs. The maximization ensures the correct estimation of the bone length and the accurate bone reduction.

Results

The method has been evaluated on a data set created from CT images of 8 people. 12 virtual cases of femoral shaft fractures have been created from each individual, resulting in 96 cases in total. Each case consists of two pairs of the orthogonal virtual X-ray images ray-casted from a segmented CT image. For every case, a tested bone was split approximately in the middle of its shaft. A typical test case is illustrated in Fig. 1, the corresponding reconstructed 3D model is depicted in Fig. 2.

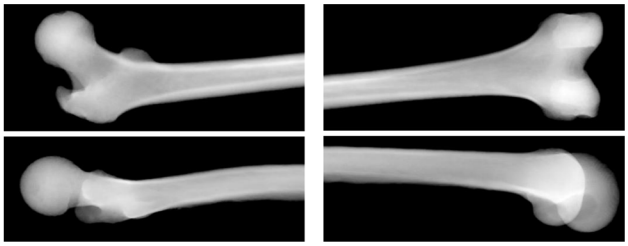

Fig. 1 The sample test case. Two pairs of orthogonal radiographs capturing the proximal (left) and the distal (right) part of the virtually fractured femoral bone

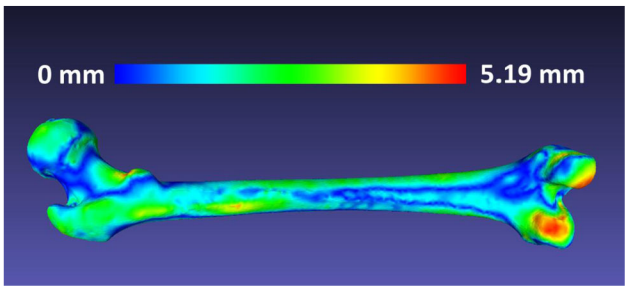

Fig. 2 A polygonal model reconstructed from the sample case. The heat map visualizes the differences from the ground-truth model, mean error was 1.53 mm

The initial estimates of the SSIM pose were generated randomly. The bones used for the evaluation were not included in the training set of the SSIM. First, as a baseline solution, only the 2D–3D registration itself was performed for the test cases. Then the evaluation of the proposed method, including the 3D bone reduction, was performed. The reconstructed 3D models and the ground-truth models segmented from CT images were compared using the symmetric Hausdorff distance [5]. The results are shown in Table 1.

Table 1 The average accuracy of the proposed method is sufficient for the purposes of the preoperative planning, while the results of the baseline solution are significantly inaccurate

	Mean distance [mm]	RMS	Maximal distance [mm]
Proposed method	1.38	1.74	7.26
Baseline	2.52	3.41	11.90

Conclusion

We proposed a novel method for the 2D–3D reconstruction of fractured long bones with accuracy sufficient for the application in the preoperative planning. The results clearly confirm that the 2D–3D reconstruction of a fractured long bone must be performed simultaneously with the 3D bone reduction, as the plain deformable registration fails for not being capable of recovering the bone length. With respect to the promising results reached on the synthetic evaluation data set, the ongoing work will focus on the real world cases evaluation. The proposed method is suitable for straight parallelization and consequent acceleration using graphics hardware (GPU), which makes it applicable within the clinical preoperative planning software.

Acknowledgement

This research has been funded by the Technology Agency of the Czech Republic (TA04011606).

References

[1] Gong RH, Stewart J, Abolmaesumi P „Reduction of multi-fragment fractures of the distal radius using atlas-based 2d/3d registration", in Medical Imaging: Visualization, Image-Guided Procedures, and Modeling, Proc. SPIE 7261, SPIE-The International Society for Optical Engineering (2009).

[2] Yao J, Taylor RH „Construction and simplification of bone density models", in Medical Imaging: Image Processing, Proc. SPIE 4322, 814–823, SPIE-The International Society for Optical Engineering (2001).

[3] Ehlke M, Ramm H, Lamecker H, Hege HC, Zachow S „Fast generation of virtual x-ray images for reconstruction of 3d anatomy", IEEE Transactions on Visualization and Computer Graphics 19, 2673–2682 (2013).

[4] Klima O, Kleparnik P, Spanel M, Zemcik P „Intensity-based femoral atlas 2D/3D registration using Levenberg–Marquardt optimisation"in Medical Imaging: Biomedical Applications in Molecular, Structural, and Functional Imaging, Proc. SPIE, SPIE-The International Society for Optical Engineering (2016).

[5] Aspert N, Santa-cruz D, Ebrahimi T „MESH: Measuring Errors between Surfaces using the Hausdorff distance"in Proc. of IEEE International Conference in Multimedia and Expo 2002.

C

GP-GPU ACCELERATED INTENSITY-BASED 2D/3D REGISTRATION PIPELINE

CITATION

Ondřej Klíma, Petr Klepárník, Michal Španěl, and Pavel Zemčík. GP-GPU accelerated intensity-based 2D/3D registration pipeline. Proceedings of Shape Symposium, pages 19–19. Delemont: Swiss Institute for Computer Aided Surgery, 2015. http://www.shapesymposium.org/ (*extended abstract*)

GP-GPU ACCELERATED INTENSITY-BASED 2D/3D REGISTRATION PIPELINE

Ondrej Klima[1]⋆, Petr Kleparnik[1], Michal Spanel[2], Pavel Zemcik[1],
[1]Brno University of Technology, CZECH REPUBLIC. [2]3Dim Laboratory, Brno, CZECH REPUBLIC.

Background: The possibilities of computer-aided preoperative planning based on plain X-ray images have recently been brought into focus in orthopaedic surgery. One of the main tasks in orthopeadic surgery is the identification of the best shaped bone implant or bone replacement for a specific patient. The essential moment of the planning process is the construction of 3D patient-speficic bone model from a set of X-ray images. The construction is performed using a deformable 2D/3D registration where a statistical shape model is being fitted into a set of calibrated X-ray images. The deformable registration is a time-consuming process, especially in case of intensity-based registration methods. On the other hand, beyond the shape reconstruction, intensity based methods allow modeling bone densities which can be further exploited for FEM simulations.

Aims: In order to speed-up the preoperative planning process, we are working on a pipeline for intensity-based 2D/3D registration fully accelereted using graphics hardware (GP-GPU).

Methods: We have created a statistical shape and intensity model [1], based on a set of CT images of femoral bones and corresponding segmentations. The bone model is represented as a tetrahedral mesh (see Figure 1 left); the bone density is described in each tetrahedron using Bernstein polynomials of a certain degree. Using this representation it is possible to model anatomical structures such as a compact and spongy bone that are observable in X-ray images of femora. The CT data sets were obtained from anonymized clinical cases and from `Virtual Skeleton Database`. Registration of CT images was performed using the `Elastix` software.

Before the registration is performed, the input X-ray images of patient's femur must be calibrated and roughly segmented by the user. Once a rough position of the shape model is initialized interactively by the user, the registration is performed as an optimization of parameters and position of constructed shape model. In each iteration of the optimization, digitally reconstructed radiographs are rendered from the SSIM. Rendering is performed according to [2] in graphics hardware, using low-level GLSL implementation. The similarity between rendered DRRs and original X-ray images is evaluated using the mutual information metric. Consequently, the SSIM position and parameters are adjusted for the next iteration. The patient-specific model is found when the differences between original X-ray images and DRRs are minimized.

For evaluation of the registration pipeline, two data sets have been created. The first data set contains virtual X-rays rendered from CT images with and without tissues surrounding femoral bones. The second data set comprises from the real X-ray images of a leg phantom.

Results: Figure 1 middle shows DRRs rendered from instaces of the constructed SSIM. The instances were created by varying the first principal components of the shape and intensity models.

Rendering of DRRs from a bone model consisting of 65 thousand vertices and 104 thousand tetrahedra with density described by Bernsterin polynomials of the 3^{rd} degree is performed with framerate 87 FPS on average on `NVIDIA GeForce GTX460` graphics card.

Figure 1 right contains a bone model reconstructed from two calibrated virtual X-ray images. The mean Euclidean distance between the reconstructed and ground-truth bone model surfaces was 0.69 mm, the maximum distance between surfaces was 2.86 mm.

Conclusions: We have proposed a framework for the accelerated multiview intensity-based 2D/3D registration. The whole registration is performed in graphics hardware (GP-GPU), benefiting from the computation locality and parallel implementations of chosen methods. Certain parts of the pipeline implementation will be released as open-source software. Following work will be focused on the extensive evaluation of the pipeline.

Acknowledgments: The authors thank the University Hospital in Ostrava for providing CT images of femoral bones. This work is supported by the Technology Agency of the Czech Republic (TA CR, Project Id: TA04011606).

References:

[1] J. Yao, R. Taylor, "Construction and simplification of bone density models" *SPIE Medical Imaging*: 2001.

[2] M. Ehlke, H Ramm, H. Lamecker, H.C. Hege, S. Zachow. "Fast generation of virtual X-ray images for reconstruction of 3D anatomy." *IEEE Trans Vis Comput Graph*: Dec 2013.

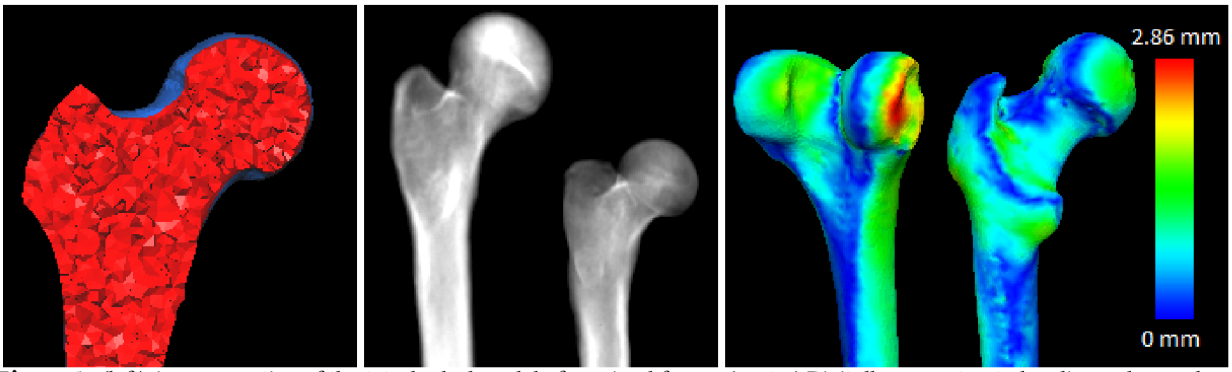

Figure 1: *(left) A cross-section of the tetrahedral model of proximal femur. (center) Digitally reconstructed radiographs rendered from instances of the shape and intensity model. The value of the first principal components of the left and right bone corresponds to 2σ and -2σ respectively. (right) A bone model reconstructed from two calibrated virtual X-ray images. The reconstruction accuracy is visualised using a heat map.*

Part V

SUPPLEMENTARY MATERIALS

The following part describes technical details on calibration box, markers, Plexiglass phantom, and statistical shape and intensity models involved in the studies. The technical drawings were kindly digitized and rendered by Adéla Hýlová, and the bone implants were generously scanned and visualized by Aleš Mizera and Pavel Stoklásek.

D

BIPLANAR CALIBRATION BOX

As the costs of commercially available calibration boxes range from €2,434 to €13,500, a custom biplanar cage was constructed using an extruded Plexiglass and tantalum beads from X-medics Scandinavia[1] provider for involvement in studies [KNM+18, KMŠ+18]. Figures D.1 and D.2 present technical drawings of the box, Figure D.3 shows its visualisation. Table D.1 contains coordinates of individual beads within the box.

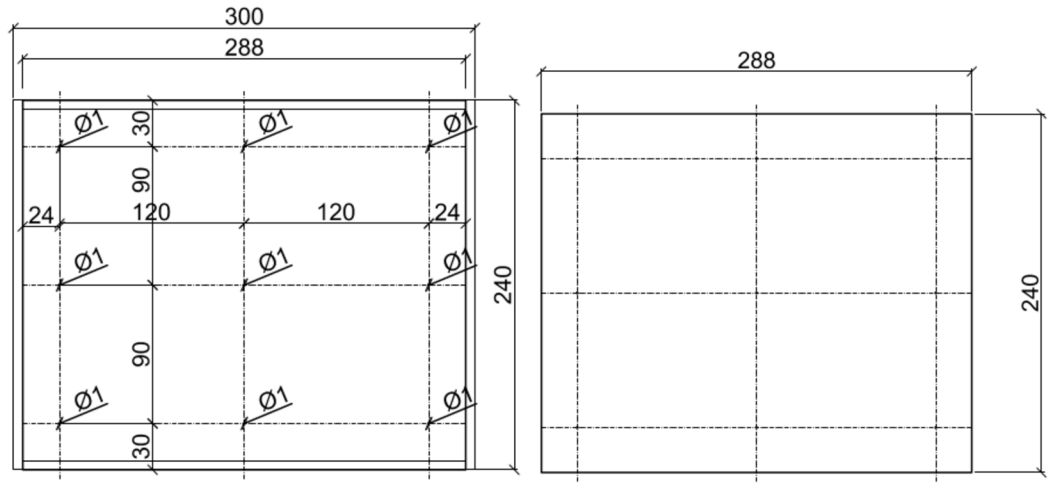

Figure D.1: Dimensions of the fiducial planes.

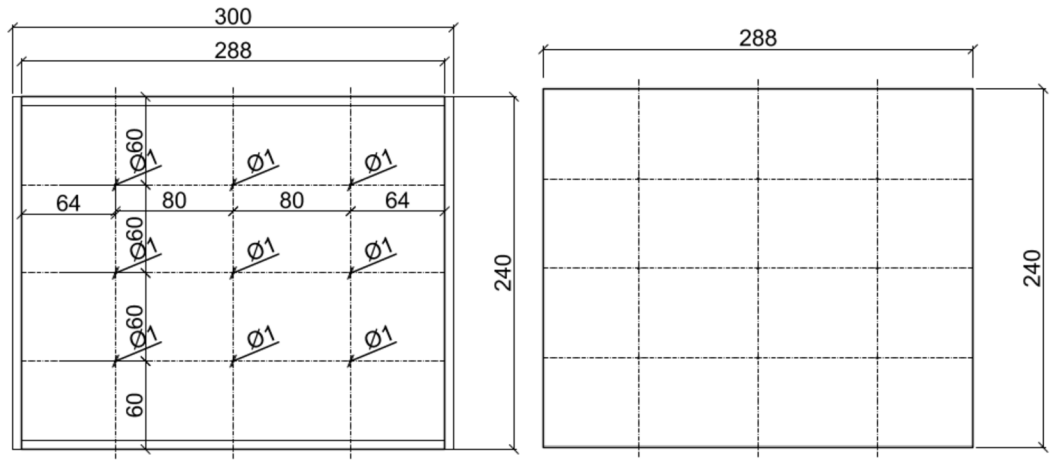

Figure D.2: Dimensions of the control planes.

[1] https://x-medics.com/

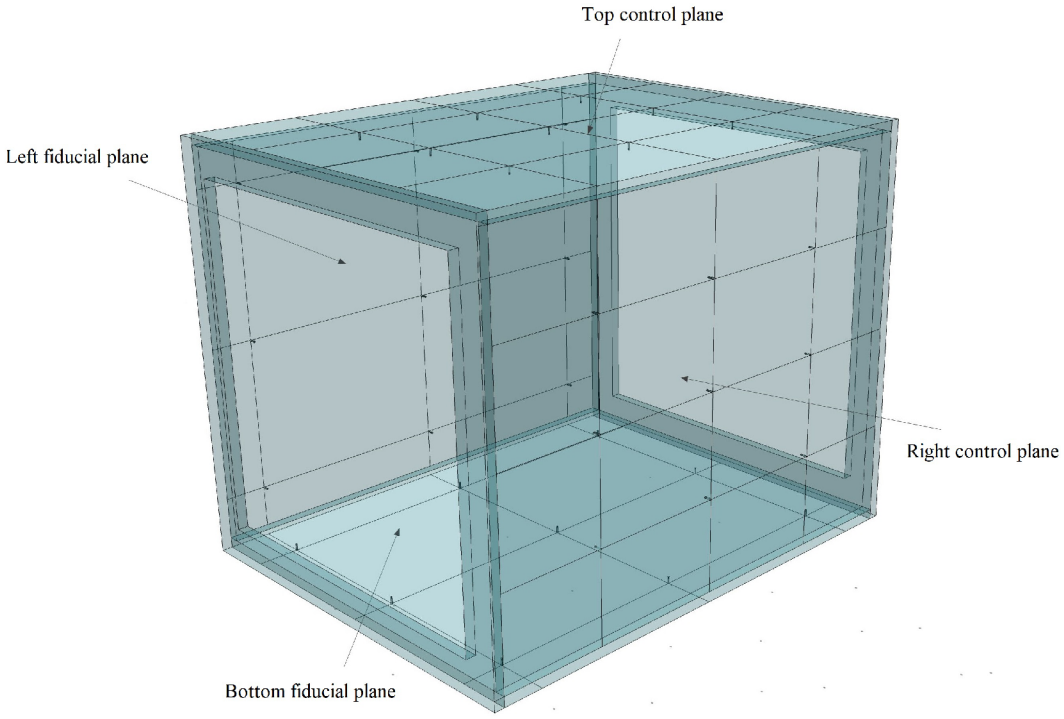

Figure D.3: Visualisation of the constructed calibration box.

Table D.1: Poses of tantalum beads within the calibration box.

	Anterior-posterior view						Lateral view					
	Control plane			Fiducial plane			Control plane			Fiducial plane		
	x	y	z	x	y	z	x	y	z	x	y	z
1	-90	120	0	-60	80	233	- 116.5	120	206.5	116.5	80	176.5
2	0	120	0	0	80	233	-116.5	120	116.5	116.5	80	116.5
3	90	120	0	60	80	233	-116.5	120	26.5	116.5	80	56.5
4	-90	0	0	-60	0	233	-116.5	0	206.5	116.5	0	176.5
5	0	0	0	0	0	233	-116.5	0	116.5	116.5	0	116.5
6	90	0	0	60	0	233	-116.5	0	26.5	116.5	0	56.5
7	-90	-120	0	-60	-80	233	-116.5	-120	206.5	116.5	-80	176.5
8	0	-120	0	0	-80	233	-116.5	-120	116.5	116.5	-80	116.5
9	90	-120	0	60	-80	233	-116.5	-120	26.5	116.5	-80	56.5

E

PROSTHESIS PHANTOM ASSEMBLY

The recover a ground-truth pose of the femoral stem [KNM+18], the implant was attached to a custom made Plexiglass phantom equipped with tantalum beads at known positions. Technical drawings of the phantom are shown in Figure E.1, visualisation of the phantom is illustrated in Figure E.2. Figure E.3 describes the attachement of the stem to the phantom box.

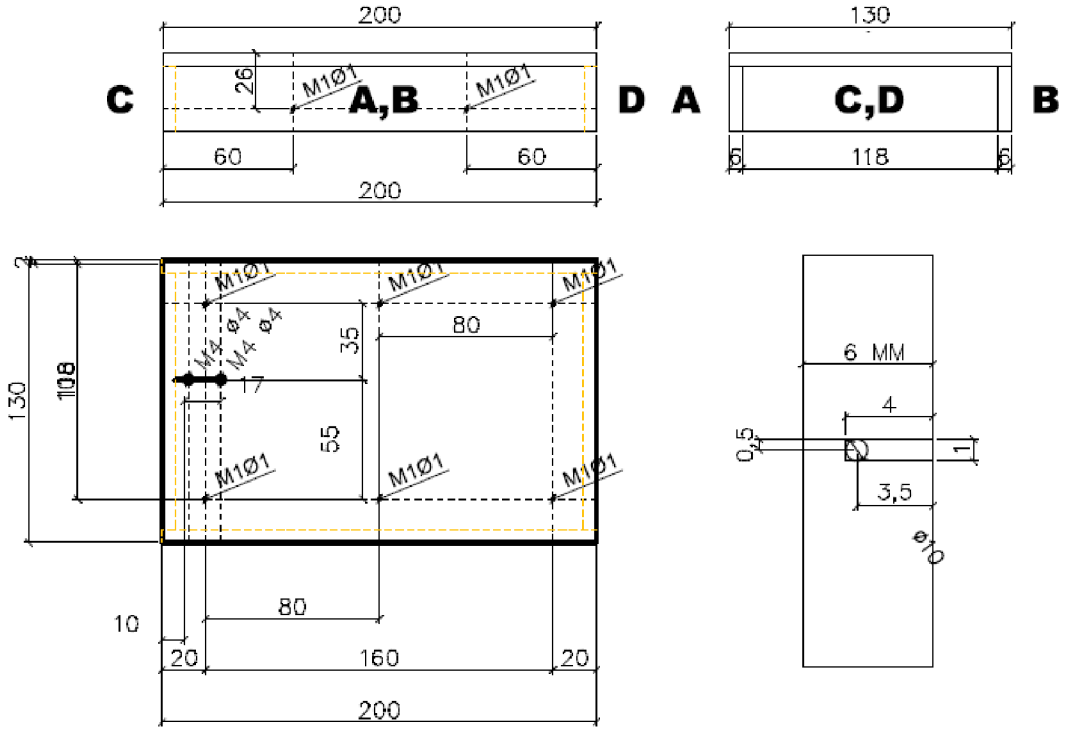

Figure E.1: Technical drawings describing dimensions of the phantom and placement of the tantalum beads.

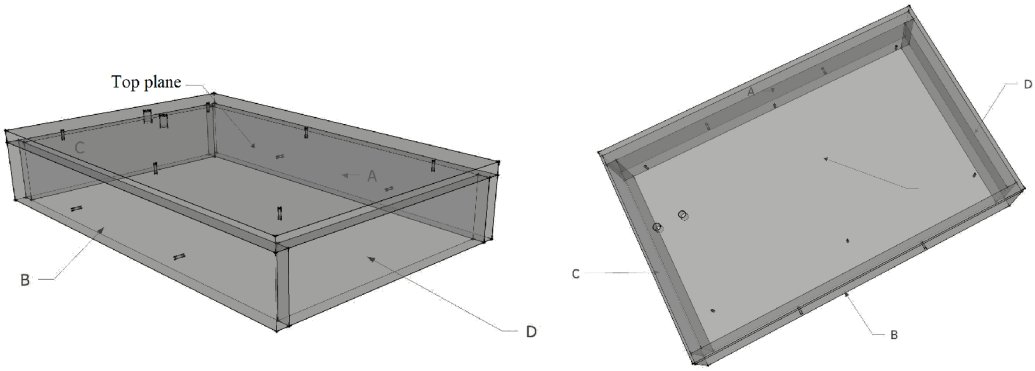

Figure E.2: Visualisations of the Plexiglass phantom.

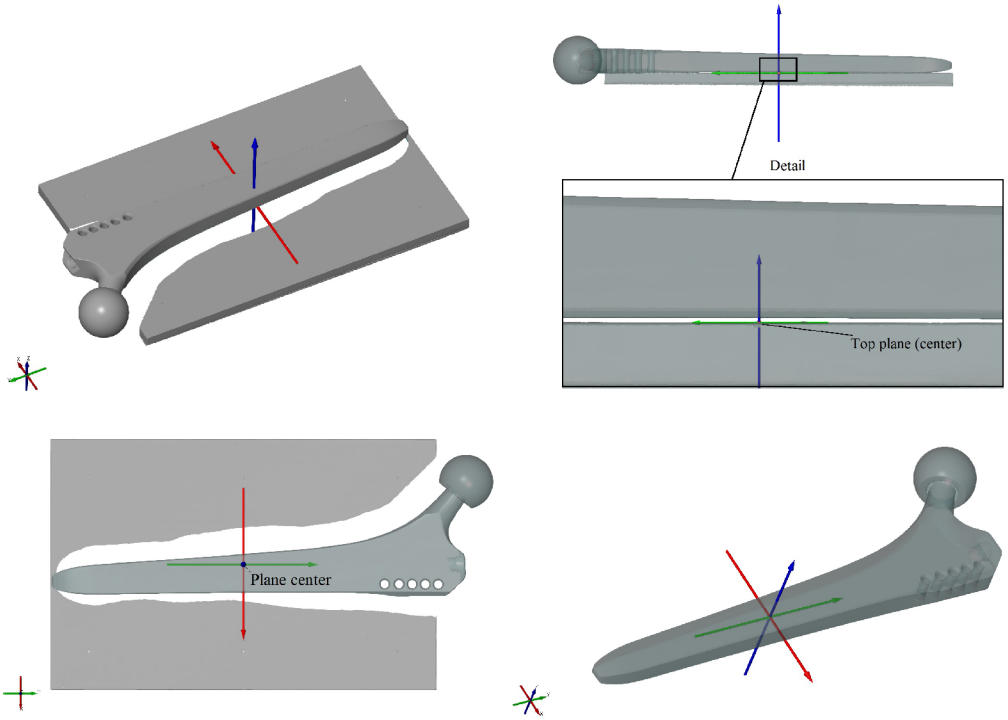

Figure E.3: Attachement of the femoral stem to the Plexiglass phantom.

F

PREOPERATIVE PLANNING CALIBRATION MARKERS

For the calibration of radiographs in real user scenarios, experimental markers shown in Figure F.1 were constructed by Tescan 3DIM[1]company. Usage of the markers and corresponding radiographs, involved in [KKŠZ16a], are illustrated in Figures F.3 and F.2.

Figure F.1: Experimental calibration markers constructed by Tescan 3Dim company.

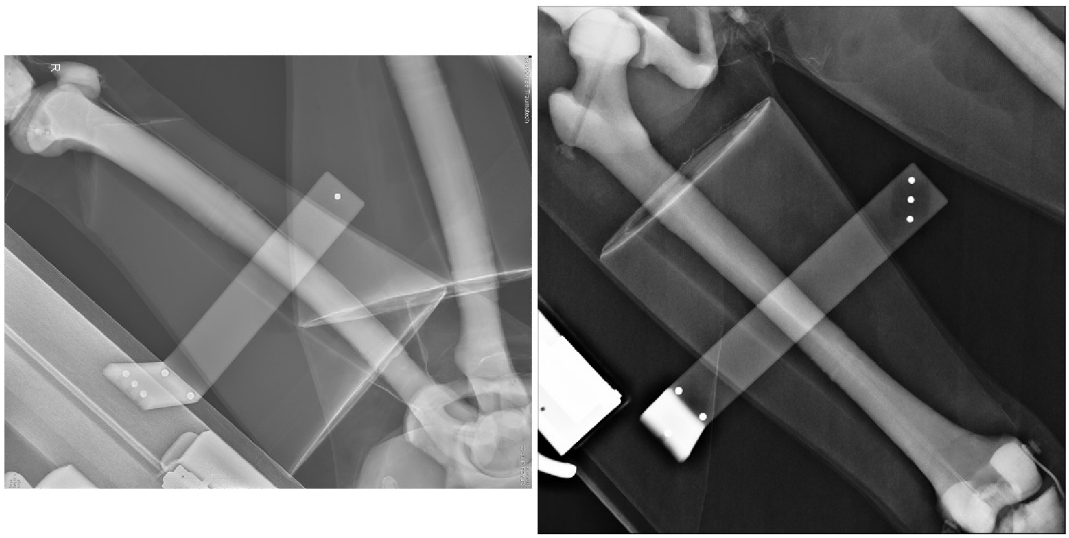

Figure F.2: Radiographs captured using L-shaped calibration marker shown in Figure F.1 *(left)*.

[1] https://www.tescan3dim.com/

Figure F.3: Capturing anterior-posterior and lateral radiographs of the dummy with calibration marker shown in Figure F.1 *(right)* firmly attached to the limb vacuum splint.

G

STATISTICAL SHAPE AND INTENSITY MODELS

Within the scope of the thesis and the preoperative planning application, four statistical shape and intensity models [132] were constructed following a procedure described in [KKŠZ16a]. The computed tomography images used for shape models construction were provided by University Hospital in Ostrava. The reference tetrahedral models were created using Delaunay triangulation [109] from polygonal models with 10,000 faces.

G.1 LOWER LIMBS

Statistical shape models of femur and tibia are shown in Figures G.1 and G.2, details of the models are presented in Table G.1.

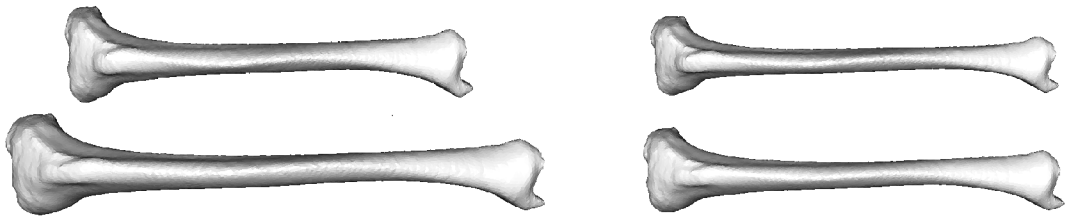

$b_1 = \pm 2\sigma$ $b_2 = \pm 2\sigma$

Figure G.1: Statistical shape model of tibia. The instances were generated by setting the first *(left)* and the second *(right)* parameter to $\pm 2\sigma$. The rest of the shape modes were set to zero.

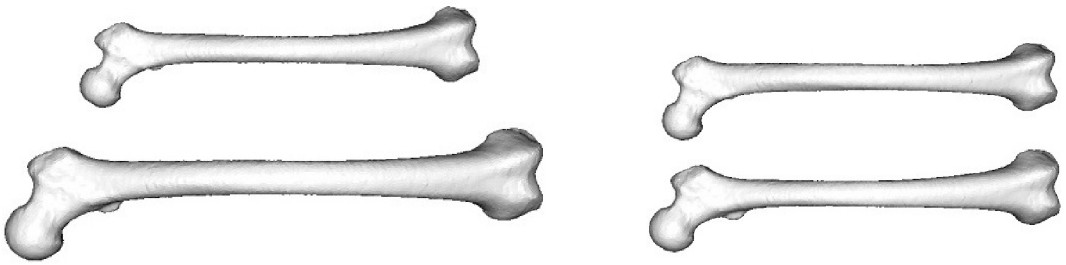

$b_1 = \pm 2\sigma$ $b_2 = \pm 2\sigma$

Figure G.2: Statistical shape model of femur.

Table G.1: Characteristics of involved statistical shape models of lower limbs.

Statistical shape model	Size of training set	Modes of variation	Tetrahedral vertices	Tetrahedra
Femur	43 bones	41	20,843	93,480
Tibia	42 bones	40	22,003	106,436

G.2 UPPER LIMBS

Figures G.3 and G.4 show constructed shape and intensity models of femur and tibia. Further characteristics of the models are described in Table G.2.

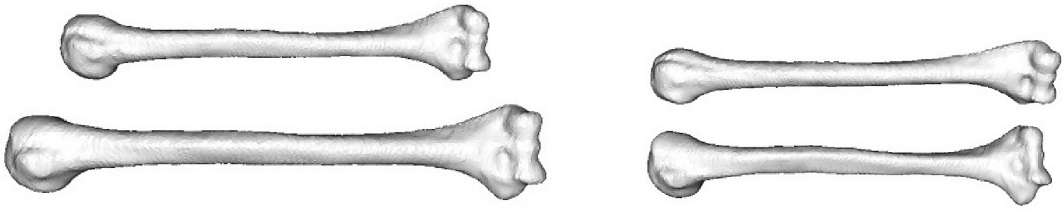

$b_1 = \pm 2\sigma$ $b_2 = \pm 2\sigma$

Figure G.3: Statistical shape model of humerus.

$b_1 = \pm 2\sigma$ $b_2 = \pm 2\sigma$

Figure G.4: Statistical shape model of radius.

Table G.2: Characteristics of statistical shape models of upper limbs.

Statistical shape model	Size of training set	Modes of variation	Tetrahedral vertices	Tetrahedra
Humerus	30 bones	28	20,003	106,436
Radius	21 bones	40	21,253	101,800

BIBLIOGRAPHY

[1] iJoint: 2D/3D reconstruction of patient-specific hip joint from conventional X-ray radiographs. Institute for Surgical Technology & Biomechanics, Universität Bern.

[2] iLeg: 2D/3D reconstruction of lower extremity from clinically available X-rays. Institute for Surgical Technology & Biomechanics, Universität Bern.

[3] *Principal Component Analysis*. Springer-Verlag, 2002. doi: 10.1007/b98835. URL https://doi.org/10.1007/b98835.

[4] YI Abdel-Aziz, HM Karara, and M Hauck. Direct linear transformation from comparator coordinates into object space coordinates in close-range photogrammetry. *Proceedings of the Symposium on Close-Range photogrammetry*, pages 1 – 18, 1971.

[5] Gunnar Adalberth, Kjell G Nilsson, Johan Kärrholm, and Helen Hassander. Fixation of the tibial component using CMW-1 or palacos bone cement with gentamicin: Similar outcome in a randomized radiostereometric study of 51 total knee arthroplasties. *Acta Orthopaedica Scandinavica*, 73(5):531–538, January 2002. doi: 10.1080/00016470232102280 2. URL https://doi.org/10.1080/00016470232102280 2.

[6] Thomas Albrecht and Thomas Vetter. Automatic Fracture Reduction. In Joshua A. Levine, Rasmus R. Paulsen, and Yongjie Zhang, editors, *Mesh Processing in Medical Image Analysis 2012*, pages 22–29, Berlin, Heidelberg, 2012. Springer Berlin Heidelberg. ISBN 978-3-642-33463-4.

[7] Ovidiu Alexa, Bogdan Veliceasa, Bogdan Puha, and Diana Cimpoesu. Digital templating in surgical treatment of trochanteric fractures. In *2013 E-Health and Bioengineering Conference (EHB)*, pages 1–4, 2013. doi: 10.1109/EHB.2013.6707381.

[8] Per O. Almquist, Arnbjörn Arnbjörnsson, Rose Zätterström, Leif Ryd, Charlotte Ekdahl, and Thomas Fridén. Evaluation of an external device measuring knee joint rotation: an in vivo study with simultaneous roentgen stereometric analysis. *Journal of Orthopaedic Research*, 20(3):427–432, May 2002. doi: 10.1016/s0736-0266(01)00148-6. URL https://doi.org/10.1016/s0736-0266(01)00148-6.

[9] Amro Alnahhal, Nayef Aslam-Pervez, and Hassaan Q. Sheikh. Templating hip arthroplasty. *Open Access Macedonian Journal of Medical Sciences*, 7(4):672–685, February 2019. doi: 10.3889/oamjms.2019.088. URL https://doi.org/10.3889/oamjms.2019.088.

[10] N. Aspert, D. Santa-Cruz, and T. Ebrahimi. Mesh: measuring errors between surfaces using the hausdorff distance. In *Multimedia and Expo, 2002. ICME '02. Proceedings. 2002 IEEE International Conference on*, volume 1, pages 705–708, 2002.

[11] N. Baka, B.L. Kaptein, M. de Bruijne, T. van Walsum, J.E. Giphart, W.J. Niessen, and B.P.F. Lelieveldt. 2d-3d shape reconstruction of the distal femur from stereo x-ray imaging using statistical shape models. *Medical Image Analysis*, 15:840 – 850, 2011.

[12] N. Baka, M. de Bruijne, T. van Walsum, B. L. Kaptein, J. E. Giphart, M. Schaap, W. J. Niessen, and B. P. F. Lelieveldt. Statistical Shape Model-Based Femur Kinematics From Biplane Fluoroscopy. *IEEE Transactions on Medical Imaging*, 31 (8):1573–1583, Aug 2012. ISSN 0278-0062.

[13] Nora Baka, Bart L. Kaptein, J. Erik Giphart, Marius Staring, Marleen de Bruijne, Boudewijn P.F. Lelieveldt, and Edward Valstar. Evaluation of automated statistical shape model based knee kinematics from biplane fluoroscopy. *Journal of Biomechanics*, 47(1):122 – 129, 2014. ISSN 0021-9290.

[14] P.J. Besl and Neil D. McKay. A method for registration of 3-d shapes. *IEEE Transactions on Pattern Analysis and Machine Intelligence*, 14(2):239–256, February 1992. doi: 10.1109/34.121791. URL https://doi.org/10.1109/34.121791.

[15] Hans-Georg Beyer and Bernhard Sendhoff. *Covariance Matrix Adaptation Revisited – The CMSA Evolution Strategy –*, pages 123–132. Berlin, Heidelberg, 2008. ISBN 978-3-540-87700-4. doi: 10.1007/978-3-540-87700-4_13.

[16] Christopher M. Bishop. *Pattern Recognition and Machine Learning (Information Science and Statistics)*. Springer-Verlag New York, Inc., Secaucus, NJ, USA, 2006.

[17] Christoph K. Boese, Jan Bredow, Jens Dargel, Peer Eysel, Hansjörg Geiges, and Philipp Lechler. Calibration marker position in digital templating of total hip arthroplasty. *The Journal of Arthroplasty*, 31(4):883–887, April 2016. doi: 10.1016/j.arth.2015.10.009. URL https://doi.org/10.1016/j.arth.2015.10.009.

[18] Christoph Kolja Boese, Philipp Lechler, Leonard Rose, Jens Dargel, Johannes Oppermann, Peer Eysel, Hansjörg Geiges, and Jan Bredow. Calibration markers for digital templating in total hip arthroplasty. *PLOS ONE*, 10(7):e0128529,

July 2015. doi: 10.1371/journal.pone.0128529. URL https://doi.org/10.1371/journal.pone.0128529.

[19] Sveinbjörn Brandsson, Jon Karlsson, Leif Swärd, Jüri Kartus, Bengt I. Eriksson, and Johan Kärrholm. Kinematics and laxity of the knee joint after anterior cruciate ligament reconstruction. *The American Journal of Sports Medicine*, 30 (3):361–367, May 2002. doi: 10.1177/03635465020300031001. URL https://doi.org/10.1177/03635465020300031001.

[20] Bart Ten Brinke, Annechien Beumer, Koen L M Koenraadt, Denise Eygendaal, Gerald A Kraan, and Nina M C Mathijssen. The accuracy and precision of radiostereometric analysis in upper limb arthroplasty. *Acta Orthopaedica*, 88(3): 320–325, March 2017. doi: 10.1080/17453674.2017.1291872. URL https://doi.org/10.1080/17453674.2017.1291872.

[21] Hsin-Jui Chen, Shanq-Jang Ruan, Sha-Wo Huang, and Yan-Tsung Peng. Lung x-ray segmentation using deep convolutional neural networks on contrast-enhanced binarized images. *Mathematics*, 8(4):545, April 2020. doi: 10.3390/math8040545. URL https://doi.org/10.3390/math8040545.

[22] AMT Choo and TR Oxland. Improved rsa accuracy with dlt and balanced calibration marker distributions with an assessment of initial-calibration. *Journal of Biomechanics*, 36(2):259–264, 2003. ISSN 0021-9290.

[23] Rasmus Christensen, Emil Toft Petersen, Jonathan Jürgens-Lahnstein, Søren Rytter, Lars Lindgren, Sepp De Raedt, Annemarie Brüel, and Maiken Stilling. Assessment of knee kinematics with dynamic radiostereometry: Validation of an automated model-based method of analysis using bone models. *Journal of Orthopaedic Research*, 39(3):597–608, October 2020. doi: 10.1002/jor.24875. URL https://doi.org/10.1002/jor.24875.

[24] T.F. Cootes, D.H. Cooper, C.J. Taylor, and J. Graham. A trainable method of parametric shape description. *Image and Vision Computing*, pages 289–294, 1992.

[25] Owain Critchley, Stuart Callary, Graham Mercer, David Campbell, and Christopher Wilson. Long-term migration characteristics of the corail hydroxyapatite-coated femoral stem: a 14-year radiostereometric analysis follow-up study. *Archives of Orthopaedic and Trauma Surgery*, 140(1):121–127, October 2019. doi: 10.1007/s00402-019-03291-8. URL https://doi.org/10.1007/s00402-019-03291-8.

[26] Martin Čuta and Tomáš Mořkovský. Antropologické zhodnocení kosterních pozůstatků ze slavkovské šibenice u křenovic. *Anthropologia integra*, 8(2):15–

24, December 2017. doi: 10.5817/ai2017-2-15. URL https://doi.org/10.5817/ai2017-2-15.

[27] T. De Silva, A. Uneri, M. Ketcha, S. Reaungamornrat, J. Goerres, S. Vogt, G. Kleinszig, J.-P. Wolinsky, and J. Siewerdsen. "levelcheck" localization of spinal vertebrae in intraoperative radiographs from preoperative mri. In *Proc. of CARS*, pages S54–S55. Springer, 2016.

[28] I. L. Dryden and K. V. Mardia. *Statistical Shape Analysis*. Wiley, Chichester, 1998.

[29] Richard O. Duda and Peter E. Hart. Use of the hough transformation to detect lines and curves in pictures. *Communications of the ACM*, 15(1):11–15, January 1972. doi: 10.1145/361237.361242. URL https://doi.org/10.1145/361237.361242.

[30] J. Dworzak, H. Lamecker, J. von Berg, T. Klinder, C. Lorenz, D. Kainmuller, H. Seim, H.-C. Hege, and S. Zachow. 3d reconstruction of the human rib cage from 2d projection images using a statistical shape model. *International Journal Computer Assisted Radiology and Surgery*, 5(2):111–124, 2010.

[31] Karen Dyreborg, Mikkel R Andersen, Nikolaj Winther, Søren Solgaard, Gunnar Flivik, and Michael M Petersen. Migration of the uncemented echo bi-metric and bi-metric THA stems: a randomized controlled RSA study involving 62 patients with 24-month follow-up. *Acta Orthopaedica*, 91(6):693–698, August 2020. doi: 10.1080/17453674.2020.1802682. URL https://doi.org/10.1080/17453674.2020.1802682.

[32] M. Ehlke, H. Ramm, H. Lamecker, H.-C. Hege, and S. Zachow. Fast generation of virtual x-ray images for reconstruction of 3d anatomy. *IEEE Transactions on Visualization and Computer Graphics*, 19:2673–2682, 2013.

[33] Braden C Fleming, Glenn D Peura, Joseph A Abate, and Bruce D Beynnon. Accuracy and repeatability of roentgen stereophotogrammetric analysis (RSA) for measuring knee laxity in longitudinal studies. *Journal of Biomechanics*, 34 (10):1355–1359, October 2001. doi: 10.1016/s0021-9290(01)00087-2. URL https://doi.org/10.1016/s0021-9290(01)00087-2.

[34] Y. Fukuoka, A. Hoshino, and A. Ishida. A simple radiographic measurement method for polyethylene wear in total knee arthroplasty. *IEEE Transactions on Rehabilitation Engineering*, 7(2):228–233, June 1999. doi: 10.1109/86.769413. URL https://doi.org/10.1109/86.769413.

[35] R. H. Gong, J. Stewart, and P. Abolmaesumi. Reduction of multi-fragment fractures of the distal radius using atlas-based 2d/3d registration. In *Medical*

Imaging: Visualization, Image-Guided Procedures, and Modeling, volume 7261 of *Proc. SPIE*. SPIE-The International Society for Optical Engineering, 2009.

[36] Ren Hui Gong and Purang Abolmaesumi. 2D/3D registration with the CMA-ES method. In *Medical Imaging*, pages 69181M–69181M. SPIE, 2008.

[37] Ren Hui Gong, James Stewart, and Purang Abolmaesumi. Multiple-object 2-D–3-D registration for noninvasive pose identification of fracture fragments. *IEEE Transactions on Biomedical Engineering*, 58(6):1592–1601, 2011.

[38] Asgeir Gudnason, Gunnar Adalberth, Kjell-Gunnar Nilsson, and Nils P Hailer. Tibial component rotation around the transverse axis measured by radiostereometry predicts aseptic loosening better than maximal total point motion. *Acta Orthopaedica*, 88(3):282–287, March 2017. doi: 10.1080/17453674.2017.1297001. URL https://doi.org/10.1080/17453674.2017.1297001.

[39] L. Hansen, S. De Raedt, P. B. Jørgensen, B. Mygind-Klavsen, B. Kaptein, and M. Stilling. Marker free model-based radiostereometric analysis for evaluation of hip joint kinematics. *Bone & Joint Research*, 7(6):379–387, June 2018. doi: 10.1302/2046-3758.76.bjr-2017-0268.r1. URL https://doi.org/10.1302/2046-3758.76.bjr-2017-0268.r1.

[40] Lars Hansen, Sepp de Raedt, Peter Bo Jørgensen, Bjarne Mygind-Klavsen, Bart Kaptein, and Maiken Stilling. Dynamic radiostereometric analysis for evaluation of hip joint pathomechanics. *Journal of Experimental Orthopaedics*, 4(1), June 2017. doi: 10.1186/s40634-017-0096-2. URL https://doi.org/10.1186/s40634-017-0096-2.

[41] N. Hansen. The cma evolution strategy: A comparing review. In *Towards a New Evolutionary Computation*, volume 192 of *Studies in Fuzziness and Soft Computing*, pages 75–102. Springer Berlin Heidelberg, 2006.

[42] N. Hansen and S. Kern. Evaluating the cma evolution strategy on multimodal test functions. *Parallel Problem Solving from Nature - PPSN VIII*, pages 282–291, 2004.

[43] Ulrik Hansson, Leif Ryd, and Sören Toksvig-Larsen. A randomised RSA study of peri-apatite™ HA coating of a total knee prosthesis. *The Knee*, 15(3):211–216, June 2008. doi: 10.1016/j.knee.2008.01.013. URL https://doi.org/10.1016/j.knee.2008.01.013.

[44] Richard Hartley and Andrew Zisserman. *Multiple View Geometry in Computer Vision*. Cambridge University Press, USA, 2 edition, 2003. ISBN 0521540518.

[45] Maria Hilding and Per Aspenberg. Local peroperative treatment with a bisphosphonate improves the fixation of total knee prostheses: A randomized, double-blind radiostereometric study of 50 patients. *Acta Orthopaedica*, 78(6):795–799, January 2007. doi: 10.1080/17453670710014572. URL https://doi.org/10.1080/17453670710014572.

[46] Hagen Hommel, Alper Akcoltekin, Benedikt Thelen, Jan Stifter, Tobias Schw\"agli, and Guoyan Zheng. 3xplan: A novel technology for 3d prosthesis planning using 2d x-ray radiographs. In Klaus Radermacher and Ferdinando Rodriguez Y Baena, editors, *CAOS 2017. 17th Annual Meeting of the International Society for Computer Assisted Orthopaedic Surgery*, volume 1 of *EPiC Series in Health Sciences*, pages 93–95. EasyChair, 2017. doi: 10.29007/s2sn. URL https://easychair.org/publications/paper/fQ.

[47] D.W.J. Howcroft, M.J. Fehily, C. Peck, A. Fox, B. Dillon, and D.S. Johnson. The role of preoperative templating in total knee arthroplasty: Comparison of three prostheses. *The Knee*, 13(6):427–429, December 2006. doi: 10.1016/j.knee.2006.05.002. URL https://doi.org/10.1016/j.knee.2006.05.002.

[48] A. Hurvitz and L. Joskowicz. Registration of a ct-like atlas to fluoroscopic x-ray images using intensity correspondences. *International Journal of Computer Assisted Radiology and Surgery*, 3:493–504, 2008.

[49] Christian Igel, Verena Heidrich-Meisner, and Tobias Glasmachers. Shark. *Journal of Machine Learning Research*, 9:993–996, 2008.

[50] Renjit Thomas Issac, Hitesh Gopalan, Mathew Abraham, Cherian John, Sujith Mathew Issac, and Diju Jacob. Preoperative determination of tibial nail length: An anthropometric study. *Chinese Journal of Traumatology*, 19(3):151 – 155, 2016. ISSN 1008-1275.

[51] Anne Jacobsen, Frank Seehaus, Yutong Hong, Han Cao, Alexander Schuh, Raimund Forst, and Stefan Sesselmann. Model-based roentgen stereophotogrammetric analysis using elementary geometrical shape models: 10 years results of an uncemented acetabular cup component. *BMC Musculoskeletal Disorders*, 19(1), September 2018. doi: 10.1186/s12891-018-2259-4. URL https://doi.org/10.1186/s12891-018-2259-4.

[52] J. Jan. *Medical Image Processing, Reconstruction and Restoration - Concepts and Methods*. CRC Press, Taylor and Francis Group, Boca Raton, FL, USA, 2006.

[53] Juan J. Jiménez-Delgado, Félix Paulano-Godino, Rubén PulidoRam-Ramírez, and J. Roberto Jiménez-Pérez. Computer assisted preoperative planning of

bone fracture reduction: Simulation techniques and new trends. *Medical Image Analysis*, 30:30 – 45, 2016. ISSN 1361-8415.

[54] B L Kaptein, E R Valstar, B C Stoel, P M Rozing, and J H C Reiber. Evaluation of three pose estimation algorithms for model-based roentgen stereophotogrammetric analysis. *Proceedings of the Institution of Mechanical Engineers, Part H: Journal of Engineering in Medicine*, 218(4):231–238, April 2004. doi: 10.1243/0954411041561036. URL https://doi.org/10.1243/0954411041561036.

[55] Bart L Kaptein, Edward R Valstar, Cees W Spoor, Berend C Stoel, and Piet M Rozing. Model-based RSA of a femoral hip stem using surface and geometrical shape models. *Clinical Orthopaedics and Related Research*, 448:92–97, July 2006. doi: 10.1097/01.blo.0000224010.04551.14. URL https://doi.org/10.1097/01.blo.0000224010.04551.14.

[56] BL Kaptein, ER Valstar, BC Stoel, PM Rozing, and JHC Reiber. A new model-based rsa method validated using cad models and models from reversed engineering. *Journal of Biomechanics*, 36(6):873–882, 2003.

[57] BL Kaptein, ER Valstar, CW Spoor, BC Stoel, and PM Rozing. Model-based rsa of a femoral hip stem using surface and geometrical shape models. *Clinical orthopeadics and related research*, (448):92–97, 2006.

[58] J. Karrholm, S. Brandsson, and M. A. R. Freeman. Tibiofemoral movement 4: changes of axial tibial rotation caused by forced rotation at the weight-bearing knee studied by RSA. *The Journal of Bone and Joint Surgery. British volume*, 82-B(8):1201–1203, November 2000. doi: 10.1302/0301-620x.82b8.0821201. URL https://doi.org/10.1302/0301-620x.82b8.0821201.

[59] C. T. Kelley. *Iterative methods for optimization*. Frontiers in applied mathematics. SIAM, Philadelphia, 1999. ISBN 0-89871-433-8. URL http://opac.inria.fr/record=b1096699.

[60] M. D. Ketcha, T. De Silva, A. Uneri, G. Kleinszig, S. Vogt, J.-P. Wolinsky, and J. H. Siewerdsen. Automatic masking for robust 3d-2d image registration in image-guided spine surgery, 2016.

[61] Siavash Khallaghi, Parvin Mousavi, Ren Hui Gong, Sean Gill, Jonathan Boisvert, Gabor Fichtinger, David Pichora, Dan Borschneck, and Purang Abolmaesumi. Registration of a statistical shape model of the lumbar spine to 3d ultrasound images. In *MICCAI 2010*, pages 68–75. 2010.

[62] Davis E. King. Dlib-ml: A machine learning toolkit. *Journal of Machine Learning Research*, 10:1755–1758, 2009.

[63] M. Kistler, S. Bonaretti, M. Pfahrer, R. Niklaus, and P. B?chler. The virtual skeleton database: An open access repository for biomedical research and collaboration. *Journal of Medical Internet Research*, 2013.

[64] Stefan Klein, M. Staring, Keelin Murphy, M.A. Viergever, and J. P W Pluim. Elastix: A toolbox for intensity-based medical image registration. *IEEE Transactions on Medical Imaging*, 29(1):196–205, 2010.

[65] K Kobayashi, M Sakamoto, Y Tanabe, A Ariumi, T Sato, G Omori, and Y Koga. Automated image registration for assessing three-dimensional alignment of entire lower extremity and implant position using bi-plane radiography. *Journal of Biomechanics*, 42(16):2818–2822, 2009.

[66] Philippe Kopylov, Per Aspenberg, Xunhua Yuan, and Leif Ryd. Radiostereometric analysis of distal radial fracture displacement during treatment: A randomized study comparing norian SRS and external fixation in 23 patients. *Acta Orthopaedica Scandinavica*, 72(1):57–61, January 2001. doi: 10.1080/000164701753606707. URL https://doi.org/10.1080/000164701753606707.

[67] Y. Kosashvili, N. Shasha, E. Olschewski, O. Safir, L. White, A. Gross, and D. Backstein. Digital versus conventional templating techniques in preoperative planning for total hip arthroplasty. *Can J Surg*, 52(1):6–11, Feb 2009.

[68] H. Lamecker, T.H. Wenckebach, and H.-C. Hege. Atlas-based 3d-shape reconstruction from x-ray images. In *18th International Conference on Pattern Recognition*, volume 1, pages 371–374. ICPR, 2006.

[69] Haofu Liao, Wei-An Lin, Jiarui Zhang, Jingdan Zhang, Jiebo Luo, and S. Kevin Zhou. Multiview 2d/3d rigid registration via a point-of-interest network for tracking and triangulation. In *Proceedings of the IEEE/CVF Conference on Computer Vision and Pattern Recognition (CVPR)*, June 2019.

[70] Rui Liao, Shun Miao, Pierre de Tournemire, Sasa Grbic, Ali Kamen, Tommaso Mansi, and Dorin Comaniciu. An artificial agent for robust image registration. In *Proceedings of the Thirty-First AAAI Conference on Artificial Intelligence*, AAAI'17, page 4168–4175. AAAI Press, 2017.

[71] William E. Lorensen and Harvey E. Cline. Marching cubes: A high resolution 3d surface construction algorithm. *ACM SIGGRAPH Computer Graphics*, 21(4): 163–169, August 1987. doi: 10.1145/37402.37422. URL https://doi.org/10.1145/37402.37422.

[72] M. Luthi, R. Blanc, T. Albrecht, T. Gass, O. Goksel, P. Büchler, M. Kistler, H. Bousleiman, M. Reyes, P. Cattin, and T. Vetter. Statismo – a framework for PCA based statistical models. 7 2012.

[73] M.R. Mahfouz, W.A. Hoff, R.D. Komistek, and D.A. Dennis. A robust method for registration of three-dimensional knee implant models to two-dimensional fluoroscopy images. *IEEE Transactions on Medical Imaging*, 22(12):1561–1574, December 2003. doi: 10.1109/tmi.2003.820027. URL https://doi.org/10.1109/tmi.2003.820027.

[74] MR Mahfouz, WA Hoff, RD Komistek, and DA Dennis. Effect of segmentation errors on 3d-to-2d registration of implant models in x-ray images. *Journal of Biomechanics*, 38:229–239, 2005.

[75] Ahmed Nageeb Mahmoud, Uldis Kesteris, and Gunnar Flivik. Stable migration pattern of an ultra-short anatomical uncemented hip stem: A prospective study with 2 years radiostereometric analysis follow-up. *HIP International*, 27(3):259–266, April 2017. doi: 10.5301/hipint.5000458. URL https://doi.org/10.5301/hipint.5000458.

[76] P. Markelj, D. Tomaževič, B. Likar, and F. Pernuš. A review of 3D/2D registration methods for image-guided interventions. *Medical Image Analysis*, 16(3): 642 – 661, 2012. ISSN 1361-8415. Computer Assisted Interventions.

[77] Inger Mechlenburg, Thomas M. Klebe, Kaj V. Døssing, Anders Amstrup, Kjeld Søballe, and Maiken Stilling. Evaluation of periprosthetic bone mineral density and postoperative migration of humeral head resurfacing implants: two-year results of a randomized controlled clinical trial. *Journal of Shoulder and Elbow Surgery*, 23(10):1427–1436, October 2014. doi: 10.1016/j.jse.2014.05.012. URL https://doi.org/10.1016/j.jse.2014.05.012.

[78] Shun Miao, Z. Jane Wang, and Rui Liao. A CNN regression approach for real-time 2d/3d registration. *IEEE Transactions on Medical Imaging*, 35(5):1352–1363, May 2016. doi: 10.1109/tmi.2016.2521800. URL https://doi.org/10.1109/tmi.2016.2521800.

[79] Shun Miao, Sebastien Piat, Peter Walter Fischer, Ahmet Tuysuzoglu, Philip Walter Mewes, Tommaso Mansi, and Rui Liao. Dilated FCN for multi-agent 2d/3d medical image registration. In Sheila A. McIlraith and Kilian Q. Weinberger, editors, *Proceedings of the Thirty-Second AAAI Conference on Artificial Intelligence, (AAAI-18), the 30th innovative Applications of Artificial Intelligence (IAAI-18), and the 8th AAAI Symposium on Educational Advances in Artificial Intelligence (EAAI-18), New Orleans, Louisiana, USA, February 2-7, 2018*, pages 4694–4701. AAAI Press, 2018. URL https://www.aaai.org/ocs/index.php/AAAI/AAAI18/paper/view/16085.

[80] Kenichi Morooka, Masahiko Nakamoto, and Yoshinobu Sato. A survey on statistical modeling and machine learning approaches to computer assisted

medical intervention: Intraoperative anatomy modeling and optimization of interventional procedures. *IEICE TRANSACTIONS on Information and Systems*, pages 784–797, 2013. ISSN 0916-8532.

[81] S. Nazari-Farsani, S. Finnilä, N. Moritz, K. Mattilla, J. Alm, and H. Aro. Is model-based radiostereometric analysis suitable for clinical trials of a cementless tapered wedge femoral stem? *Clinical Orthopaedics and Related Research*, 474: 2246–2253, 2016.

[82] AK Nebergall, K Rader, H Palm, H Malchau, and ME Greene. Precision of radiostereometric analysis (rsa) of acetabular cup stability and polyethylene wear improved by adding tantalum beads to the liner. *Acta Orthopaedica*, 86: 563–568, 2015.

[83] Audrey K. Nebergall, Ola Rolfson, Harry E. Rubash, Henrik Malchau, Anders Troelsen, and Meridith E. Greene. Stable fixation of a cementless, proximally coated, double wedged, double tapered femoral stem in total hip arthroplasty: A 5-year radiostereometric analysis. *The Journal of Arthroplasty*, 31(6):1267–1274, June 2016. doi: 10.1016/j.arth.2015.11.036. URL https://doi.org/10.1016/j.arth.2015.11.036.

[84] Emil Toft Nielsen, Kasper Stentz-Olesen, Sepp de Raedt, Peter Bo Jørgensen, Ole Gade Sørensen, Bart Kaptein, Michael Skipper Andersen, and Maiken Stilling. Influence of the anterolateral ligament on knee laxity: A biomechanical cadaveric study measuring knee kinematics in 6 degrees of freedom using dynamic radiostereometric analysis. *Orthopaedic Journal of Sports Medicine*, 6(8):232596711878969, August 2018. doi: 10.1177/2325967118789699. URL https://doi.org/10.1177/2325967118789699.

[85] David Nuttall, John F. Haines, and Ian I. Trail. A study of the micromovement of pegged and keeled glenoid components compared using radiostereometric analysis. *Journal of Shoulder and Elbow Surgery*, 16(3):S65–S70, May 2007. doi: 10.1016/j.jse.2006.01.015. URL https://doi.org/10.1016/j.jse.2006.01.015.

[86] Yoshito Otake, Matthieu Esnault, Robert Grupp, Shinichi Kosugi, and Yoshinobu Sato. Robust patella motion tracking using intensity-based 2d-3d registration on dynamic bi-plane fluoroscopy: towards quantitative assessment in mpfl reconstruction surgery, 2016.

[87] J. R. T. Pietrzak, F. E. Rowan, B. Kayani, M. J. Donaldson, S. S. Huq, and F. S. Haddad. Preoperative CT-based three-dimensional templating in robot-assisted total knee arthroplasty more accurately predicts implant sizes than

two-dimensional templating. *The Journal of Knee Surgery*, 32(07):642–648, August 2018. doi: 10.1055/s-0038-1666829. URL https://doi.org/10.1055/s-0038-1666829.

[88] Bart G Pijls, José W M Plevier, and Rob G H H Nelissen. RSA migration of total knee replacements. *Acta Orthopaedica*, 89(3):320–328, March 2018. doi: 10.1080/17453674.2018.1443635. URL https://doi.org/10.1080/17453674.2018.1443635.

[89] Stephen M. Pizer, E. Philip Amburn, John D. Austin, Robert Cromartie, Ari Geselowitz, Trey Greer, Bart ter Haar Romeny, John B. Zimmerman, and Karel Zuiderveld. Adaptive histogram equalization and its variations. *Computer Vision, Graphics, and Image Processing*, 39(3):355–368, September 1987. doi: 10.1016/s0734-189x(87)80186-x. URL https://doi.org/10.1016/s0734-189x(87)80186-x.

[90] A.H. Prins, B.L. Kaptein, B.C. Stoel, D.J.P. Lahaye, and E.R. Valstar. Performance of local optimization in single-plane fluoroscopic analysis for total knee arthroplasty. *Journal of Biomechanics*, 48(14):3837–3845, 2015. ISSN 0021-9290. doi: https://doi.org/10.1016/j.jbiomech.2015.09.005. URL https://www.sciencedirect.com/science/article/pii/S0021929015004832.

[91] A.H. Prins, B.L. Kaptein, B.C. Stoel, D.J.P. Lahaye, and E.R. Valstar. Performance of local optimization in single-plane fluoroscopic analysis for total knee arthroplasty. *Journal of Biomechanics*, 48(14):3837–3845, November 2015. doi: 10.1016/j.jbiomech.2015.09.005. URL https://doi.org/10.1016/j.jbiomech.2015.09.005.

[92] Jón I. Ragnarsson and Johan Kärrholm. Stability of femoral neck fracture: Roentgen stereophotogrammetry of 29 hook-pinned fractures. *Acta Orthopaedica Scandinavica*, 62(3):201–207, 1991. doi: 10.3109/17453679108993593.

[93] Hans Rahme, Per Mattsson, Lars Wikblad, Jan Nowak, and Sune Larsson. Stability of cemented in-line pegged glenoid compared with keeled glenoid components in total shoulder arthroplasty. *The Journal of Bone and Joint Surgery-American Volume*, 91(8):1965–1972, August 2009. doi: 10.2106/jbjs.h.00938. URL https://doi.org/10.2106/jbjs.h.00938.

[94] L. Ryd and S. Toksvig-Larsen. Stability of the elevated fragment in tibial plateau fractures. *International Orthopaedics*, 18(3), June 1994. doi: 10.1007/bf00192467. URL https://doi.org/10.1007/bf00192467.

[95] O. Sadowsky, J. D. Cohen, and J. H. Taylor. Rendering tetrahedral meshes with higher-order attenuation functions for digital radiograph reconstruction. In *16th Visualization Conference*, pages 39–46, Minneapolis, 2005. IEEE.

[96] O. Sadowsky, J. D. Cohen, and J. H. Taylor. Projected tetrahedra revisited: A barycentric formulation applied to digital radiograph reconstruction using higher-order attenuation functions. *IEEE Trans. Vis. Comput. Graph.*, 12:461–473, 2006. URL http://dblp.uni-trier.de/db/journals/tvcg/tvcg12.html#SadowskyCT06.

[97] O. Sadowsky, G. Chintalapani, and R. H. Taylor. Deformable 2d-3d registration of the pelvis with a limited field of view, using shape statistics. In *MICCAI*, volume 4792 of *Lecture Notes in Computer Science*, pages 519–526. Springer Berlin Heidelberg, 2007.

[98] Steffen Schumann, Moritz Tannast, Mathias Bergmann, Michael Thali, Lutz-P. Nolte, and Guoyan Zheng. A hierarchical strategy for reconstruction of 3d acetabular surface models from 2d calibrated x-ray images. In Purang Abolmaesumi, Leo Joskowicz, Nassir Navab, and Pierre Jannin, editors, *Information Processing in Computer-Assisted Interventions*, pages 74–83, Berlin, Heidelberg, 2012. Springer Berlin Heidelberg. ISBN 978-3-642-30618-1.

[99] Steffen Schumann, Li Liu, Moritz Tannast, Mathias Bergmann, Lutz-P. Nolte, and Guoyan Zheng. An integrated system for 3d hip joint reconstruction from 2d x-rays: A preliminary validation study. *Annals of Biomedical Engineering*, 41 (10):2077–2087, May 2013. doi: 10.1007/s10439-013-0822-6. URL https://doi.org/10.1007/s10439-013-0822-6.

[100] Steffen Schumann, Benedikt Thelen, Steven Ballestra, Lutz-P. Nolte, Philippe Büchler, and Guoyan Zheng. X-ray image calibration and its application to clinical orthopedics. *Medical Engineering & Physics*, 36(7):968–974, July 2014. doi: 10.1016/j.medengphy.2014.04.001. URL https://doi.org/10.1016/j.medengphy.2014.04.001.

[101] Steffen Schumann, Richard Bieck, Rainer Bader, Johannes Heverhagen, Lutz-P. Nolte, and Guoyan Zheng. Radiographic reconstruction of lower-extremity bone fragments: a first trial. *International Journal of Computer Assisted Radiology and Surgery*, 11(12):2241–2251, Dec 2016. ISSN 1861-6429.

[102] F Seehaus, J Emmerich, BL Kaptein, H Windhagen, and C Hurschler. Dependence of model-based rsa accuracy on higher and lower implant surface model quality. *BioMedical Engineering OnLine*, (32), 2013. doi: 10.1186/1475-925X-12-32.

[103] G Selvik. Roentgen stereophotogrammetry. a method for the study of the kinematics of the skeletal system. *Acta Orthopeadica Scandinavia. Supplementum.*, 232:1–51, 1989.

[104] G Selvik. Roentgen stereophotogrammetric analysis. *Acta Radiologica*, 31(2): 113–126, 1990.

[105] G. Selvik, P. Alberius, and A. S. Aronson. A roentgen stereophotogrammetric system. *Acta Radiologica. Diagnosis*, 24(4):343–352, July 1983. doi: 10.1177/028418518302400412. URL https://doi.org/10.1177/028418518302400412.

[106] B Shareghi, PE Johanson, and J Kärrholm. Clinical evaluation of model-based radiostereometric analysis to measure femoral head penetration and cup migration in four different cup designs. *Journal of Orthopaedic Research*, 35(4): 760–767, 2017. ISSN 1554-527X.

[107] Anis Shazia, Khin Wee Lai, Joon Huang Chuah, Mohammad Ali Shoaib, Hamidreza Mohafez, Maryam Hadizadeh, Yan Ding, and Zhi Chao Ong. An overview of deep learning approaches in chest radiograph. *IEEE Access*, pages 1–1, 2020. doi: 10.1109/access.2020.3028390. URL https://doi.org/10.1109/access.2020.3028390.

[108] P. Shirley and A. Tuchman. A polygonal approximation to direct scalar volume rendering. In *Proceedings of the 1990 Workshop on Volume Visualization*, VVS '90, pages 63–70, New York, 1990. ACM.

[109] H. Si. Tetgen, a delaunay-based quality tetrahedral mesh generator. *ACM Trans. Math. Softw.*, 41:11:1–11:36, 2015.

[110] P. Skadlubowicz, Z. Król, Z. Wróbel, F. Hefti, and A. Krieg. Using of statistical shape models for pelvis reconstruction in the oncologic surgery. *Journal of Medical Informatics and Technologies*, 13:151–156, 2009.

[111] Lowell M. Smoger, Kevin B. Shelburne, Adam J. Cyr, Paul J. Rullkoetter, and Peter J. Laz. Statistical shape modeling predicts patellar bone geometry to enable stereo-radiographic kinematic tracking. *Journal of Biomechanics*, 58:187 – 194, 2017. ISSN 0021-9290.

[112] Aaron Sodickson, Pieter F. Baeyens, Katherine P. Andriole, Luciano M. Prevedello, Richard D. Nawfel, Richard Hanson, and Ramin Khorasani. Recurrent CT, cumulative radiation exposure, and associated radiation-induced cancer risks from CT of adults. *Radiology*, 251(1):175–184, April 2009. doi: 10.1148/radiol.2511081296. URL https://doi.org/10.1148/radiol.2511081296.

[113] Peter Spellucci. *DONLP2 users guide*. Technical University at Darmstadt, Department of Mathematics, Darmstadt, Germany, 1993.

[114] M. Stilling, S. Kold, S. de Raedt, N. T. Andersen, O. Rahbek, and K. Søballe. Superior accuracy of model-based radiostereometric analysis for measurement of polyethylene wear. *Bone & Joint Research*, 1(8):180–191, August 2012. doi: 10.1302/2046-3758.18.2000041. URL https://doi.org/10.1302/2046-3758.18.2000041.

[115] Maiken Stilling, Inger Mechlenburg, Anders Amstrup, Kjeld Soballe, and Thomas Klebe. Precision of novel radiological methods in relation to resurfacing humeral head implants: assessment by radiostereometric analysis, DXA, and geometrical analysis. *Archives of Orthopaedic and Trauma Surgery*, 132(11): 1521–1530, July 2012. doi: 10.1007/s00402-012-1580-x. URL https://doi.org/10.1007/s00402-012-1580-x.

[116] Jonathan J. Streit, Yousef Shishani, Meridith E. Greene, Audrey K. Nebergall, John Paul Wanner, Charles R. Bragdon, Henrik Malchau, and Reuben Gobezie. Radiostereometric and radiographic analysis of glenoid component motion after total shoulder arthroplasty. *Orthopedics*, 38(10), October 2015. doi: 10.3928/01477447-20151002-56. URL https://doi.org/10.3928/01477447-20151002-56.

[117] K. Subburaj, B. Ravi, and Manish Agarwal. Automated identification of anatomical landmarks on 3d bone models reconstructed from CT scan images. *Computerized Medical Imaging and Graphics*, 33(5):359–368, July 2009. doi: 10.1016/j.compmedimag.2009.03.001. URL https://doi.org/10.1016/j.compmedimag.2009.03.001.

[118] CB Syu, JY Lai, RY Chang, KS Shih, KJ Chen, and SC Lin. Automatic model-based roentgen stereophotogrammetric analysis (rsa) of total knee prostheses. *Journal of Biomechanics*, 45:164–171, 2012.

[119] T. S.Y. Tang and R. E. Ellis. 2d/3d deformable registration using a hybrid atlas. In *MICCAI*, volume 3750 of *Lecture Notes in Computer Science*, pages 223–230. Springer Berlin Heidelberg, 2005.

[120] Daniel Toth, Shun Miao, Tanja Kurzendorfer, Christopher A. Rinaldi, Rui Liao, Tommaso Mansi, Kawal Rhode, and Peter Mountney. 3d/2d model-to-image registration by imitation learning for cardiac procedures. *International Journal of Computer Assisted Radiology and Surgery*, 13(8):1141–1149, May 2018. doi: 10.1007/s11548-018-1774-y. URL https://doi.org/10.1007/s11548-018-1774-y.

[121] J. Uvehammer, J. Kärrholm, S. Brandsson, P. Herberts, L. Carlsson, J. Karlsson, and L. Regnér. In vivokinematics of total knee arthroplasty: Flat compared with concave tibial joint surface. *Journal of Orthopaedic Research*, 18(6):856–864, November 2000. doi: 10.1002/jor.1100180603. URL https://doi.org/10.1002/jor.1100180603.

[122] Marta Valenti, Elena De Momi, Weimin Yu, Giancarlo Ferrigno, Mohsen Akbari Shandiz, Carolyn Anglin, and Guoyan Zheng. Fluoroscopy-based tracking of femoral kinematics with statistical shape models.

[123] Edward R Valstar, Eric H Garling, and Piet M Rozing. Micromotion of the souter-strathclyde total elbow prosthesis in patients with rheumatoid arthritis. *Acta Orthopaedica Scandinavica*, 73(3):264–272, January 2002. doi: 10.1080/00016470232015522O. URL https://doi.org/10.1080/00016470232015522O.

[124] ER Valstar, FW de Jong, HA Vrooman, PM Rozing, and JHC Reiber. Model-based roentgen stereophotogrammetry of orthopaedic implants. *Journal of Biomechanics*, 34(6):715–722, 2001.

[125] ER Valstar, R Gill, L Ryd, G Flivik, N Börlin, and J Kärrholm. Guidelines for standardization of radiostereometry (rsa) of implants. *Acta Orthopaedica*, 76(4): 563–572, 2005.

[126] J. C. T. van der Lugt, E. R. Valstar, S. W. Witvoet-Braam, and R. G. H. H. Nelissen. Migration of the humeral component of the souter-strathclyde elbow prosthesis. *The Journal of Bone and Joint Surgery. British volume*, 92-B(2):235–241, February 2010. doi: 10.1302/0301-620x.92b2.22636. URL https://doi.org/10.1302/0301-620x.92b2.22636.

[127] J. Victor, D. Van Doninck, L. Labey, B. Innocenti, P.M. Parizel, and J. Bellemans. How precise can bony landmarks be determined on a CT scan of the knee? *The Knee*, 16(5):358–365, October 2009. doi: 10.1016/j.knee.2009.01.001. URL https://doi.org/10.1016/j.knee.2009.01.001.

[128] Paul Van Der Voort, Martijn L D Klein Nulent, Edward R Valstar, Bart L Kaptein, Marta Fiocco, and Rob G H H Nelissen. Long-term migration of a cementless stem with different bioactive coatings. data from a "prime" RSA study: lessons learned. *Acta Orthopaedica*, 91(6):660–668, November 2020. doi: 10.1080/17453674.2020.1840021. URL https://doi.org/10.1080/17453674.2020.1840021.

[129] B. F. Wall and D. Hart. Revised radiation doses for typical x-ray examinations. report on a recent review of doses to patients from medical x-ray examinations

in the uk by nrpb. national radiological protection board. *The British Journal of Radiology*, 70:437–439, 1997.

[130] Ge Wu, Sorin Siegler, Paul Allard, Chris Kirtley, Alberto Leardini, Dieter Rosenbaum, Mike Whittle, Darryl D D'Lima, Luca Cristofolini, Hartmut Witte, Oskar Schmid, and Ian Stokes. ISB recommendation on definitions of joint coordinate system of various joints for the reporting of human joint motion—part i: ankle, hip, and spine. *Journal of Biomechanics*, 35(4):543–548, April 2002. doi: 10.1016/s0021-9290(01)00222-6. URL https://doi.org/10.1016/s0021-9290(01)00222-6.

[131] J. Yao and R. Taylor. Assessing accuracy factors in deformable 2d/3d medical image registration using a statistical pelvis model. In *Ninth IEEE International Conference on Computer Vision*, volume 2, pages 1329–1334, 2003.

[132] J. Yao and R. H. Taylor. Construction and simplification of bone density models. In *Medical Imaging: Image Processing*, volume 4322 of *Proc. SPIE*, pages 814–823. SPIE-The International Society for Optical Engineering, 2001.

[133] G. Zheng, S. Gollmer, S. Schumann, X. Dong, T. Feilkas, and T. A. Gonz?lez Ballester. A 2d/3d correspondence building method for reconstruction of a patient-specific 3d bone surface model using point distribution models and calibrated x-ray images. *Medical Image Analysis*, 13:883 – 899, 2009.

[134] Guoyan Zheng and Steffen Schumann. 3d reconstruction of a patient-specific surface model of the proximal femur from calibrated x-ray radiographs: A validation studya). *Medical Physics*, 36(4):1155–1166, March 2009. doi: 10.1118/1.3089423. URL https://doi.org/10.1118/1.3089423.

[135] Guoyan Zheng, Steffen Schumann, Alper Alcoltekin, Branislav Jaramaz, and Lutz-P. Nolte. Patient-specific 3d reconstruction of a complete lower extremity from 2d x-rays. In Guoyan Zheng, Hongen Liao, Pierre Jannin, Philippe Cattin, and Su-Lin Lee, editors, *Medical Imaging and Augmented Reality*, pages 404–414, Cham, 2016. Springer International Publishing. ISBN 978-3-319-43775-0.

[136] Guoyan Zheng, Alper Alcoltekin, Benedikt Thelen, and Lutz-P. Nolte. 3x-knee: A novel technology for 3d preoperative planning and postoperative evaluation of TKA based on 2d x-rays. In *Advances in Experimental Medicine and Biology*, pages 93–103. Springer Singapore, 2018. doi: 10.1007/978-981-13-1396-7_8. URL https://doi.org/10.1007/978-981-13-1396-7_8.

[137] R. Zinno, S. Di Paolo, G. Ambrosino, D. Alesi, S. Zaffagnini, G. Barone, and L. Bragonzoni. Migration of the femoral component and clinical outcomes after total knee replacement: a narrative review. *MUSCULOSKELETAL SURGERY*,

December 2020. doi: 10.1007/s12306-020-00690-8. URL https://doi.org/10.1007/s12306-020-00690-8.

PUBLICATIONS

Core publications forming the thesis are listed below. Selected parts of the thesis were also presented at the 5th Bilateral Symposium with International Participation, a meeting of traumatology surgeons, radiologists, and radiology assistants, and at HiVisComp 2019, a meeting of the Czech and Slovak computer graphics and computer vision community.

[KNM+18] Ondřej Klíma, Petr Novobilský, Roman Madeja, David Bařina, Adam Chromý, Michal Španel, and Pavel Zemčík. Intensity-based nonoverlapping area registration supporting "drop-outs" in terms of model-based radiostereometric analysis. *Journal of Healthcare Engineering*, 2018:8538125, May 2018. doi: 10.1155/2018/8538125 (**impact factor: 1.295**, see Chapter 5)

[KKŠZ16a] Ondřej Klíma, Petr Klepárník, Michal Španel, and Pavel Zemčík. Intensity-based femoral atlas 2D/3D registration using Levenberg-Marquardt optimisation. In *Medical Imaging 2016: Biomedical Applications in Molecular, Structural, and Functional Imaging*, volume 9788, pages 113 – 124. International Society for Optics and Photonics, SPIE, 2016. doi: 10.1117/12.2216529 (see Chapter 6)

[KCZ+16] Ondřej Klíma, Adam Chromý, Pavel Zemčík, Michal Španěl, and Petr Klepárník. A study on performace of Levenberg-Marquardt and CMA-ES optimization methods for atlas-based 2D/3D reconstruction. *IFAC-PapersOnLine*, 49(25):121–126, 2016. 14th IFAC Conference on Programmable Devices and Embedded Systems PDES 2016. doi: 10.1016/j.ifacol.2016.12.021 (see Chapter 7)

[KBK+16] Ondřej Klíma, David Bařina, Petr Klepárník, Pavel Zemčík, Adam Chromý, and Michal Španěl. Lossy compression of 3D statistical shape and intensity models of femoral bones using JPEG 2000. *IFAC-PapersOnLine*, 49(25):115 – 120, 2016. 14th IFAC Conference on Programmable Devices and Embedded Systems PDES 2016. doi: 10.1016/j.ifacol.2016.12.020 (see Chapter 8)

[KMŠ+18] Ondřej Klíma, Roman Madeja, Michal Španel, Martin Čuta, Pavel Zemčík, Pavel Stoklásek, and Aleš Mizera. Virtual 2D-3D fracture reduction with bone length recovery using statistical shape models. In

Shape in Medical Imaging, pages 207–219, Cham, 2018. Springer International Publishing. doi: 10.1007/978-3-030-04747-4_20 (see Chapter 9)

[KKŠZ16b] Ondřej Klíma, Petr Klepárník, Michal Španěl, and Pavel Zemčík. Towards an accurate 3D reconstruction of fractured long bones from plain 2D radiographs. volume 11 of *CARS 2016—Computer Assisted Radiology and Surgery Proceedings of the 30th International Congress and Exhibition Heidelberg, Germany, June 21–25, 2016*, pages 180–181. International Journal of Computer Assisted Radiology and Surgery, 2016. doi: 10.1007/s11548-016-1412-5 (*extended abstract*, see Appendix B)

[KCK+17] Ondřej Klíma, Adam Chromý, Petr Klepárník, Michal Španěl, and Pavel Zemčík. Model-based radiostereometric analysis using intensity-based 2D/3D registration pipeline: Feasibility study. Conference Materials and Posters of Spring Conference on Computer Graphics SCCG 2017, pages 31–33. Mikulov: Vysoké učení technické v Brně, 2017. http://sccg.sk/ (*extended abstract*, see Appendix A)

[KKŠZ15] Ondřej Klíma, Petr Klepárník, Michal Španěl, and Pavel Zemčík. GP-GPU accelerated intensity-based 2D/3D registration pipeline. Proceedings of Shape Symposium, pages 19–19. Delemont: Swiss Institute for Computer Aided Surgery, 2015. http://www.shapesymposium.org/ (*extended abstract*, see Appendix C)

PUBLICATIONS

The following list includes selected publications beyond the scope of the thesis. Current lists are available at ORCID iD 0000-0001-9295-065X, Scopus Author ID 57193340483 and Researcher ID I-4030-2018.

[MBK+21] Roman Madeja, Grzegorz Bajor, Ondřej Klíma, Lubor Bialy and Jana Pometlová. Computer-Assisted Preoperative Planning of Reduction and Osteosynthesis of Scapular Fracture: A Case Report. *Open Medicine*, Walter de Gruyter, ISSN 2391-5463, 2021. (In press, **impact factor: 2.199**)

[PCM+21] Lenka Polcerová, Mária Chovancová, Miroslav Králík, Radoslav Beňuš, Ondřej Klíma, Tereza Meinerová, Martin Čuta and Mária Petrová. Radioulnar Contrasts in Fingerprint Ridge Counts: Searching for Dermatoglyphic Markers of Early Sex Development *American Journal of Human Biology*, ISSN 1520-6300, 2021. (Minor revisions required, **impact factor: 1.937**)

[DO20] David Bařina and Ondřej Klíma. JPEG 2000: guide for digital libraries. *Digital Library Perspectives*, 36(3):249–263, Jan 2020. doi: 10.1108/DLP-03-2020-0014

[KKU+18] Miroslav Králík, Ondřej Klíma, Petra Urbanová, Lenka Polcerová, and Martin Čuta. Morphometric sex estimation from the hip bone by means of the hip 1.1 software. In *Shape in Medical Imaging*, pages 78–89, Cham, 2018. Springer International Publishing. doi: 10.1007/978-3-030-04747-4_8

[CK17] Adam Chromý and Ondřej Klíma. A 3D scan model and thermal image data fusion algorithms for 3D thermography in medicine. *Journal of Healthcare Engineering*, 2017:5134021, Nov 2017. doi: 10.1155/2017/5134021 (**impact factor: 1.261**)

[KIK+17] Miroslav Králík, Pavlína Ingrová, Sławomir Kozieł, Adela Hupková, and Ondřej Klíma. Overall trends vs. individual trajectories in the second-to-fourth digit (2D:4D) and metacarpal (2M:4M) ratios during puberty and adolescence. *American Journal of Physical Anthropology*, 162(4):641–656, 2017. doi: 10.1002/ajpa.23153 (**impact factor: 2.901**)

[CŽK16] Adam Chromý, Luděk Žalud, and Ondřej Klíma. Deskbalance: Novel gamified system for diagnosis and treatment of postural sta-

bility. *IFAC-PapersOnLine*, 49(25):200–205, 2016. 14th IFAC Conference on Programmable Devices and Embedded Systems PDES 2016. doi: 10.1016/j.ifacol.2016.12.034

[BKZ16b] David Bařina, Ondřej Klíma, and Pavel Zemčík. Single-loop software architecture for JPEG 2000. In *Data Compression Conference (DCC)*, pages 582–582, 2016. doi: 10.1109/DCC.2016.19

[BKZ16a] David Bařina, Ondřej Klíma, and Pavel Zemčík. Single-loop architecture for JPEG 2000. In *International Conference on Image and Signal Processing (ICISP)*, volume 9680 of *Lecture Notes in Computer Science (LNCS)*, pages 346–355. Springer, 2016. doi: 10.1007/978-3-319-33618-3_35

LIST OF FIGURES

LIST OF TABLES

LIST OF ACRONYMS

AP	Anterior-Posterior.
BPC	Bits per Component.
BPT	Bits per Tetrahedron.
BPV	Bits per Vertex.
BW	Black&White.
CAD	Computer Aided Design.
CHT	Circular Hough Transformation.
CMA-ES	Covariance Matrix Adaptation Evolution Strategy.
CMSA-ES	Covariance Matrix Self Adaptation Evolution Strategy.
CPU	Central Processing Unit.
CR	Computed Radiography.
CT	Computed Tomography.
DCI	Digital Cinema Initiatives.
DLT	Direct Linear Transformation.
DOF	Degrees of Freedom.
DR	Digital Radiograph.
DRR	Digitally Reconstructed Radiograph.
DWT	Discrete Wavelet Transform.
FCP	Fiducial and Control Planes.
GPA	Generalized Procrustes Analysis.
GPGPU	General Purpose Computations on Graphics Processing Units.
GPU	Graphics Processing Unit.
HU	Hounsfield Units.
L.-M.	Levenberg-Marquardt.
LAT	Lateral.
MBRSA	Model-based Radiostereometric Analysis.
NLS	Nonlinear Least Squares.
NMI	Normalized Mutual Information.
NOA	Nonoverlapping Area.

OpenGL Open Graphics Library.

PCA Principal Component Analysis.

PD Pixel Differences.

PDM Point Distribution Model.

PPCA Probabilistic Principal Component Analysis.

PT Projected Tetrahedra.

RE Reverse Engineering.

RMS Root Mean Square.

RMSE Root Mean Squared Error.

RSA Radiostereometric Analysis.

SSIM Statistical Shape and Intensity Model.

SSD Sum of Squared Differences.

SSM Statistical Shape Model.

TKA Total Knee Arthroplasty.

THA Total Hip Arthroplasty.

VSD Virtual Skeleton Database.

COLOPHON

This document was typeset using the typographical look-and-feel `classicthesis` developed by André Miede. The style was inspired by Robert Bringhurst's seminal book on typography *"The Elements of Typographic Style"*. It is available for LaTeX via CTAN as `classicthesis`.

Final Version as of August 31, 2021 (`classicthesis` version 1.0).